N° d'ordre :

University of Saida – Dr. Moulay Tahar
Faculty of Technology

Thesis

Presented to obtain the diploma of
Doctorate in Science
Specialty: Electronics
Field: Electronics

By:

Gouni Slimane

Theme:

Synthesis, Dimensioning and Optimization Techniques for Microwave Filters for Base Station of Mobile Communication

---

These Defended on

December 09th,2024 in front of the jury composed of :

N°	Name	Grade	University	Quality
01	**NOURI Keltouma**	Prof	University of Saida – Dr. Moulay Tahar	President
02	**DAMOU Mehdi**	MCA	University of Saida – Dr. Moulay Tahar	Supervisor
03	**CHETIOUI Mohammed**	MCA	University of Saida – Dr. Moulay Tahar	Co-Supervisor
04	**BERBER Mohammed**	Prof	Centre Universitaire Nour Bachir, El bayadh	Examiner
05	**MAHDJOUB Zoubir**	Prof	Université de Sidi Bel Abbes-Djilali Liabes	Examiner
06	**BENDAOUDI Amina**	Prof	Université de Sidi Bel Abbes- Djilali Liabes	Examiner

Dedications

I dedicate this work to :

To my parents,

my wife,

and my children,

With all my love and gratitude

Acknowledgements

I would like to express my deepest gratitude to my supervisors, **Dr. Damou Mehdi** and **Dr. Chetioui Mohammed**, for their invaluable guidance, support, and time throughout my PhD journey. Their encouragement and insights have been instrumental in completing this work.

I am also profoundly grateful to the esteemed jury members, **Prof. Nouri Keltouma**, **Prof. Mahdjoubi Zoubir**, **Prof. Bendaoudi Amina**, and **Prof. Berber Mohammed**, for their thoughtful feedback, guidance, and their extreme patience in reviewing my thesis. Their contributions have significantly enriched the quality of this research.

Additionally, I would like to extend my heartfelt thanks to my friends and colleagues, **Mr. Boudkhil Abdelhakim**, **Dr. Bouras Bouhaf**, **Dr. Bouhmidi Rachid**, and **prof Ghaouti Djellouli** for their invaluable help and unwavering moral support. Their presence and assistance have been a source of strength and motivation.

Abstract

Mobile communication is an essential aspect of modern life, necessitating continuous improvements in connectivity and reliability. Mobile communication providers face increasing demands to enhance network standards, with base stations playing a crucial role in connecting mobile devices to the broader communication infrastructure. This system's microwave filters are vital for minimizing interference, improving signal quality, and optimizing performance. This research explores various synthesis, dimensioning, and optimization techniques for microwave filters used in mobile communication base stations. The study aims to develop high-performance filters to improve mobile communication systems by examining recent advancements. The first chapter covers the fundamentals of microwave filters, including filter networks, key parameters, and different filter types such as all-pole, transmission zero, and linear phase filters. It also introduces the coupling matrix and its applications and the necessary physical components for implementing microwave filters. Chapter two introduces rectangular bandpass waveguide filters, discussing propagation modes, waveguide resonators, and methods of wavelength transformation. It provides practical examples of filter design and synthesis. The third chapter focuses on developing and optimizing compact microwave filters, detailing the coupling matrix theory and the design of bandpass filters. It covers cross-coupled filters, microscopic filter design, and dual-mode open-loop resonators. The final chapter examines substrate-integrated waveguide (SIW) technology for filter design. It includes analytical design methods, hexagonal cavities, trisection filters, and the group delay method for parameter extraction. The chapter discusses experimental results and the effects of structural variations. This comprehensive study offers valuable insights into advanced methods in microwave filter design, benefiting students, researchers, and professionals in the field.

Key words: Coupled Resonator Filter SIW, HFSS, Coupling Matrix, DGS, AWR

Resume

La communication mobile est un aspect essential de la vie modern, nécessitant des améliorations continues en matière de connectivité et de fiabilité. Les fournisseurs de communications mobiles sont confrontés à des demandes croissantes d'amélioration des normes de réseau, les stations de base jouant un rôle crucial dans la connexion des appareils mobiles à l'infrastructure de communication plus large. Les filtres micro-ondes de ce système sont essentiels pour minimiser les interférences, améliorer la qualité du signal et optimiser les performances. Cette recherche explore diverses techniques de synthèse, de dimensionnement et d'optimisation des filtres micro-ondes utilisés dans les stations de base de communications mobiles. L'étude vise à développer des filtres hautes performances pour améliorer les systèmes de communication mobile en examinant les progrès récents. Le premier chapitre couvre les principes fondamentaux des filtres micro-ondes, y compris les réseaux de filtres, les paramètres clés et différents types de filtres tels que les filtres tous pôles, à transmission nulle et à phase linéaire. Il présente également la matrice de couplage et ses applications ainsi que les composants physiques nécessaires à la mise en œuvre des filtres micro-ondes. Le chapitre deux présente les filtres de guide d'ondes passe-bande rectangulaire, discutant des modes de propagation, des résonateurs de guide d'onde et des méthodes de transformation de longueur d'onde. Il fournit des exemples pratiques de conception et de synthèse de filtres. Le troisième chapitre se concentre sur le développement et l'optimisation de filtres micro-ondes compacts, détaillant la théorie des matrices de couplage et la conception de filtres passe-bande. Il couvre les filtres à couplage croisé, la conception de filtres microruban et les résonateurs à boucle ouverte bimode. Le dernier chapitre examine la technologie de guide d'ondes intégré au substrat (SIW) pour la conception de filtres. Il comprend des méthodes de conception analytique, des cavités hexagonales, des filtres trisections et la méthode de retard de groupe pour l'extraction des paramètres.

Le chapitre discute des résultats expérimentaux et des effets des variations structurelles. Cette étude approfondie offre des informations précieuses sur les méthodes avancées de conception de filtres micro-ondes, bénéficiant aux étudiants, aux chercheurs et aux professionnels du domaine.

Mots clés : Filtre à résonateur couplé SIW, HFSS, Matrice de couplage, DGS, AWR.

Contents

4 Analytical and Synthesis filters Design Substrate Integrated Waveguide (SIW) 125

List of figures

List of tables

List of symbols

f : Frequency

ω : Angular frequency

f_0 : Central frequency

f_c : Cutoff frequency

L : Inductance

C : Capacitance

R : Resistance

c : Velocity oflight in free space

Z_0 : Characteristic impedance

λ_0 : Wavelength in free space

λ_g : Wavelength in the guided medium

λ_c : Cutoff wavelength

E : Electric field

H : Magnetic field

LIST OF ABBREVIATIONS

RF : Radio Frequency

EM : Electromagnetic

TE : Transverse Electric

TM : Transverse Magnetic

LPF : Lowpass Filter

BPF : Bandpass Filter

FBW : Fractional Bandwidth

WG : Wave Guide

$HFSS$: High Frequency Structural Simulator

BW : Bandwidth

General Introduction

Mobile communication has become an indispensable facet of modern life, driving a relentless pursuit of enhanced connectivity and reliability. Amidst this demand, mobile communication providers face escalating pressure to elevate the standards of their networks. At the heart of these networks lies the pivotal base station, serving as the linchpin connecting mobile devices to the expansive communication infrastructure.

Within this intricate ecosystem, microwave filters emerge as indispensable guardians, meticulously sieving through signals to ensure clarity amidst the noise. Their role in minimizing interference, enhancing signal quality, and optimizing performance is paramount. Yet, the quest for superior filters becomes imperative as the clamor for swift er, more dependable services intensifies.

Thus, this research project embarks on a voyage to explore and evaluate a myriad of synthesis, dimensioning, and optimization techniques tailored for microwave filters within mobile communication base stations. By scrutinizing recent advancements and breakthroughs, the endeavor aims to pioneer high-performance filters that augment the efficacy of mobile communication systems.

Chapters unfurl a comprehensive journey through the realm of microwave filter technology. The first chapter delves into the foundational principles of microwave filters. It begins with exploring the basics of filter networks, including the essential role of polynomials in defining filter properties and their mathematical manipulation. Key parameters such as transmission and reflection coefficients are defined, and their calculations are explained. The chapter also covers different types of filters such as all-pole, transmission zero, and linear phase filters–

highlighting their unique frequency responses and characteristic functions. The concept of transmission zeros in linear phase filters is also introduced. Additionally, the chapter explains the coupling matrix and its applications, including the circuit model, spreading factor, and matrix multiplication, along with a diagram illustrating coupling routing. Finally, it overviews the physical components necessary for implementing microwave filters.

Chapter 2 provides an introduction to rectangular bandpass waveguide filters. It discusses the various propagation modes, including TE and TM mode parameters, focusing on the dominant TE10 mode. The chapter explores waveguide resonators and the role of inductive and capacitive irises in creating discontinuities. Different methods of wavelength transformation are compared, providing a thorough understanding of their applications. The chapter also includes practical examples of filter design, such as a direct coupling bandpass filter in rectangular waveguide design and the approximation and synthesis of online pseudo- elliptic filters.

The third chapter focuses on the development and optimization of compact microwave filters. It introduces the coupling matrix theory, detailing the general theory and physical realization of an NxN coupling matrix. The chapter then covers the design of bandpass filters, including specifications, initial models, and considerations for frequency response, equivalent circuits, and EM design. It discusses cross-coupled filters, dimensions, quality factors, coupling coefficient extraction, fabrication, and experimental results. The chapter also explores microscopic filter design, specifically dual-mode open-loop resonators, providing detailed design specifications and theoretical background.

The final chapter examines the design of filters using substrate-integrated waveguide (SIW) technology. It begins with an overview of SIW filter design, followed by analytical design and optimization methods. The chapter covers hexagonal cavities, equivalent circuits, trisection filter design, and the group delay method for parameter extraction, focusing on quality factors and coupling. It discusses the design and experimental results of second and third-order filters with mixed-coupling. Additionally, it explores SIW cross-coupled filters, detailing trisection filter design steps and cascaded quadruplet filters, as well as the effects of structural variations via hole diameters and defected ground structures (DGS).

This summary provides a structured and detailed overview of the essential topics and advanced methods in microwave filter design, offering valuable insights for students, researchers, and professionals in the field.

Chapter 1

Fundamentals of Microwave Filters

1.1 Fundamentals of Microwave Filters

In electronic communication systems, microwave resonator filters are essential because they permit specific frequency to flow through while attenuating others. Radar systems, wireless communication, or communication via satellite are three prominent applications of these filters. By examining the fundamental ideas and regulations about microwave resonator filters, this chapter seeks to lay the groundwork By knowing these basic guidelines.

1.1.1 Polynomials

The insertion loss method for polynomials involves expressing the power output-to- power input ratio in the low pass transfer function. This transfer function is shown as $S_{21}(s)$ using the complex frequency variable. It is standard practice in filter design to replace ”S” where ”j” stands for the angular frequency and ”j” for an imaginary unit.

In the context of filter design, a low pass transfer function $S_{21}(s)$ represents a ratio of two polynomials: one in the numerator and one in the denominator. The numerator polynomial signifies the coefficients of the output voltage, while the denominator polynomial signifies the coefficients of the input voltage.

$$S_{21}(S) = \frac{A(s)}{B(s)} \tag{1.1.1}$$

$$\frac{V_{out}}{V_{in}} = \frac{a_m S^m + a_{m-1} S^{m-1} + . \cdot \cdot \cdot \cdot + a_1 S + a_0}{b_n S^n + b_{n-1} S^{n-1} + \cdot + b_1 S + b_0} = S_{21}(s) \tag{1.1.2}$$

The normalized complex frequency, denoted as $\Omega_S = \sigma_n + j\Omega$, is extensively employed in the theory of Laplace transforms. To ensure that the transfer function precisely characterizes stable systems, the denominator (oft en represented as $S^2 + 1(s)$ or simply the denominator of $T(s)$ must constitute a Hurwitz polynomial [33].

Consequently, the complex frequency domain's left half-plane must contain the roots of the denominator. By solving the transfer function $T(s)$ at $S = j\Omega$, the ratio between the amplitudes of the input and output can be ascertained. In this context, s signifies complex frequency, whereas $j\Omega$ represents imaginary frequency, more precisely angular frequency. In contrast, absolute angular frequency are represented by the symbol Ω, given that $S = j\Omega$ represents a sinusoidal stable state.

Suppose the peak-to-trough amplitude at the network's output is less than the amplitude of the input. In that case, the network attenuates the sinusoidal wave, A commonly used unit to express attenuation in decibels (dB) .

$$A(\Omega) = 20 \log |\frac{V_{in}(j\Omega)}{V_{out}(j\Omega)}|. \tag{1.1.3}$$

Here is another way to describe the transfer function $H(s)$ according to our definition:

$$A(\Omega) = 20 \log |t(j\Omega)|. \tag{1.1.4}$$

As the ratio of input to output, we oft en examine transfer functions in filter theory, which implies we work with:

$$H(s) = \frac{1}{S_{21}(s)} = \frac{a_m S^m + a_{m-1} S^{m-1} + \cdot \cdot \cdot \cdot + a_1 S + a_0}{b_n S^n + b_{n-1} S^{n-1} + \cdot + b_1 S + b_0} = \frac{E(S)}{P(S)}. \tag{1.1.5}$$

It is possible to express the attenuation as follows:

$$A(\Omega) = 20 \log |H(j\Omega)|. \tag{1.1.6}$$

$H(s)$ is the name of an input/output transfer function. Of then, the arbitrary form we want to emulate in a filter's pass band is only a constant. Simplifying the constant value in the pass band involves normalizing it to unity.

$$|H(j\Omega)| \approx 1. \tag{1.1.7}$$

You can use the characteristic function $H(s)$ instead of then constant term.

$$H(s)H(-s) = 1 + K(s)K(-s). \tag{1.1.8}$$

Here is how $H(s)$ may be stated because this Equation shows that the denominator polynomials of $H(s)$ and $K(s)$ are the same:

$$H(s) = \frac{E(S)}{P(S)}. \tag{1.1.9}$$

One approach to representing $K(s)$ is as follows:

$$K(s) = \frac{F(S)}{P(S)}. \tag{1.1.10}$$

One can relate the polynomials using the expressions (1.1.8), (1.1.9), and (1.1.10) as follows:

$$E(s)E(-s) = P(s)P(-s) + F(s)F(-s). \tag{1.1.11}$$

The network's attenuation can be calculated using the following formula:

$$A(\Omega) = 10 \log |H(j\Omega)|^2.) \tag{1.1.12}$$

$$= 10 \log(1 - |H(j\Omega)|^2)$$

Thus, the attenuation becomes infinite when either $K(j\Omega)$ or $H(j\Omega)$ is infinite. But until $K(j\Omega)$ is zero, the attenuation does not become zero. It becomes apparent that the characteristic function is preferable because it removes the unity constant, so that the attenuation poles (reflection zeros) and transmission zeros are highlighted [33].

1.1.2 Transmission and Reflection Coefficients

The transfer function denoted as $S(s)$ and defined as the transmission coefficient in transmission line theory, is represented as follows [33].

$$S_{21}(s) = \frac{transmitted\ wave}{incident\ wave}. \tag{1.1.13}$$

Here are the definitions of the incident wave and the reflection coefficient $S11(s)$:

$$S_{11}(s) = \frac{reflected\ wave}{incident\ wave}. \tag{1.1.14}$$

When expressing the ratio in voltage terms, the sign of ρ is positive; however, when defining it in current terms, it is negative [27].

Since it is the only power available, the reflected and transmitted power must match the available power.

$$|\rho(s)|^2 + |S_{21}(s)|^2 = 1. \tag{1.1.15}$$

The following is an expression for the reflection coefficient using polynomials from (1.1.10) and (1.1.14): [33]

$$\rho(S) = \frac{F(S)}{P(S)}. \tag{1.1.16}$$

Decibels quantify transmission loss, also known as attenuation and reflection loss, sometimes called return loss.

$$A = 10\log\frac{1}{|t(j\Omega)|^2} = -10\log|t(j\Omega)|^2 dB \tag{1.1.17}$$

$$R_L = 10\log\frac{1}{|\rho(j\Omega)|^2} = -10\log|\rho(j\Omega)|^2 dB \tag{1.1.18}$$

One can determine the relationship between transmission and return loss using (1.1.14).

$$A = 10\log(1 - 10^{-R/10})dB \tag{1.1.19}$$

$$R_L = 10\log(1 - 10^{-A/10})dB \tag{1.1.20}$$

As per transmission-line theory [4], the equation for calculating the reflection coefficient $S(j\Omega)$ in a two-port network is as follows:

$$S_{11}(s) = \frac{Z_{in}(s) - R_1}{Z_{in}(s) + R_1} = \frac{Z_{in}(s) - 1}{Z_{in}(s) + 1} \; where \; Z_{in}(s) = \frac{Z_{in}(s)}{R_1} \tag{1.1.21}$$

A polynomial expression for the reflection coefficient is as follows:

$$S_{11}(s) = \frac{Z_{in}(s) - R_1}{Z_{in}(s) + R_1} = \frac{F(s)}{E(s)} \tag{1.1.22}$$

Given that $Z(s)$ is a positive real value, it can be deduced that the denominator polynomial

- The Hurwitz polynomial, $E(s)$, must-have all its roots on the left side of then s-plane.
- Hurwitz polynomials do not occur in the product of the polynomial $F(s)$. However, because the polynomial coefficient has to be precise, their roots must beets truthful at the origin or appear in conjugate complex pairs.

1.1.3 Properties of Polynomials

The filter synthesis commences with the origins of the $P(s)$ and $F(s)$ polynomials, which are ascertainable by the filter parameters. Equation (1.1.11) can be used to derive the polynomial $E(s)$. In the broader situation, these polynomials have particular qualities, such as realizing prototype filters for Nth-order lowpass that are both symmetric and asymmetric.

$F(s)$ has roots on the imaginary axis with a degree of N. The frequency known as reflection zeros indicate no filter loss present since no power is reflected at these frequency.

Transmission zeros, oft en called attenuation poles, happen at frequency with infinite filter loss and no power transmission. These frequency are on the imaginary axis, known as attenuation poles or transmission zeros. The roots of $P(s)$ may take the form of symmetric pairs oriented on the imaginary axis, which would provide linear-phase filters. The degree of these roots is either equal to or less than N. The left half-plane of S contains all Hurwitz polynomial $E(s)$ roots with a degree of N.

1.1.4 Setting the Polynomials to Normal

In (1.1.7), we use the characteristic function S to define the input/output transfer function $H(s)$ as:

$$|H(S)|^2 = 1 + |K(S)|^2 \tag{1.1.23}$$

To retain generality, we may restate the connection as follows by introducing a constant factor ε:

$$|H(S)|^2 = 1 + \varepsilon|K(S)|^2. \tag{1.1.24}$$

The ripple factor ε represents a filter's pass band fluctuation or ripple.

The polynomials $F(S)$ and $P(S)$ have the highest coefficients equal to one before building the filter. One method of achieving this normalization is using ε to determine the most significant coefficients of $F(S)$, $P(S)$, and the prototype amplitude response. As equation (1.1.22) shows, it represents their ratio as an apparent constant factor within the ripple factor. The expression for the transmitted power can be derived from Equation (1.1.22):

$$|T(S)|^2 = \frac{-1}{1+\varepsilon^2|E(S)|^2} = \frac{1|P(S)|^2}{\varepsilon^2|E(S)|^2} \tag{1.1.25}$$

Where

$$|E(S)|^2 = |F(S)|^2 + \frac{|P(S)|^2}{\varepsilon^2}. \tag{1.1.26}$$

The transmission and reflection coefficients are calculated using the following formula:

$$T(S) = \frac{1}{\varepsilon}\frac{p(S)}{E(S)}. \tag{1.1.27}$$

$$\rho(S) = \frac{F(S)}{E(S)} \tag{1.1.28}$$

The selection of ε determines the filter response. ε controls the ripple's size for equiripple pass bands. We usually pick ε based on the maximum allowable ripple in maximally flat pass bands or non-equiripple pass bands. At Ω_1, the filter will show a maximum ripple of $A_1 dB$ in the pass band.

$$|S(j\Omega_1)|^2 = 10^{-A/10} = \frac{1}{1+\varepsilon^2|K(j\Omega_1)|^2}. \tag{1.1.29}$$

The calculation determines the ripple constant.

$$\varepsilon = \sqrt{\frac{10^{A_1/10}-1}{|K(j\Omega_1)|^2}}. \tag{1.1.30}$$

Return loss can also be used to express the ripple constant.

$$\varepsilon = \sqrt{\frac{1}{10^{R_1/10}-1|K(j\Omega_1)|^2}} \tag{1.1.31}$$

The maximum ripple A_1 is linked to return loss R_1. Normalized low pass filter prototypes usually have a cutoff frequency of Ω_1 or unity.

1.1.5 Expansion of the Reflection Coefficients and Transmission

e sections Before this one, we covered polynomials of filters of order N, which may have a maximum of N transmission zeros at a frequency less than N. A filter of order N may have a maximum of N transmission zeros if its frequency is lower than N. Here,

$$T(S) = \frac{1}{\varepsilon}\frac{P(S)}{E(S)}. \tag{1.1.32}$$

$$\rho(S) = \frac{1}{\varepsilon_R}\frac{F(S)}{E(S)} \tag{1.1.33}$$

As in the preceding section, Equation (1.1.33) normalizes the polynomials $E(S)$, $F(S)$, and $P(S)$ so that the coefficients of their highest degree terms equal unity.

To obtain the third polynomial from any two of the three polynomials, use the Equation for energy conservation (1.1.21) with the following procedure:

$$|E(s)|^2 = \frac{|F(S)|^2}{\varepsilon_R^2} + \frac{|P(S)|^2}{\varepsilon^2}. \tag{1.1.34}$$

$E(s)$ and $F(s)$, which are Nth-degree polynomials with leading coefficients normalized to unity, include finite-frequency transmission zeros in the polynomial $P(s)$ of degree Z, where Z represents the number of finite-frequency transmission zeros. For a network to be realizable, Z must be less than or equal to N.

Given that $F(s)$ and (s) are Nth-degree polynomials with leading coefficients of unity, when Z is smaller than N, ε_R must equal unity (1.1.19). This can be reformulated to account for the limited attenuation at $S = \pm j\infty$ when $Z = N$ or $P(s)$ is an Nth-degree polynomial.

$$\frac{1}{\varepsilon_R^2}\frac{\left|F(\pm \dot{j}\infty)\right|^2}{|E(\pm j\infty)|^2} + \frac{1}{\varepsilon^2}\frac{\left|P(\pm \dot{j}\infty)\right|^2}{|E(\pm j\infty)|^2} = 1. \tag{1.1.35}$$

The polynomials $E(s)$, F(s),and $P(s)$ have the highest-degree coefficients of unity and are N^{th}-degree polynomials at $S = \pm j\infty$.

$$\frac{1}{\varepsilon_R^2} + \frac{1}{\varepsilon^2} = 1. \tag{1.1.36}$$

$$|T(S)|^2 = \frac{1}{1 + \dfrac{\varepsilon^2|F(S)|^2}{\varepsilon_R^2|P(S)|^2}} \tag{1.1.37}$$

The ripple constant can also be expressed in its generalized form.

$$\varepsilon = \varepsilon_R\sqrt{\frac{1}{10^{R_1/10} - 1}\frac{1}{|K(j\Omega_1)|^2}} \tag{1.1.38}$$

Using Equation (1.1.35) instead of Equation (1.1.33), one can calculate the ripple factor ε_R.

$$\varepsilon_R = \sqrt{1 + (10^{R_1/10} - 1)|K(j\Omega_1)|^2} \tag{1.1.39}$$

The value of ε_R will be larger than unity for $Z = N$. If the attenuation at $S = \pm j\infty$ is great enough, the ripple factor ε_R will almost equal unity. Here, the transmitted power in (1.1.34) and the ripple factor in (1.1.35) expressions are comparable to those in (1.1.29) and (1.1.23), respectively [33].

1.2 Frequency Responses and Characteristic Functions

A filter is a network that selectively permits some frequency to go through while attenuating others [27]. A filter that attenuates frequency has a magnitude response that is either negligible or almost zero in that particular frequency range. As shown in Fig. (1.1), an ideal low pass filter is a network that attenuates all frequency over this threshold while allowing frequency up to a specific cutoff frequency to pass through.

It is impossible to achieve the desired ideal characteristic due to the inability to perform the frequency response shown in Fig.(1.1) The approximation issue arises from the need to create a realizable transfer function.

The desired ideal characteristic cannot be achieved because the frequency response shown in Fig.(1.1) cannot be achieved. The approximation issue arises from the need to create a realizable transfer function.

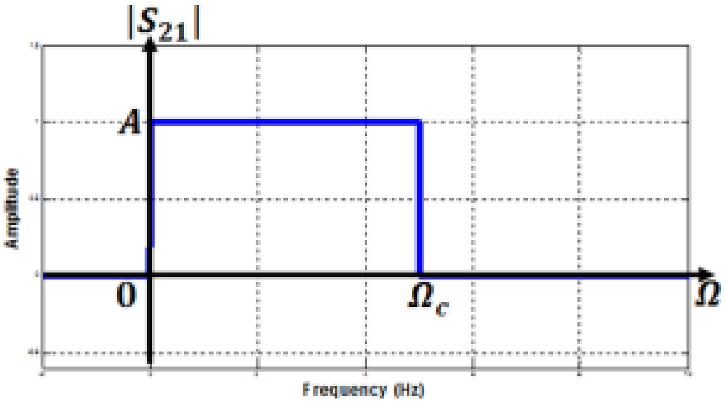

Figure 1.1: Lowpass filter's amplitude spectrum

The normalized lowpass prototype filters are presented for reference

1.2.1 All-Pole Filters

The structure that follows defines the all-pole filter's characteristic function:

$$K(S) = \frac{F(s)}{P(S)} \tag{1.2.1}$$

Where $P(S) = 1$. The transfer function:

$$T(S) = \frac{1}{E(S)} \tag{1.2.2}$$

Transmission zeros are nonexistent at some frequency. Every transmission's zero location is unlimited. $F(s)$, the polynomial, defines the filter's frequency response.

The poles of the polynomial $F(s)$, not the zeros, are crucial for determining the frequency response of a system. Specifically, for a Butterworth filter, also known as a maximally flat magnitude filter, all poles are located on a circle in the left half of the complex plane, equidistant from the origin, ensuring that the frequency response is as flat as possible at the origin ($\omega = 0$) within the pass band. The term "maximally flat" refers to the characteristic that the magnitude response has a maximally flat (no ripples) characteristic in the pass band and rolls off towards zero in the stop band. The Nth-order Butterworth polynomial defines the denominator of the system's transfer function, and its magnitude squared gives the filter's frequency response. The characteristic function of an Nth-order Butterworth filter can be expressed in terms of its poles, which are complex and occur in conjugate pairs.

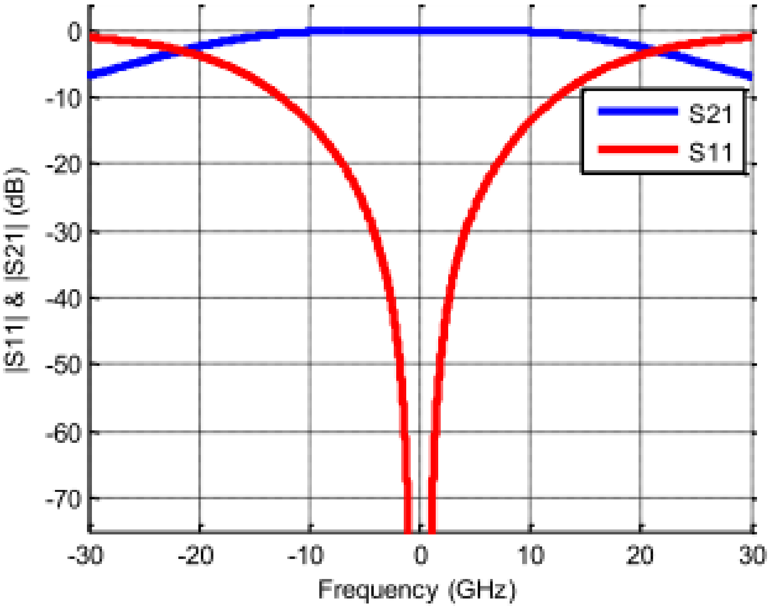

Figure 1.2: the fourth-order Butterworth filter's lowpass repones

$$K(s) = F(s) = S^N \tag{1.2.3}$$

and the transmitted power is given by

$$|T(S)|^2 = \frac{1}{1 + \varepsilon^2 S^N} \tag{1.2.4}$$

Over the passband, the maximum amplitude fluctuation is defined by the ripple factor ε. For instance, the selection of ε as unity indicates that half of the power is transmitted at the cutoff frequency $\Omega c = 1$. Fig.(1.3) displays the amplitude response of $4th$-order maximally flat filter with $\varepsilon = 0 : 1005$. This ripple constant corresponds to a $20dB$ return loss at $\Omega = \pm 1$.

The roots of the polynomial, denoted $F(S)$, can be at finite frequency, and the following expression defines the associated characteristic function:

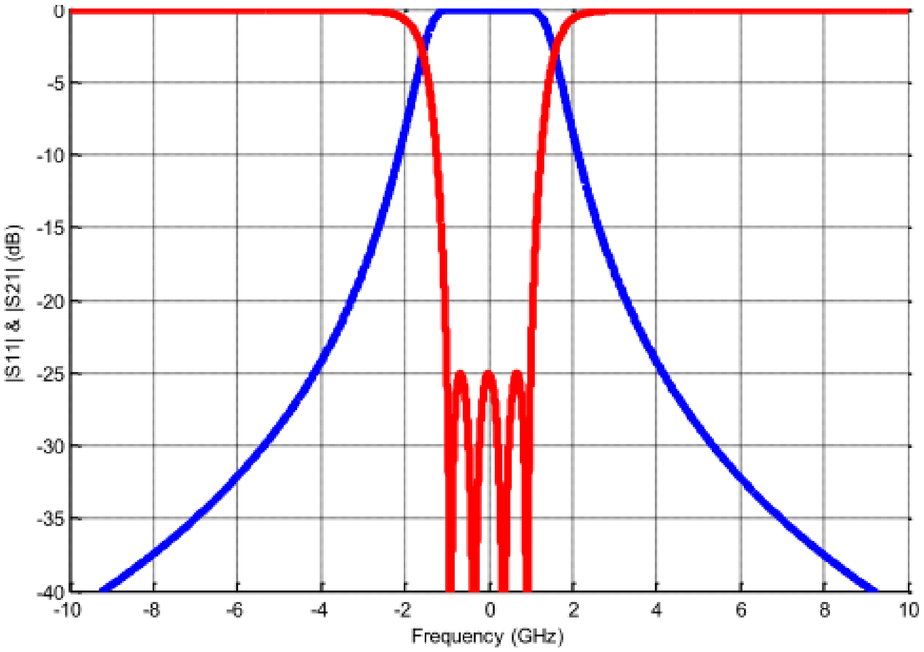

Figure 1.3: Fourth-order all-pole filter with an arbitrary distribution of reflection zeros and its lowpass response.

$$K(S) = F(S) = (S - S_{f1})(S - S_{f2}) \cdots (S - S_{fN}) \tag{1.2.5}$$

The lowpass amplitude response of a $4th$-order all-pole filter, characterized by reflection zeros at $Sf = \pm jO.95$ and $Sf = \pm jO.25$, exhibits a $20dB$ return loss at $\Omega = \pm 1$.

This response is sometimes called the Tchebychev response when the roots are strategically positioned to produce an equi-ripple frequency response in the passband.

Fig.(1.4) depicts the lowpass amplitude response of a fourth-order Tchebychev filter, demonstrating an equi-ripple return loss of $20dB$. For this particular Tchebychev response (equi-ripple), the reflection zeros can be selected using the Tchebychev polynomial, as referenced in [16]. In Fig.(1.4), the reflection zeros are located at Sf $= j0.9239$ and $Sf = j0.827$, and the nipple constant is $\varepsilon = 0.0425$.

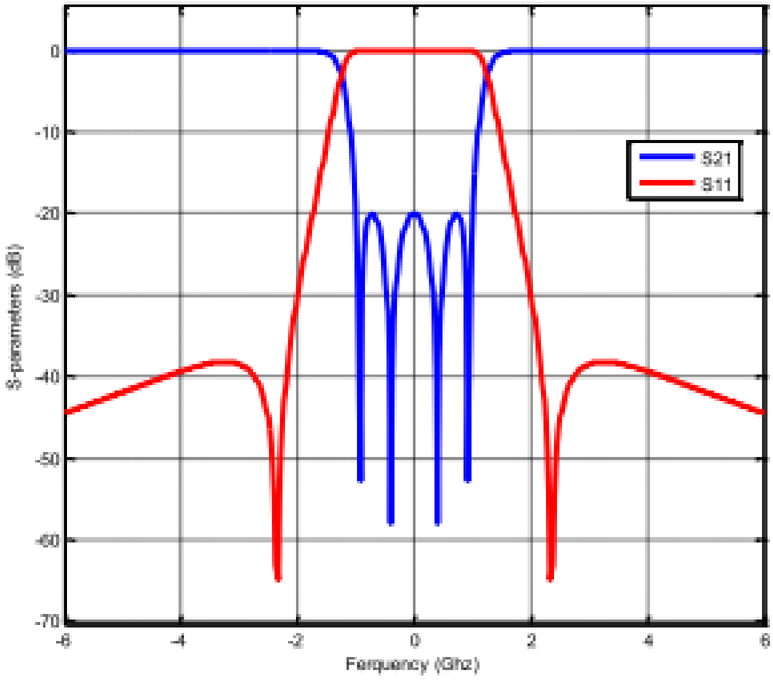

Figure 1.4: The lowpass response of the $4th$-order Tchebychev response filter is shown, with a $20dB$ equisetum loss

1.2.2 Transmission Zero Filters

The characteristic function of then filters with transmission zeros is as follows:

$$K(s) = \frac{F(S)_{-}(S - s_{f1})(S - s_{f2})\cdots(S - S_{fn})}{P(S)(S - s_{p1})(S - s_{p2}).(S - S_{pn})} \tag{1.2.6}$$

In a finite-frequency transmission, T must represent the number of zeros and be less than or equal to N. The positions of points S_{f_i} and S_{pi} are along the imaginary axis. The filter may exhibit an equi-ripple response in the passband, the stopped, or both, depending on the locations of the roots of $F(s)$ and $P(s)$. Equal filter responses in the passband and stopped characterize an elliptic function response. The characteristic function $K(s)$ for an oval function response can be derived using the Jacobian elliptic function. Building filters with a non-equi-ripple reaction in the stopped can oft en generate excellent near-band rejection characteristics.

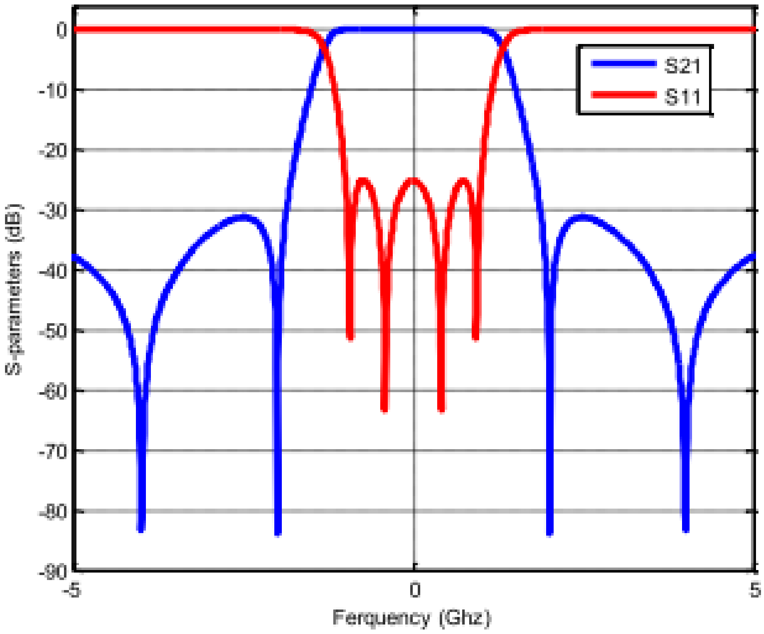

Figure 1.5: Response of then 4th order filter exhibits a $20dB$ equi-ripple return loss, with transmission zeros at $Sp = j2.4$ and $j3.6$ [33].

The frequency response of a $4th$-order filter, as shown in Fig.(1.5), exhibits characteristics of equi-ripple Transmission zeros at $Sp = j2.4$ and $j3.6$, which are also present in the band's response. For the equi-ripple response in the passband, the reflection zeros may be found using the characteristic function $K(S)$ [33].

$$K(i\Omega) = \cosh(\sum_{i=1}^{N} \cosh^{-1}(\frac{\Omega - 1/\Omega_i}{1 - \Omega/\Omega_i})) \tag{1.2.7}$$

It is easy to find the reflection zeros by calculating the filter's reflection coefficient, where Ωi denotes the location of then i^{th} reflection zero.

Near the passband, the selectivity of the transmission zero filters is greater than that of the all-pole filter. The wide-band selectivity of the all-pole filter is superior. However, Fig.(1.6) contrasts the transmission coefficients shown in Figures (1.2, 1.4, and 1.5). At $\Omega = \pm 1$, each filter has a $20dB$ return loss.

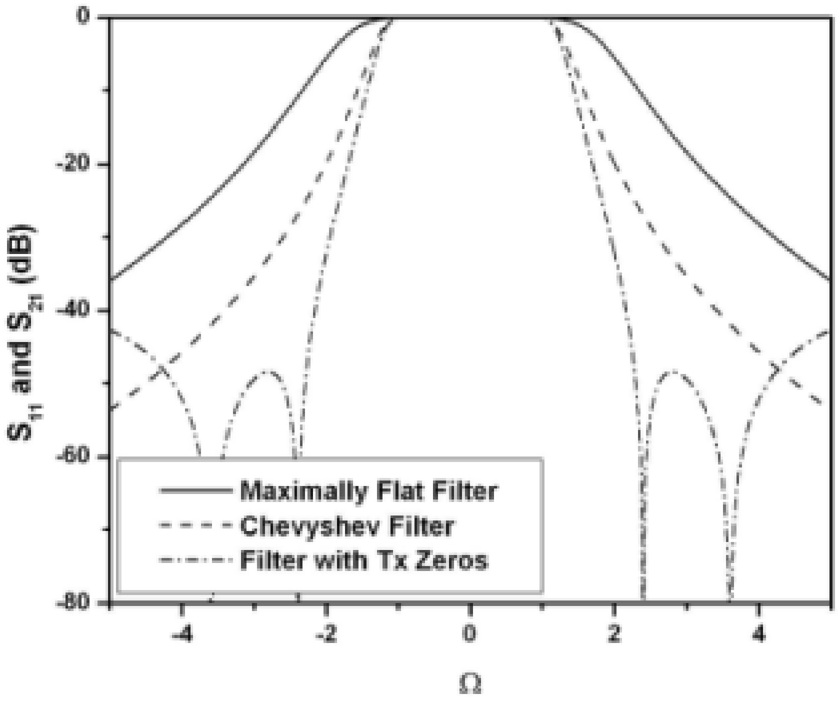

Figure 1.6: These are the 4th-order filteres lowpass response in the illustrations 1.2,1.4 and 1.5. [4]

1.2.3 Linear Phase Filters

The linear phase filters' characteristic function may be found by:

$$K(S) = \frac{F(S)}{P(S)} = \frac{(s - s_{f1})(s - s_{f2}) \cdots (s - s_{fN})}{(s - s_{p1})(s - s_{p2})(s - s_{pT})} \tag{1.2.8}$$

The location of $P(s)$ roots concerning the imaginary axis should be symmetrical. For instance, $isn_1 + jW_1$ should be one of the roots of $P(s)$ if $Sp_1 = sn_1 + jW_1$. Linear phase filters may have maximally flat, equiripple, or non-equiripple pass bands.

1.2.4 Transmission Zeros in Linear Phase Filters

Except for the polynomial $P(S)$, which has roots on the imaginary axis, Equation (1.2.5) depicts the characteristic function of then linear phase filters with zeros that resemble gears.

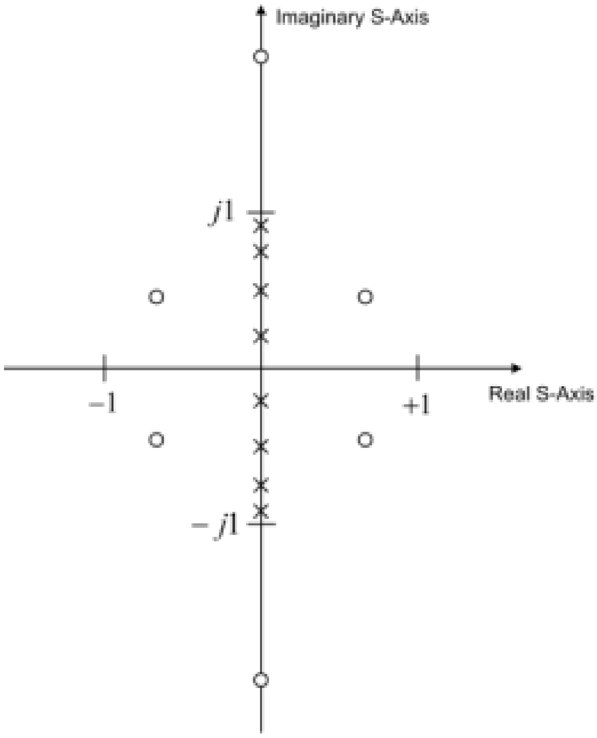

Figure 1.7: The root locations of $P(s)$ and $F(s)$ in the linear phase filter with a gearbox zero can be represented using the symbols x and 0, respectively

Roots on the imaginary axis represent transmission zeros at finite frequency, while pairs of roots symmetrically positioned about the imaginary axis characterize linear phase in the passband. Fig.(1.7) depicts the locations of the roots of $F(s)$ (denoted by S_f) and $P(s)$ (represented by Sp) for the linear phase filter example with a transmission zero. On the imaginary axis, there are two $P(s)$ roots, and in the S-plane, $P(s)$ has four complex roots. Fig.(1.8) illustrates the filter's group delay and amplitude responses. Notably, the complex roots of $P(s)$ contribute to equalizing the group delay in the passband. Therefore, the complex roots compensate for the filter's group delay variations.

Changes made:

- Clarified the representation of $F(s)$ and $P(s)$ roots by denoting them S_f and S_p, respectively.
- Replaced complicated roots with complex roots to use more standard terminology.
- Improved sentence structure and flow for better clarity and readability.

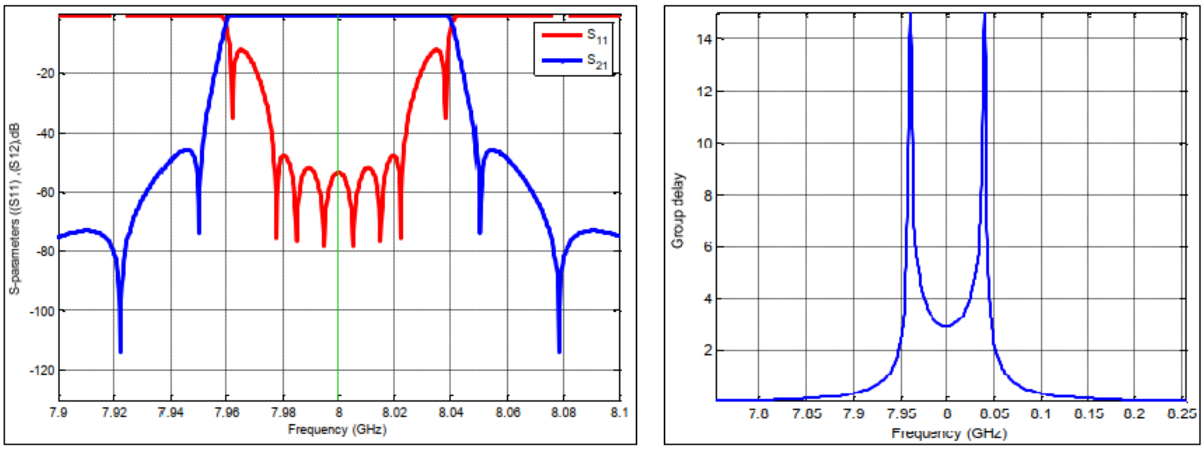

Figure 1.8: Gearbox zeros for linear phase filtering (a)the amplitude response ; (b) the response derived from the group delay .

Users utilize this filter as a lowpass

$$T(\Omega) = -\frac{d\phi(\Omega)}{d\Omega} \tag{1.2.9}$$

The frequency response of a bandpass filter is obtained using the conventional frequency transformation, where ϕ is the phase of $\Omega(t)$ expressed in radians.

$$\Omega = \frac{1}{B}\left(\frac{f}{f_0} - \frac{f_0}{f}\right) \tag{1.2.10}$$

Determine the bandpass filter group delay response using fractional bandwidth (B) and centre frequency (f_0) .

$$\tau(f) = \frac{T(\Omega)}{2\pi B f_0}\left[1 + \left(\frac{f_0}{f}\right)^2\right] \tag{1.2.11}$$

1.3 Coupling Matrix

1.3.1 Circuit Model

Williams and Atia introduced the coupling matrix concept in references [41] and [1], focusing on dual-mode narrowband waveguide filters in the early 1970s. The coupling matrix concept abstracts the voltage-current relationships within the equivalent circuit frame work. In this context, we developed a prototype narrowband bandpass circuit model, depicted in Fig.(1.9) An open-circuit voltage source (e) with a source resistance (R) drives the circuit, which terminates at the load R_L. Transformers interconnect the lumped-element series resonators, constituting the circuit model. We monitor the current flowing through each series resonator. Every resonator is characterized by a self-inductance of $1H$ and a capacitance of $1F$. By normalizing the couplings for a bandwidth of $1rad/s$, we establish a central frequency of $1rad/s$, as cited in reference [3]. Due to the narrow band approximation, we assume that the mutual couplings linking each resonator with every other resonator remain constant across frequency.

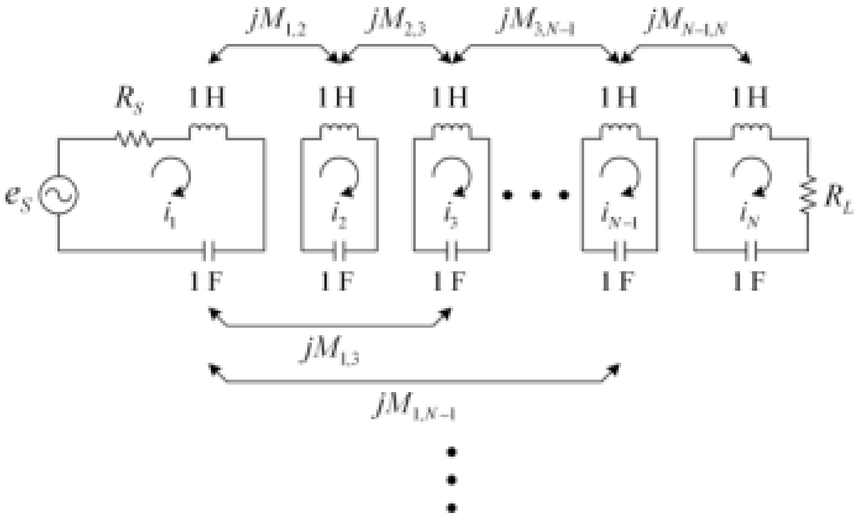

Figure 1.9: A prototype bandpass circuit intended for Nth-order filtration.

A prototype bandpass circuit shown in Fig.(1.9) represents the voltage-current relationship for each loop, which can be conveniently manipulated by describing it in matrix form as follows:

$$\begin{bmatrix} e_s \\ 0 \\ \vdots \\ 0 \\ 0 \end{bmatrix} = \begin{bmatrix} R_s + j(\omega - \frac{1}{\omega}) & jM_{1,2} & \cdots & jM_{1,N-1} & jM_{1,N} \\ jM_{1,2} & j(\omega - \frac{1}{\omega}) & \cdots & jM_{2,N-1} & jM_{2,N} \\ \cdots & \cdots & \ddots & \cdots & \cdots \\ jM_{N-1,1} & jM_{N-1,2} & \cdots & j(\omega - \frac{1}{\omega}) & jM_{N-1,N} \\ jM_{N,1} & jM_{N,2} & \cdots & jM_{N,N-1} & R_L + j(\omega - \frac{1}{\omega}) \end{bmatrix} \begin{bmatrix} i_1 \\ i_2 \\ \vdots \\ i_{N-1} \\ i_N \end{bmatrix} \tag{1.3.1}$$

The voltage-current relationship is given in (1.2.9) but simplified in the following way:

$$E = AI = (j(\omega - \frac{1}{\omega})U + R + jM)I, \tag{1.3.2}$$

The matrix E and the identity matrix U. represent the left side of Equation

(1.2.9). Not only are R, M matrices, and I.

$$I = \begin{bmatrix} i_1 \\ i_2 \\ \vdots \\ i_{N-1} \\ i_N \end{bmatrix}, \qquad R = \begin{bmatrix} R_s & 0 & \cdots & 0 & 0 \\ 0 & 0 & \cdots & 0 & 0 \\ \cdots & \cdots & \ddots & \cdots & \cdots \\ 0 & 0 & \cdots & 0 & 0 \\ 0 & 0 & \cdots & 0 & R_L \end{bmatrix} \tag{1.3.3}$$

$$M = \begin{bmatrix} 0 & jM_{1,2} & \cdots & jM_{1,N-1} & jM_{1,N} \\ jM_{1,2} & 0 & \cdots & jM_{2,N-1} & jM_{2,N} \\ \cdots & \cdots & \ddots & \cdots & \cdots \\ jM_{N-1,1} & jM_{N-1,2} & \cdots & 0 & jM_{N-1,N} \\ jM_{N,1} & jM_{N,2} & \cdots & jM_{N,N-1} & 0 \end{bmatrix} \tag{1.3.4}$$

The coupling matrix in this instance is denoted as matrix M. Every series resonator has an identical resonance frequency. Hence, a synchronously tuned circuit makes up the analogous circuit model filter. Fig.(1.10) shows how we changed the bandpass prototype to make an asynchronously tuned filter. We did this by giving each series resonator virtual parts that react constantly. The resonators' resonant frequency vary due to these fixed-frequency reactive components. In this instance, the coupling matrix provides.

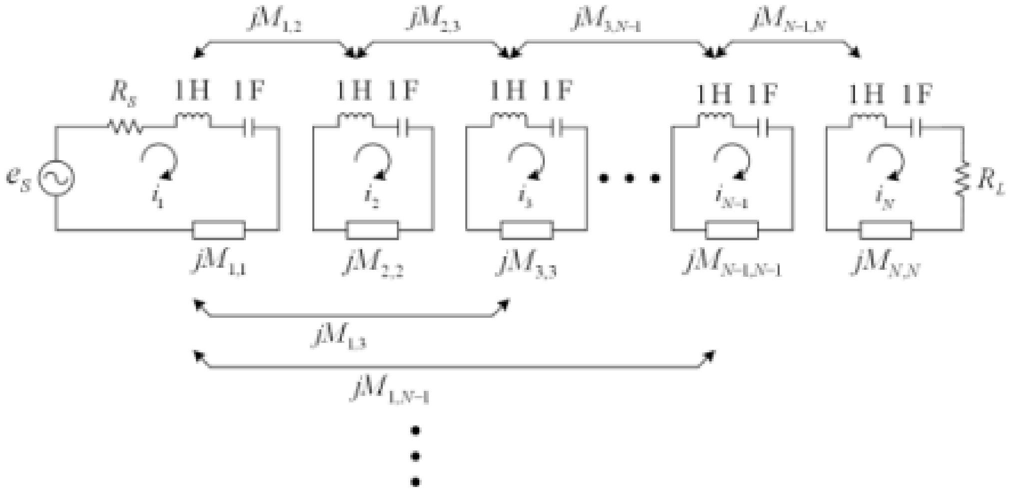

Figure 1.10: A prototype circuit for filtering using an Nth-order bandpass.

$$M = \begin{bmatrix} M_{1,1} & M_{1,2} & \cdots & M_{1,N-1} & M_{1,N} \\ M_{1,2} & M_{2,2} & \cdots & M_{2,N-1} & M_{2,N} \\ \cdots & \cdots & \ddots & \cdots & \cdots \\ M_{N-1,1} & M_{N-1,2} & \cdots & M_{N-1,N-1} & M_{N-1,N} \\ M_{N,1} & M_{N,2} & \cdots & M_{N,N-1} & M_{N,N} \end{bmatrix} \tag{1.3.5}$$

The goal of creating microwave resonator filters is to match a specific lowpass transfer function with a particular coupling matrix, source resistance (R_S) , and load resistance (R_L).

We must use lowpass terminology to represent the voltage-current relationship for the bandpass prototype. The bandpass prototype achieves the change frequency on lowpass to bandpass.

$$\Omega = \frac{\omega_0}{\Delta\omega}(\frac{f\omega}{\omega_0} - \frac{\omega_0}{\omega}) \tag{1.3.6}$$

The bandpass topology described in (1.3.6) can be expressed using low pass terminology, given that both the bandwidth ($\Delta\omega$) and centre frequency (ω_0) of the bandpass topology in Fig.(1.11) are one rad/s, with ω_0 denoting the centre frequency in rad/s and $\Delta\omega$ denoting the bandwidth in rad/s, respectively.

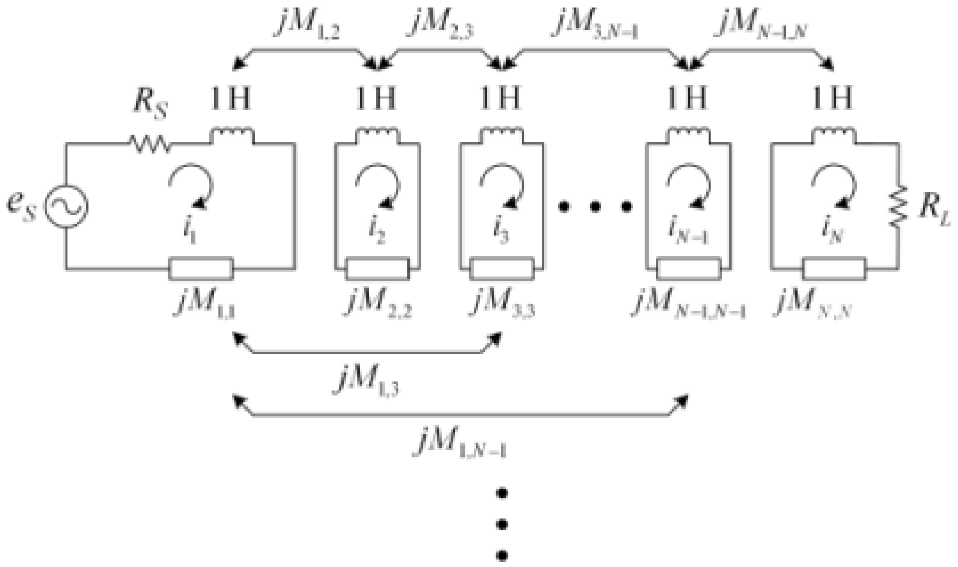

Figure 1.11: An Nth-order lowpass filter prototype circuit.

$$E = AI = (i\Omega + R + jM)I = (SU + R + jM)I, \tag{1.3.7}$$

By rearranging the series resonators via inductors, the bandpass prototype in Fig.(1.11) [43] can also be converted to the low pass prototype. It is clear that (1.3.4) is the outcome of the low pass prototype's voltage-current relationship in (1.11)

The $N \times N$ matrix in (**??**) [38] includes the values of the mutual couplings between the network's nodes. A direct connection occurs when there is a coupling between nodes with consecutive numbers. The self-couplings are the entries on the main diagonal, $Mi; i$, whereas the cross-couplings are the couplings between any consequentially numbered nodes. As previously stated, the self-couplings explain the variations in the resonant frequency among the various resonators. $Mi, j = Mj, i$ due to the passive network's reciprocity.

The diagonal matrix SU encompasses the frequency-variable part of the impedance for each loop. This forms an $N \times N$ matrix with all elements set to zero except for those on the diagonal, which are populated with $S = j\Omega$ as follows:

$$SU = \begin{bmatrix} S & 0 & \cdots & 0 & 0 \\ 0 & S & \cdots & 0 & 0 \\ \cdots & \cdots & \ddots & \cdots & \cdots \\ 0 & 0 & \cdots & S & 0 \\ 0 & 0 & \cdots & 0 & S \end{bmatrix} \tag{1.3.8}$$

Bandpass filters can add a positive real factor ε to S to account for the effect of then resonator's unloaded quality factor, Qu. In this case, ε equals $f_0/(BW \times Qu)$, where f_0 is the center frequency and BW is the design bandwidth.

1.3.2 Spreading Factor

The lowpass circuit prototype, seen in Fig.(1.12), is driven by an e_S volt voltage source and has an internal impedance of R_S ohms and a load impedance of R_L ohms. Impedance matrix A (Fig.(1.12)), which includes source and load terminations, depicts the circuit as a whole. Isolating this impedance matrix's strictly reactive and simply resistive components is also possible.

$$A = R + jM + SU = R + Z. \tag{1.3.9}$$

An impedance matrix Z represents a completely reactive network between a voltage source with an impedance of R_S and a load with an impedance of R_L. One can find the current in each loop by using Equation (1.2.10).

$$I = A^{-1}E \tag{1.3.10}$$

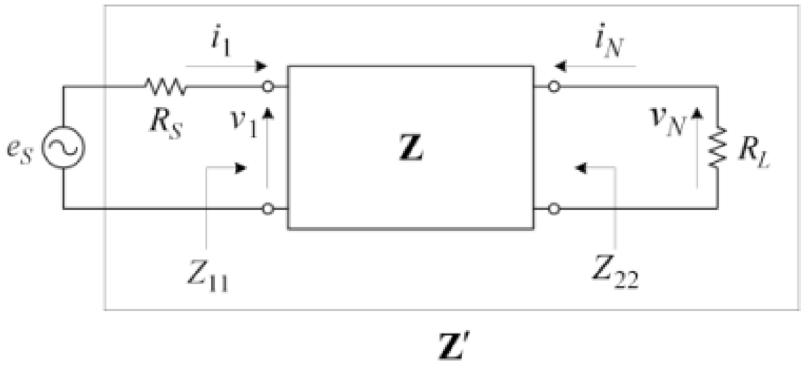

Figure 1.12: The impedance matrix A, which represents the whole circuit, and the impedance matrix Z.

Matrix A represents the source and load impedances in the network open-circuit impedance matrix. The inverse of then square matrix A is given by.

$$A^{-1} = \frac{adj(A)}{|A|} \tag{1.3.11}$$

where $[A]$ is the square matrix, A is a determinant, and $adj(A)$ is its adjoint. After subtracting row number i and column number j from A and multiplying by $(-1)_{i+j}$, the adjoint of the matrix is the transpose of the matrix whose $(i,\ j)$ entry is the cofactor $a_{i,j}$. It is essential to find the current in the first and last loops since there is one.

$$i_1 = A^{-1}_{N,1}Ei_1 = A^{-1}_{N,1}E = \frac{v_N}{R_L} \tag{1.3.12}$$

By entering (1.3.9) into the definition [38], one may determine the transmission coefficient S_{21}:

$$\begin{aligned} S_{21} &= 2\sqrt{\frac{R_S}{R_L}}.\frac{v_N}{e_s} \qquad (1.3.13) \\ &= 2\sqrt{\frac{R_S}{R_L}}.R_L A^{-1}_{N,1} \\ &= 2\sqrt{R_S R_L}.R_L A^{-1}_{N,1} \end{aligned}$$

Calculate the reflection coefficient at input port S_{11} using the following formula:

$$\begin{aligned} S_{11} &= \frac{Z_{11} - R_S}{Z_{11} + R_L}(1.62) \\ &= \frac{Z_{11} - R_S - 2R_S}{Z_{11} + R_S} \\ &= 1 - \frac{2R_S}{Z_{11} + R_S} \end{aligned} \tag{1.3.14}$$

With a potential divider and v_1 and i_1 as the equivalent values, determine the impedance Z_{11} at the input port.

$$Z_{11} = \frac{v_1}{i_1} = \frac{e_S Z_{11}}{Z_{11} + R_S} \cdot \frac{1}{e_S A^{-1}_{1,1}} \tag{1.3.15}$$

Which results in

$$\frac{1}{Z_{11} + R_S} = A^{-1}_{1,1} \tag{1.3.16}$$

Converting (1.3.13) into (1.3.11) defines the reflection coefficient at the input port.

$$S_{11} = 1 - 2R_S A^{-1}_{1,1} \tag{1.3.17}$$

Similarly, we calculate the reflection coefficient at the output port.

$$S_{22} = 1 - 2R_L A^{-1}_{N,N} \tag{1.3.18}$$

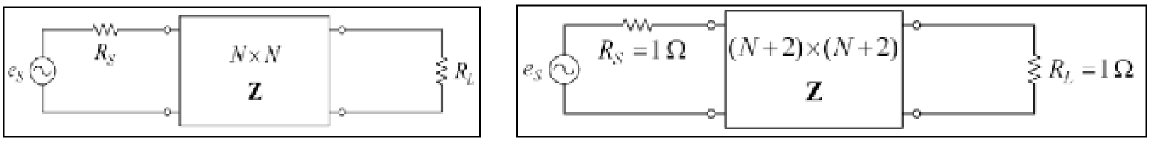

(a) (b)

Figure 1.13: The Nth-order filter in the circuit network is an $N \times N$ matrix and an $(N + 2) \times (N + 2)$ matrix.

You calculate the coupling matrix, R_S, and R_L to ensure that the S parameters (1.3.9) and (1.3.13) match the set insertion and return loss. Find the coupling matrix, R_S, and R_L to get the S parameters (1.3.9) and (1.3.13) and the set insertion and return loss to match. This is what filter synthesis is. One may use optimization techniques or analytical techniques to carry out filter synthesis. Analytical techniques synthesize a filter by equating the coefficients of $S(s)$ polynomials with those of (1.3.10). Optimization is another way to carry out this procedure [49].

1.3.3 The $(N + 2)$ Coupling Matrix Multiplied by $(N + 2)$

A normalization to unity impedance is achieved on the network's source and load sides using impedance inverters $M_{S,1}$, and $M_{N,L}$, which have respective R_S and R_L impedance values $\sqrt{R_S}\sqrt{R_L}$. To get a $(N + 2) \times (N + 2)$ matrix, you may absorb these inverters into an $N \times N$ matrix (Fig.(1.13)).

$$M = \begin{bmatrix} 0 & M_{S,1} & 0 & \cdots & 0 & 0 & 0 \\ M_{S,1} & M_{1,1} & M_{1,2} & \cdots & M_{1,N-1} & M_{1,N} & 0 \\ 0 & M_{1,2} & M_{2,2} & \cdots & M_{2N-1} & M_{2,M} & 0 \\ \vdots & \vdots & \vdots & \ddots & \vdots & \vdots & \vdots \\ 0 & M_{1,N.-1} & M_{2,N-1} & \cdots & M_{N-1,N-1} & M_{N-1,N} & 0 \\ 0 & M_{1,N} & M_{2N} & \cdots & M_{N-1,N} & M_{N,N} & M_{N,L} \\ 0 & 0 & 0 & \cdots & 0 & M_{N,L} & 0 \end{bmatrix} \tag{1.3.19}$$

In which $R_{N,L} = \sqrt{R_L}$, and $R_{S,1} = \sqrt{R_s}$. The core $N \times N$ matrix may include additional couplings between the source and load terminations and the internal nodes in addition to the couplings M_S, one, and $M_{N,L}$. Furthermore, one may integrate the directs source-load coupling $M_{S,L}$ to get canonical filter functions. The whole couplings $(N + 2) \times (N + 2)$ matrix is:

$$M = \begin{bmatrix} 0 & M_{S,1} & M_{S,2} & \cdots & M_{S,N-1} & M_{S,N} & M_{S,L} \\ M_{S,1} & M_{1,1} & M_{1,2} & \cdots & M_{1,N-1} & M_{1,N} & M_{1,L} \\ M_{S,2} & M_{1,2} & M_{2,2} & \cdots & M_{2N-1} & M_{2,M} & M_{2_r L} \\ \vdots & \vdots & \vdots & \ddots & \vdots & \vdots & \vdots \\ M_{S,N.-1} & M_{1,N.-1} & M_{2,N-1} & \cdots & M_{N-1,N-1} & M_{N-1,N} & M_{N-1,L]} \\ M_{S,N} & M_{1,N} & M_{2,N} & \cdots & M_{N-1,N} & M_{N,N} & M_{N,L} \\ M_{S,L} & M_{1,L} & M_{2,L} & \cdots & M_{N-1,L} & M_{N,L} & 0 \end{bmatrix} \tag{1.3.20}$$

The $(N + 2)(N + 2)$ coupling matrix lets you use full canonical filtering functions with Nth-degree characteristics and N fixed-frequency transmission zeros.

The following is an expression of the voltage-current relationship of the $(N+2) \times (N+2)$ coupling matrix:

$$\begin{aligned} E &= AI \\ &= (R + j\Omega W + jM)I, \end{aligned} \tag{1.3.21}$$

Where ω is comparable to the $(N+2) \times (N+2)$ identity matrix, with the exception of $W_{1,1} = W_{N+2,N+2} = 0$, and $I = [i_S,\ i_1,\ i_2, \cdots,\ i_L]^t$. where Iris a $(N+2) \times (N+2)$ matrix whose only nonzero entries are $R_{1,1} = R_{N+2,N+2} = 1$. These coefficients provide transmission and reflection in this instance.

$$S_{21} = 2.A^{-1}_{N+2,1} \tag{1.3.22}$$

and

$$S_{11} = 1 - 2.A^{-1}_{1}. \tag{1.3.23}$$

1.3.4 Diagram with Coupling-Routing

The model of the circuit prototypes, which derives the coupling matrix, describes the coupling mechanism of the cross-coupled filters. Examining which couplings between resonators are present and which are not feels awkward, but when using the circuit prototype. As a result, the coupling-routing diagram offers a practical means of viewing the filter's coupling structure.

Fig.(1.14) The diagram presents the coupling and routing of an eighth-order canonical structure filter. There are direct couplings between resonators whose numbers come aft er each other and cross-couplings between resonators whose numbers don't come aft er each other. The coupling-routing diagram of an $8th$-order canonical structure filter illustrates these direct and cross-couplings. Figure 1.15 shows the coupling-routing diagrams of a sixth-and eighth- order inline structural filter. Alternative names for the structures include cascaded quadruple and cascaded triplet structures

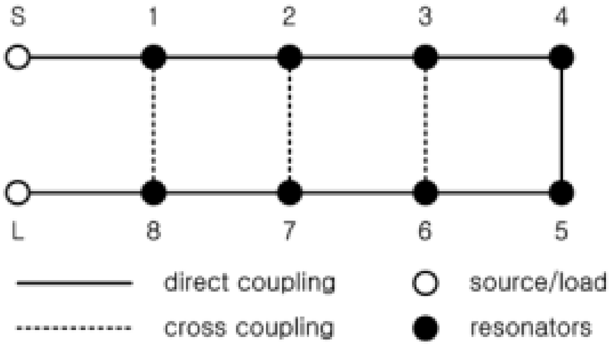

Figure 1.14: The canonical structure filter's coupling-routing diagram for the eighth order.

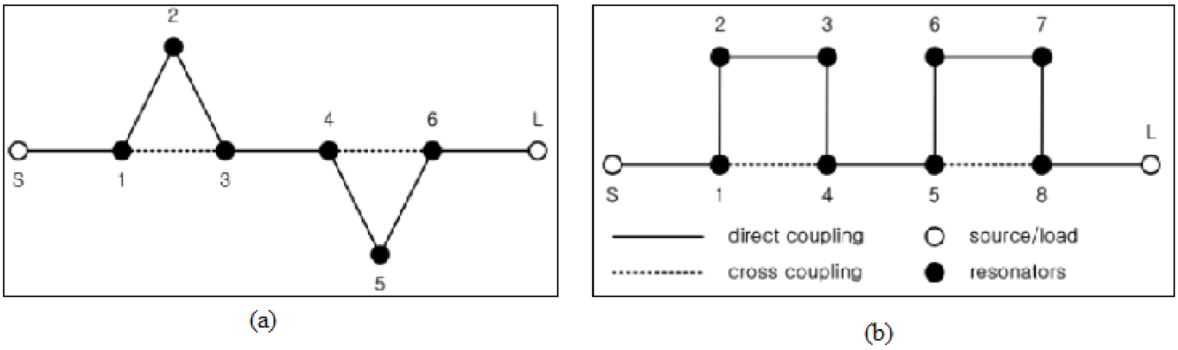

Figure 1.15: The canonical structure filter's coupling-routing diagram for the eighth order.

Cross-coupling may be used in these circumstances even if the source and load in Fig.(1.14) and Fig.(1.15) are not connected. Adding source-load coupling mainly results in more realizable gearbox zeros. The $8th$-order canonical structure filter in Fig.(1.14) can only yield a maximum of six transmission zeros. An eighth-order filter can achieve eight gearbox zeros while considering the source-load coupling.

The coupling-routing graphic explains the creation of transmission zeros and illustrates the relative phase shifts of various signal pathways. The source-load coupling [48] provides several representative examples, such as the cascaded-triplet, cascaded-quadruplet, and nested cross-coupling structures. With careful consideration, an eighth-order filter can achieve eight transmission zeros.

1.4 The Physical Components Involved in the Implementation of Microwave Filters

Choosing the physical components is one of the most crucial parts of filter implementation. It relies on several factors, including manufacturing prices, temperature drift, power handling capability, quality factor, frequency range, and physical dimensions [43]. Filter technologies such as dielectric resonators, printed circuits, lumped elements, and waveguide filters can be combined with different media.

Reactance's, lumped inducers, and lumped capacitances are the three major components of a filter. Designers can use only capacitors and inductors to design filters. Choosing which physical parts to use is a big part of making a filter. The filter's frequency range, dimensions, quality, Factor, power handling capability, temperature drift, and manufacturing cost [43] affect

Filter technologies such as dielectric resonator filters, printed circuit filters, lumped element filters, and waveguide filters, which can utilize various media. With unloaded quality filters in the hundreds of MHz, element filters typically run at hundreds of MHz. Given that they are much smaller than the operating wavelength, applying the lumped element filter effectively at high frequency is challenging. At higher frequency, designers must use dispersed components [43].

Waveguide technology implements microwave filters for low losses and excellent power handling. Rectangular and circular waveguide resonators with air fill and silver plating may reach a quality factor of 10000 to 20000. According to the parallel plate model [55], [54], the silver-plated gap, measuring 1 mm, can tolerate a peak voltage of up to $630V$. Significant progress in reducing mass, volume, and temperature drift is challenging to accomplish; however, since waveguide systems oft en exhibit poor temperature stability. [3] Engineers have adopted lighter materials like Kevlar instead of more traditional, heavy materials like metal. Moreover, we have effectively explored the use of graphite waveguide and carbon fibre technologies. A silver coating is oft en necessary for an appropriate quality factor when employing these lightweight materials. Inver has achieved impressive thermal stability.

Another microwave resonator is a compact cube or disc constructed of a material with a high dielectric constant but little loss. Theoretically, these dielectric resonators are comparable to cylindrical or rectangular waveguide resonators. The resonator will reduce a particular resonant mode's electric and magnetic fields to almost nothing within a small window of the free space wavelength if the dielectric constant is high. To minimize radiation loss, losses in the dielectric body mainly limit the resonator's unloaded quality factor [51]. Several engineers oft en use two types: Dual-mode filters are one of two types of filters using cylindrical dielectric resonators. When used in $HEII$ mode, two dual-mode filters may realize elliptic functions with little loss [16] Its volume is likewise lower. Because cylindrical dielectric resonators operate in the $TE_{01\delta}$ mode, the second kind of filter has a low-loss, flexible layout structure and is single-mode [34]. Dielectric resonator filters have several issues, including low power handling and poor spurious signal response.

Circuits combining microwaves and monolithic circuits integrating microwaves oft en utilize planar architectures. This group includes coplanar waveguide lines, microscopic lines, and strip lines. The planar structure resonator has numerous valuable features, including its compact size, simplicity in photolithography processing, and strong compatibility with active circuit parts. Using different substrate materials, planar structures can achieve a broad frequency range of applications. Nonetheless, the low-quality Factor of the planar structures is a significant disadvantage that makes applying them to narrowband filters challenging [36].

1.5 Conclusion

The chapter explores the role of polynomials in determining microwave filter characteristics, transmission and reflection coefficients, frequency responses, and characteristic functions of different filters. It categorizes filters into all-pole, transmission zero, and linear phase filters, with a special focus on transmission zeros. The chapter introduces the coupling matrix, a crucial component in designing and analyzing microwave filters, and its mathematical formulation. It also discusses the physical components of implementing microwave filters, including materials, technologies, and construction techniques. The chapter concludes with references for further exploration.

Chapter 2

Bandpass Rectangular Waveguide Filter

2.1 Introduction

A waveguide is a structure that confines the wave energy and guides the propagation of an electromagnetic wave in a specific direction. Resonators for waveguide are essential components in filter design. The waveguide features a discernible cutoff frequency that facilitates the transmission of electromagnetic energy above it while attenuating it below. In addition, waveguide propagation is characterized by distinct field patterns or modes. An infinite number of modes, each with its cutoff frequency, can coexist in any waveguide.

2.2 Rectangular Bandpass Waveguide Filter

A rectangular waveguide controls the propagation of electromagnetic waves by containing the wave energy. In general, a rectangular waveguide is comprised of a porous, cross-sectional metallic conduit (refer to Fig.(2.2.2)).

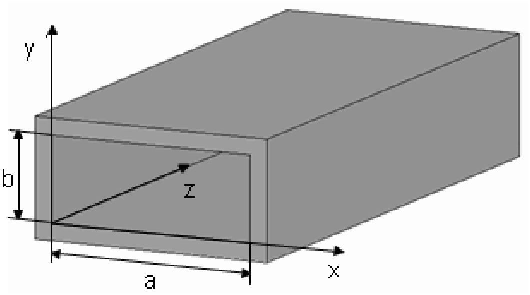

Figure 2.1: Configuration of a conventional rectangular waveguide [19]

We can determine the path of electromagnetic fields through a rectangular waveguide by applying the waveguide boundary condition to Maxwell's time-invariant field equations. The waveguide can support both transverse electric (TE) and transverse magnetic (TM) modes. These modes are illustrated by Maxwell's time-invariant field equations [21]. Due to the presence of a single conductor, TEM mode cannot pass through the waveguide. The relationship between these two kinds of modalities is independent.

2.2.1 Propagation Modes in Rectangular Waveguide

$E_z = 0$ denotes the transverse electric modes TE within a waveguide. In this case, solely the electric field is perpendicular to the direction of propagation and exclusively transverse; thus, the field components may be denoted as :

$$\begin{aligned}
(a) \qquad E_x &= \frac{j\omega\mu}{k_c^2}\frac{n\pi}{b}H_0\cos(\frac{m\pi x}{a})\sin(\frac{n\pi y}{b})e^{-j\beta c} \\
(b) \qquad E_y &= \frac{-j\omega\mu}{k_c^2}\frac{m\pi}{a}H_0\sin(\frac{m\pi x}{a})\cos(\frac{n\pi y}{b})e^{-j\beta c} \\
(c) \qquad H_x &= \frac{j\beta}{k_c^2}\frac{m\pi}{a}H_0\sin(\frac{m\pi x}{a})\cos(\frac{n\pi y}{b})e^{-j\beta c} \\
(d) \qquad H_y &= \frac{j\beta}{k_c^2}\frac{n\pi}{b}H_0\cos(\frac{m\pi x}{a})\sin(\frac{n\pi y}{b})e^{-j\beta c} \\
(e) \qquad H_z &= H_0\cos(\frac{m\pi x}{a})\cos(\frac{n\pi y}{b})e^{-j\beta c}
\end{aligned} \tag{2.2.1}$$

Denote as $TE_{mn}; (m,n)$ is acceptable values of $(0,1)$ and $(1,0)$, but not $(0,0)$. Simultaneously setting both m and n to zero would result in the elimination of the field components in equation (2.2.2). Therefore, TE_{10} can represent the lowest mode if $a > b$, and TE_{01} can represent it if $b > a$.

$Hz = 0$ denotes the transverse or normal magnetic field in the direction of propagation for transverse magnetic modes (TM modes). The field distribution is denoted by [26] [21].

$$\begin{aligned}
(a) \qquad E_x &= \frac{-j\beta}{k_c^2}\frac{m\pi}{a}E_0\cos(\frac{m\pi x}{a})\sin(\frac{n\pi y}{b})e^{-j\beta c} \\
(b) \qquad E_y &= \frac{-j\beta}{k_c^2}\frac{n\pi}{b}E_0\sin(\frac{m\pi x}{a})\cos(\frac{n\pi y}{b})e^{-j\beta c} \\
(c) \qquad E_z &= E_0\sin(\frac{m\pi x}{a})\cos(\frac{n\pi y}{b})e^{-j\beta c} \\
(d) \qquad H_x &= \frac{j\omega\varepsilon}{k_c^2}\frac{n\pi}{b}E_0\sin(\frac{m\pi x}{a})\cos(\frac{n\pi y}{b})e^{-j\beta c} \\
(e) \qquad H_y &= \frac{-j\omega\varepsilon}{k_c^2}\frac{n\pi}{b}E_0\cos(\frac{m\pi x}{a})\sin(\frac{n\pi y}{b})e^{-j\beta c}
\end{aligned} \tag{2.2.2}$$

Denote as TM_{mn}, the field vanish for TM_{00}, TM_{10} and TM_{01}.consequently The lowest mode is TM_{11}.

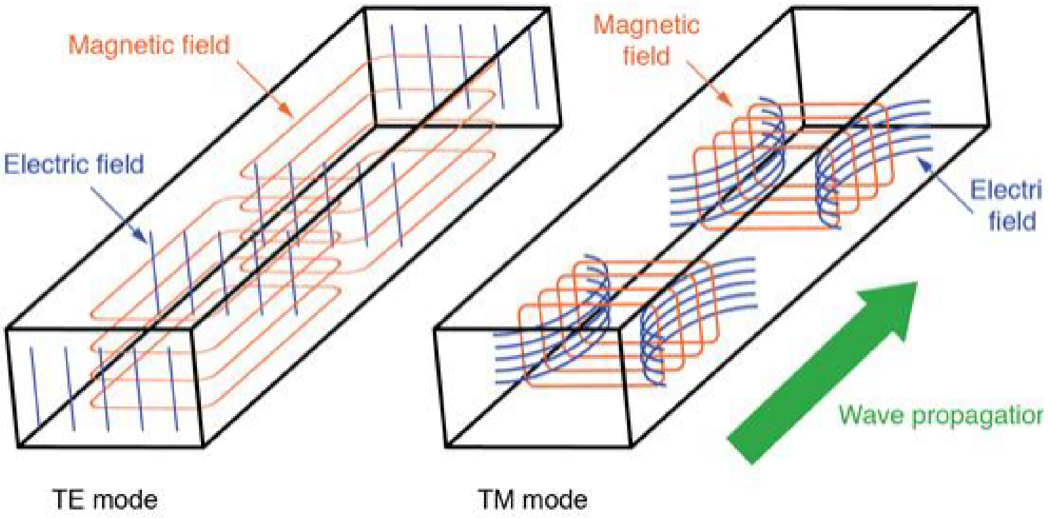

Figure 2.2: In the rectangular waveguide, general modes of propagation exist.

Mode and mode, respectively, are equivalent to the form of the TE and TM modes. The suffix "m" represents the quantity of half-wave fluctuations occurring in the field along the x-axis, while "n" signifies the quantity of half-wave fluctuations occurring along the y-axis.

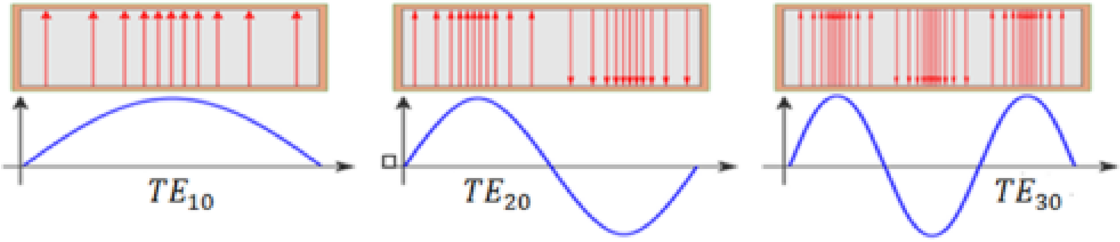

Figure 2.3: Variation in the E-field within a rectangular waveguide..

The graphical representation of the E field variation in a waveguide for the modes is illustrated in Fig.(2.3) The initial index represents the quantity of half-wave loops spanning the guide's width, whereas the second index denotes the loop count along the guide's height, which is zero in this particular instance.

2.2.2 Rectangular Waveguide TE and TM Mode Parameters

The formula for the cutoff wave number is as follows:

$$k_c^2 = \gamma^2 + k^2 = (\frac{m\pi}{a})^2 + (\frac{n\pi}{b})^2 \tag{2.2.3}$$

γ is the constant of propagation.

$$\gamma^2 = \sqrt{\left(\frac{m\pi}{a}\right)^2 + \left(\frac{n\pi}{b}\right)^2 - k_c^2} \tag{2.2.4}$$

Where

$$k = \omega\sqrt{\mu\varepsilon} \tag{2.2.5}$$

It is crucial to note that although both the TE and TM mode shave the ability to traverse the waveguide, the propagation constant ($\gamma = \alpha + j\beta$) establishes three distinct values for ka (or ω), m, and n, regardless of then mode type [19]:

Cutoff mode ($\gamma = 0$ or $\alpha = \beta = 0$) :

$$k^2 = \omega^2\mu\varepsilon = \left(\frac{m\pi}{a}\right)^2 + \left(\frac{n\pi}{b}\right)^2 \tag{2.2.6}$$

Currently, ω is referred to as the cutoff angular frequency.

$$\omega_c = \frac{1}{\sqrt{\mu\varepsilon}}\sqrt{\left(\frac{m\pi}{a}\right)^2 + \left(\frac{n\pi}{b}\right)^2} \tag{2.2.7}$$

The evanescent state ($\gamma =$aeore $\beta = 0$).

$$k^2 = \omega^2\mu\varepsilon < \left(\frac{m\pi}{a}\right)^2 + \left(\frac{n\pi}{b}\right)^2 \tag{2.2.8}$$

No propagation occurs under our control. Evanescent refers to these modes that do not propagate or diminish.

Propagation mode ($\gamma = j\beta \; or \; a = 0$) :

$$k^2 = \omega^2\mu\varepsilon > \left(\frac{m\pi}{a}\right)^2 + \left(\frac{n\pi}{b}\right)^2 \tag{2.2.9}$$

Where the phase constant β becomes:

$$\beta = \sqrt{k^2 - \left(\frac{m\pi}{a}\right)^2 - \left(\frac{n\pi}{b}\right)^2} \tag{2.2.10}$$

As a result, the cutoff frequency fc_{mn} for each mode (a combination of m and n) is as follows:

$$fc_{mn} = \frac{k_c}{2\pi\sqrt{\mu\varepsilon}} = \frac{1}{2\pi\sqrt{\mu\varepsilon}}\sqrt{\left(\frac{m\pi}{a}\right)^2 + \left(\frac{n\pi}{b}\right)^2} \tag{2.2.11}$$

The cutoff frequency determines the minimum excitation frequency at which attenuation occurs and the maximum frequency at which propagation occurs within a waveguide.

It is possible to express the propagation constant γ in relation to the cutoff frequency f_c as follows:

$$\gamma = \begin{cases} j\beta = j\omega\sqrt{\mu\varepsilon}\sqrt{1-\left[\dfrac{f_c}{f}\right]^2} & f > f_c \\ \alpha = \omega\sqrt{\mu\varepsilon}\sqrt{1-\left[\dfrac{f}{f_c}\right]^2} & f < f_c \end{cases} \tag{2.2.12}$$

For a given operating frequency f, modes exceeding the cutoff frequency $(f > fc)$ are capable of propagating (propagation mode), while waves falling bello the cutoff frequency $(f < fc)$ undergo attenuation in thee-direction (evanescent modes). Without wave propagation or attenuation, neither cutoff frequency nor operating frequency interference occurs $(f = fc)$. By way of definition, transverse resonance is the generation of a stationary wave in the transverse direction. Every mode of propagation possesses the ability to characterize the corresponding fundamental wavelength.

$$\lambda_c = \frac{2\pi}{\sqrt{\left(\dfrac{m}{a}\right)^2 + \left(\dfrac{n}{b}\right)^2}} \tag{2.2.13}$$

For the associated propagation constant β, the cutoff frequency fc_{as} serves as an equivalent representation.

$$\beta = \omega\sqrt{\mu\varepsilon}\sqrt{1-\left[\frac{f_c}{f}\right]^2} \tag{2.2.14}$$

The initial four modes of the WR-90 wave guide, filled with air and has $a = 22.86$ mm and $b = 10.16$ mm in dimensions, are being analyzed.

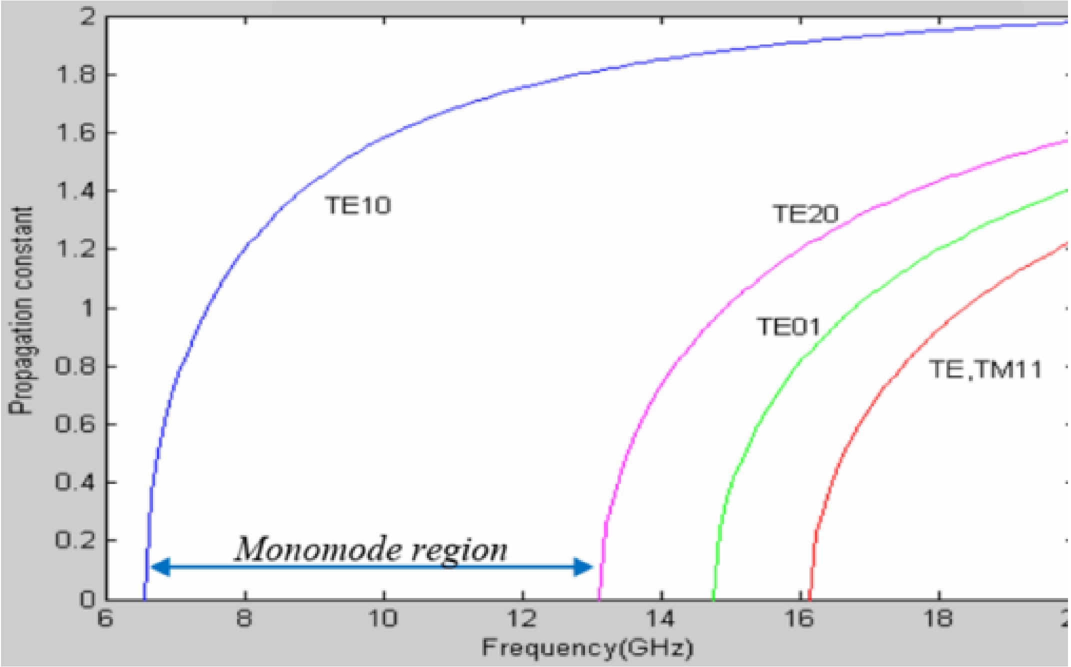

Figure 2.4: For the initial four modes, the variation in propagation remains constant concerning frequency.

As illustrated in Fig.(2.4), the mode propagates exclusively under the conditions that the operating frequency exceeds its cutoff frequency and the propagation constant is real. As previously stated, microwave waveguide and associated apparatus are commonly employed in a mono mode configuration, wherein the propagation occurs in only one mode. Working within a frequency region characterized by the propagation of only the first mode (TE_{10}), denoted as a mono mode region in the figure, is more practical.

The guide wavelength is the distance required in the z-direction of propagation to induce a 2π phase change. Thus, for each mode of propagation occurring at the operational frequency f_0:

$$\lambda_g = \frac{\lambda_o}{\sqrt{1-(f_c/f)^2}} \tag{2.2.15}$$

Where λ_0 is the free space wavelength.

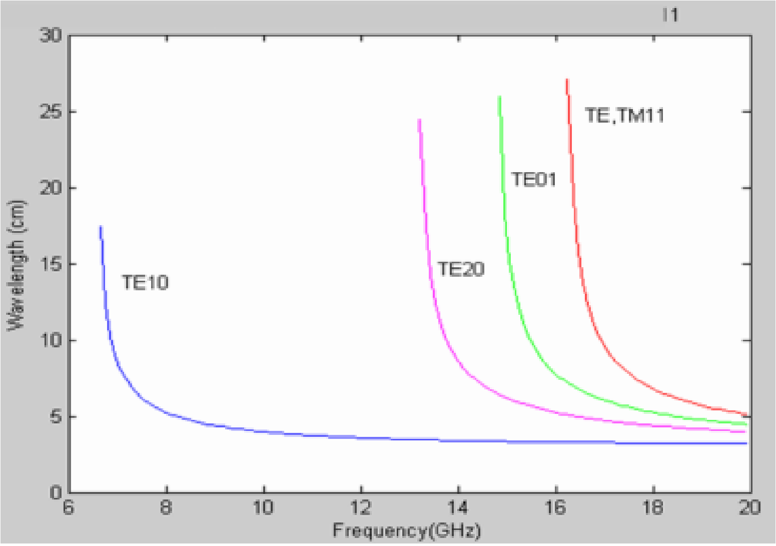

Figure 2.5: Variation of wave length with frequency for the first four modes.

The wave impedance represents relationships between the electric and magnetic fields within the waveguide. The origin of the wave impedance is [19] :

$$\eta_{TE}\frac{-E_x}{H_y} = \frac{\eta_0}{\sqrt{1-(f_c/f)^2}} = \eta_0\frac{\lambda_g}{\lambda_o} \tag{2.2.16}$$

$$\eta_{TM}\frac{-E_\chi}{H_y} = \eta_0\sqrt{1-(f_c/f)^2} = \eta_0\frac{\lambda_0}{\lambda_g} \tag{2.2.17}$$

Where η_0 is the free space wave impedance.

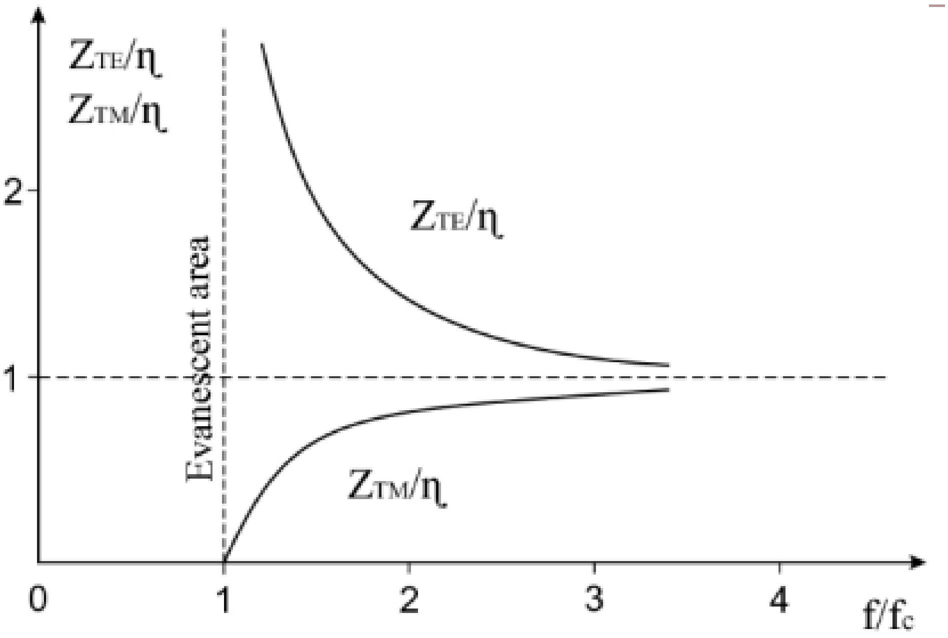

Figure 2.6: Variation of wave impedance with frequency for TE and TM modes.

2.2.3 Dominant TE_{10} mode

Principal mode, or dominant mode, refers to the mode characterized by the lowest cut- off frequency. By convention, the width an of a conventional rectangular waveguide is double the height b. The lowest frequency is attained when $m = 1$ and $n = 0$ (TE_{10} is the dominant mode of then rectangular waveguide), as indicated by equation (2.2.11).

The expressions for the cutoff frequency f_c, cutoff wavelength λ_c , and phase constant β for the TE_{10} mode are as follows:

$$fc = \frac{1}{2a\sqrt{\mu\varepsilon}} \tag{2.2.18}$$

$$\lambda_c = 2a\sqrt{\mu\varepsilon} \tag{2.2.19}$$

$$\beta = \sqrt{\omega^2\mu\varepsilon - \left(\frac{\pi}{a}\right)^2} \tag{2.2.20}$$

As the waveguide is filled with air or vacuum, the cutoff frequency and wavelength are modified as follows:

$$fc = \frac{c}{2a}(2.21) \tag{2.2.21}$$

$$\lambda_c = 2a(2.22) \tag{2.2.22}$$

$$\beta = \frac{2\pi}{\lambda_g}(2.23) \tag{2.2.23}$$

Where c is the speed of light in vacuum.

The cross-sectional measurements of an air-filled X-band rectangular wave guide ($WR90$) are $a = 22.86$ mm and $b = 10.16$ mm. Consequently, the fundamental mode's cutoff frequency is as follows:

$$fc = \frac{c}{2a} = 6.56\ GHz \tag{2.2.24}$$

Figure (2.7) presents the mode chart, which illustrates the relative cutoff frequency for the initial six modes of an air-filled rectangular waveguide ($WR90$).

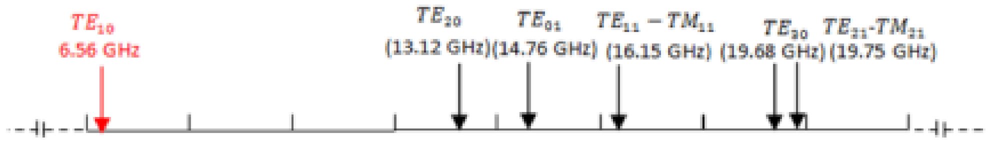

Figure 2.7: Mode chart WR-90 waveguide.

The waveguide is capable of propagating solely the TE_{10} mode within the X-band range of $\approx 8.2-12.5\ GHz$. This is commonly referred to as single-mode operation, and it is where hollow waveguide are most effectively utilized.

2.3 Waveguide resonators

When waveguide are employed at high frequency, lumped-element tuned circuits (RLC circuits) demonstrate significant inefficiency. Unwanted radiation from the circuit initiates when the element dimensions approach a correspondence with the wavelength. In situations where the dimensions of conventional circuit elements approach the wavelength, engineers opt to employ waveguide resonators as an alternative means of preventing the ingress of undesired radiation into the circuit.

A tuned circuit at high frequency can be constructed using a lumped-element RLC circuit. Conducting walls enclose a section of rectangular waveguide on ends, thereby forming the rectangular waveguide resonator and establishing an enclosed conducting box.

Depicting the resonator modes, the conducting walls affixed to the waveguide's extremities generate standing waves by reflecting the waveguide modes in both the $+z$ and $-z$ directions back and forth within the resonator.

In order for the tangential components of the electric field to cease to exist at the end- walls, it is necessary that these walls align with zero crossings of the standing wave. Alternatively stated, $d = p\lambda_c/2 = p\pi/\beta$, where is a non-zero integer, can be expressed as an integral multiple of half-wavelengths that fits along the z-axis. This establishes the following condition regarding the propagation constant:

$$\beta = \frac{p\pi}{d} \tag{2.3.1}$$

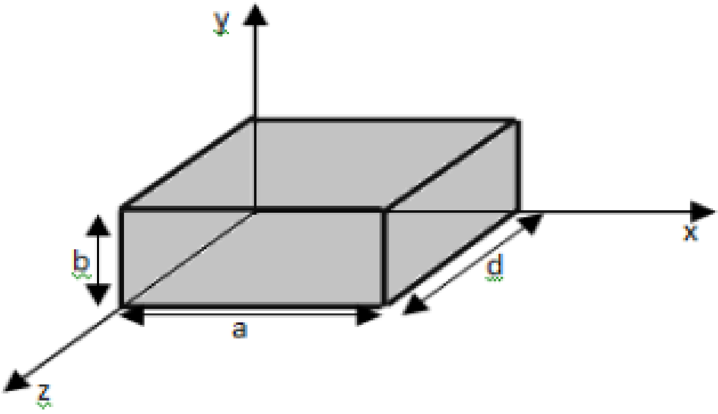

Figure 2.8: Rectangular cavité.

This can only occur for discrete values of K_0.

$$K_0 = \sqrt{\left(\frac{m\pi}{a}\right)^2 + \left(\frac{n\pi}{b}\right)^2 + \left(\frac{p\pi}{d}\right)^2} \tag{2.3.2}$$

These particular values of K_0 give the resonant frequency of the cavity:

$$f_{m,n,p} = \frac{k_0}{2\pi\sqrt{\mu\varepsilon}} = \frac{1}{2\pi\sqrt{\mu\varepsilon}}\sqrt{\left(\frac{m\pi}{a}\right)^2 + \left(\frac{n\pi}{b}\right)^2 + \left(\frac{p\pi}{d}\right)^2} \tag{2.3.3}$$

At $p = 1$, the TE_{10} mode is capable of delivering the minimum resonant frequency. Consequently, the resonant mode is the lowest TM_{101} resonant mode. It is important to mention that the resonant frequency can be achieved with identical dimensions, cross sections of the waveguide, and cavity length.

2.4 Discontinuities in Waveguide

Constructing a filter involves placing various types of obstacles along the waveguide. The job instructions are termed reactive elements of the waveguide. The prior reactance nature, whether inductive or capacitive, is determined by the axis along which they are placed inside the waveguide. If an obstacle exhibits TM modes, there is An accumulation of electrical power at the discontinuity due to the appearance of higher-order modes that vanish; in this case, the discontinuity is capacitive. On the other hand, if TE modes appear, the discontinuity is inductive. The most basic type of discontinuity is "iris".

Designers can arrange these discontinuities inside the waveguide to create a filter. The most basic configurations of the discontinuities of waveguide filters are as follows:

2.4.1 Inductive Iris

The most common type of reactive discontinuity used in rectangular wave guides is

the Inductive Iris. In this configuration, metallic collates line across the sides of the rectangular waveguide. Placing them along Hx and across Hz produces an inductive effect. Fig.(2.9) illustrates an inductive iris and its equivalent.

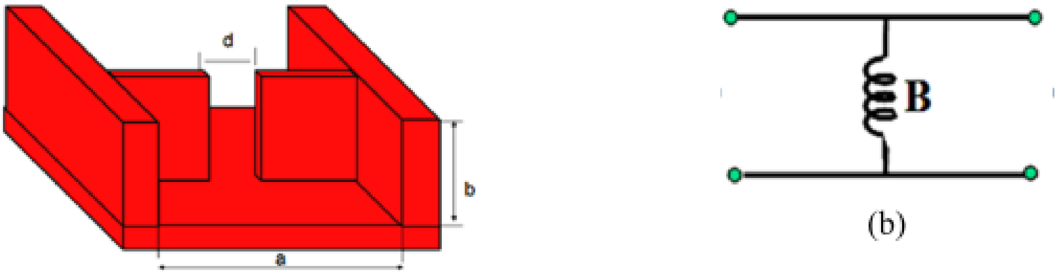

(a)

(b)

Figure 2.9: (a) An inductive iris-based rectangular waveguide filter. (b) an equivalent circuit. By, one can determine the correlation between the normalized susceptance B inductive irises and the distance d between them .

Where

$$\beta = \sqrt{w^2 \varepsilon \mu - (\frac{\pi}{a})^2}, \quad \gamma_3 = \sqrt{(\frac{3\pi}{a})^2 + w^2 \varepsilon \mu} \tag{2.4.1}$$

Another equation of this relationship found in literature is:

$$B = \frac{\lambda_Z}{a} \cot^2(\frac{\pi d}{2a}) \tag{2.4.2}$$

These equations provide a same response. The latter equation is used in this chapter.

Using $\lambda_Z = \lambda_{g_0}$.

Following is the solution of equation (2.4.2) for.

$$d = \frac{2a}{\pi} \cot^{-1} \left[\sqrt{\frac{aB}{\lambda_{g_0}}} \right] \tag{2.4.3}$$

2.4.2 Capacitive Iris

A capacitive effect is generated along E_y in this particular arrangement where metallic plates are arranged in a line on the upper and lower sides of the rectangular waveguide. When positioned along E_y, these components generate a capacitive effect. The a fore mentioned arrangement is illustrated in Fig.(1.1.10).

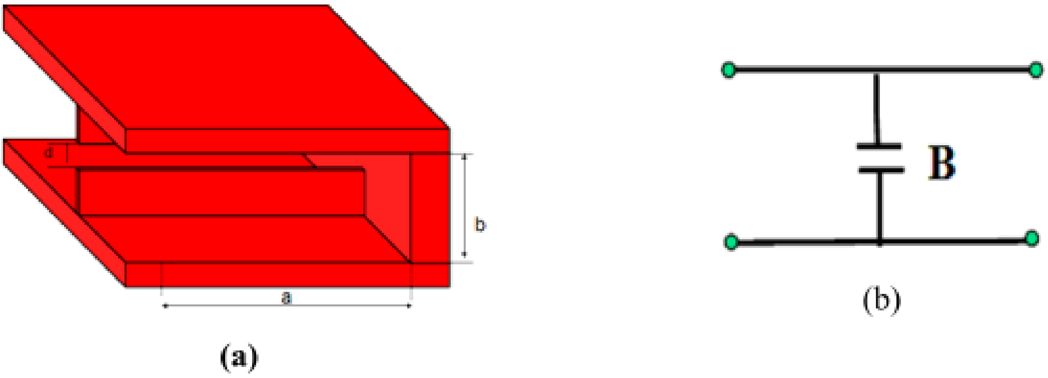

Figure 2.10: (a) Rectangular waveguide filter based on Capacitive Iris. (b) Equivalent Circuit..

Defines the correlation between the distance d between the capacitive sees and the normalized susceptance B.

$$B = \frac{2\beta b}{\pi}\ In\ (\csc(\frac{\pi d}{2b}) + (\frac{2\pi}{b\gamma_2} - 1)\cos^4(\frac{\lambda d}{2b})) \tag{2.4.4}$$

Where

$$\gamma_2 = \sqrt{\left(\frac{2\pi}{b}\right)^2 - \beta^2} \tag{2.4.5}$$

The alternative equation that provides the most accurate approximation for is as follows:

$$B = \frac{4b}{\lambda_Z}\ln(\csc(\frac{\pi d}{2b})) \tag{2.4.6}$$

Equation (2.4.6) has been incorporated into the final calculations. The solution to this equation for d is given by the subsequent equation (2.4.7).

$$d = \frac{2b}{\pi\sin^{-1}(\exp(\frac{B\lambda_{g0}}{4b}))} \tag{2.4.7}$$

2.5 Wavelength Transformation

When describing the wave within the waveguide, the prototype low pass transformation of wavelength is utilised to model a bandpass filter considerably more precisely than frequency. Effectively, the cut-off wavelength corresponding to the waveguide cut-off frequency is incorporated into the response.

$$\Omega = \frac{-1}{\Delta}\left(\frac{\lambda_{g0}}{\lambda_g} - \frac{\lambda_g}{\lambda_{g0}}\right) \tag{2.5.1}$$

Where

$$\begin{aligned}
(a) \qquad \lambda_C &= \frac{2ab}{\sqrt{(mb)^2 - (na)^2}} \quad , \qquad \lambda_g = \frac{1}{\sqrt{\left(\frac{f}{c}\right)^2 - \left(\frac{1}{\lambda_C}\right)^2}} \\
(b) \qquad \lambda_{g0} &= \frac{1}{\sqrt{\left(\frac{f}{c}\right)^2 - \left(\frac{1}{\lambda_C}\right)^2}}, \quad \lambda_{g1} = \frac{1}{\sqrt{\left(\frac{f}{c}\right)^2 - \left(\frac{1}{\lambda_C}\right)^2}}, \\
\lambda_{g2} &= \frac{1}{\sqrt{\left(\frac{f}{c}\right)^2 - \left(\frac{1}{\lambda_C}\right)^2}}
\end{aligned} \tag{2.5.2}$$

Equations (2.5.1), wherein $\triangle in$ represents the fr action bandwidth, define $\triangle$ is as follows $\Delta = \frac{\lambda_{g_1} - \lambda_{g_2}}{\lambda_{g0}}$, the guide wavelengths at the band-edge frequency are denoted as λ_{g_1} and λ_{g_2}, while λ_{g_0} represents the guide wavelength at the center frequency.

2.5.1 Comparison of Different Transformation

The performance of the aforementioned operations is represented and compared in the context of a fourth-order Tchebychev bandpass filter.

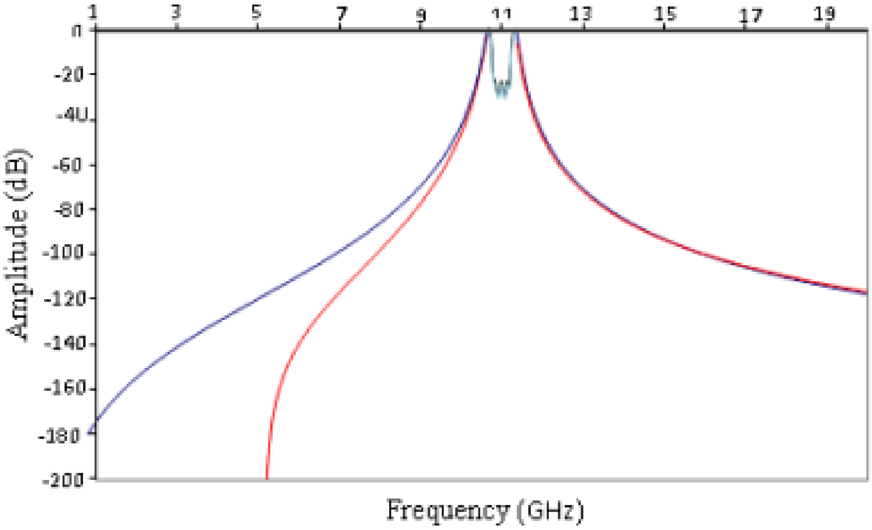

Figure 2.11: Band pass filters associated with two transformations.

The bandwidth of the two transformations seems to be precisely concurrent. Nevertheless, beyond the band, wavelength transformation considerably more accurately represents the actual filter. The frequency of 5.5 GHz is evident in this context, below which no wave can propagate further.

2.6 Filter Synthesis the Direct Coupling Bandpass Filter is a Rectangular Waveguide Design

From synthesis to electromagnetic simulation, we develop the design procedure. We implement the filter design using waveguide technology with an inductive iris coupling aperture. Two methods were used to evaluate the equivalent susceptance of the iris aperture: the first method is based on classical synthesis, while the second method utilizes the K- impedance inverter circuit model with an EM simulator. We carried out validations for both methods using the Ansoft -HFSS electromagnetic simulator, as well as the presented experimental results.

2.6.1 Filter Design in Rectangular Waveguide Configuration "in-Line"

In this example, the Extraction of the Admittance Technique is used to construct and optimize a $4th$-order combined bandpass filter. A rudimentary electromagnetic filter model based on a Tchebychev lowpass prototype with frequency transformation is created using $HFSS$ and AWR simulators [9]. The technique for extracting the multiport admittance matrix (Y matrix) is based on adding more internal ports to the filter's design. The Coupling matrix is used to create the filter polynomial features from the simulated scattering parameters [10]. A fine filter model with the best physical dimensions and the best frequency response is created after multiple iteration [47]. Compared to manual experience tuning, an admitance technique extracting system allows for faster tuning of then optimal filter.

2.6.2 Filter Designing Specifications

The specifications imposed for this filter are as Table (2.1). The circuit that will be synthesized is defined in Environment 16 as a distributed element bandpass filter [47]. We started the design of the $4th$-order filter with a study on volumetric technology. We have chosen waveguide technology; knowing the maximum ripple of 0.04321 dB and the specifications defined in the specifications, we obtain the

Function	Tchebychev
Filter order	04
center frequency f_0	10.5 GHz
Bandwidth (BW) at $-3\ dB$	950 MHz
Amplitude of the Lar ripple (passband ripple)	0.01 dB
return loss : RL	$< -20\ dB$

Table 2.1: The following specification of the filter ideal response of the Tchebychev bandpass filter of order 4.

coefficients gi ($i = 1{-}4$) of the band- pass prototype of the type filter Tchebychev:

0	g_1	g_2	g_3	g_4	g_5
1	0.7129	1.2004	1.3213	0.6476	1.1008

Using the specifications defined in the specifications, the matrix and the external quality factors for the coupled resonators are calculated from [19]:

$$\omega_0 = 2\pi f_0 \tag{2.6.1}$$

$$Q_e = \frac{g_0 g_1}{FBW} \text{ , } Q_{en} = \frac{g_n g_{n+1}}{FBW} \tag{2.6.2}$$

$$M_{i,i+1} = \frac{FBW}{\sqrt{g_i g_{i+1}}} \tag{2.6.3}$$

The synthesis of this specification is of order four such that the coupling matrix is [39]:

$$[m] = \begin{bmatrix} 0 & 0.0978 & 0 & 0 \\ 0.0978 & 0 & 0.0718 & 0 \\ 0 & 0.0718 & 0 & 0.0978 \\ 0 & 0 & 0.0978 & 0 \end{bmatrix} \tag{2.6.4}$$

$$Q_e = \frac{g_0 g_1}{FBW} = \frac{1 * 0.9314}{0.095} = 9.8042 \tag{2.6.5}$$

Table 1: Elements and values of then assoc at on matrix $M(i, i+1)$

M_{12}	M_{23}	M_{34}	$Q_e = Q_s$
0.0978	0.0718	0.0878	9.842

The filter specifications translate into desired coupling matrix elements $m(i, i{+}1)$, Q_{e1} and Q. Where the lumped elements $R_0 L_0 c_0$ represent the four synchronously tuned resonators and the quarter-wave transmission lines, which have electrical length $EL = \pm 90^0$ at the center frequency f_0, the corresponding design parameters for the band-pass filter are:

Lumped elements $R_0 L_0 c_0$ of resonators [9]:

$$L_0 = \frac{Z}{\omega_0 Q_e} 10^9 nH = 5.0372 \quad nH \tag{2.6.6}$$

$$C_0 = \frac{Q_e}{\omega_0 Z} 10^{12} pF = 4.5611 \quad pF \tag{2.6.7}$$

$$R_0 = 100000\ \Omega \tag{2.6.8}$$

The impedances of the resonators [9]:

$$Z_{i,i+1} = \frac{Z}{Q_e M_{i,i+1}} \tag{2.6.9}$$

When $Z_0 = 50\Omega$ is the supply impedance at the I/O ports:

$$Z_{12} = 58.8889\ \Omega,\quad Z_{23} = 76.6390\ \Omega,\ Z_{34} = 58.8876\ \Omega \tag{2.6.10}$$

The band-pass filter prototype operates using the characteristic impedance of the positive quarter-wave resonator lines, and parallel $R_0 L_0 c_0$ resonant circuit. After calculating the elements of the series and parallel branches, the equivalent circuit of the filter is shown in Fig.(2.12) [23].

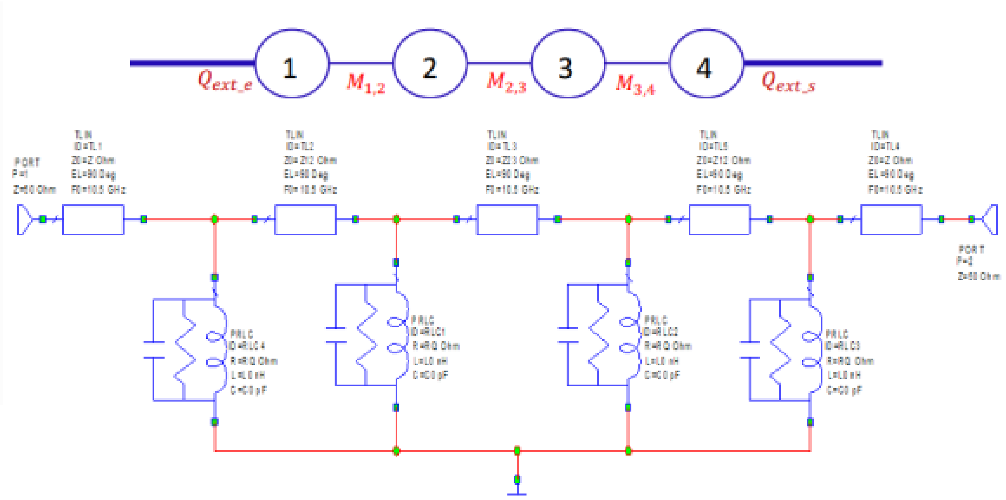

Figure 2.12: The equivalent circuit of bandpass filter order 4.

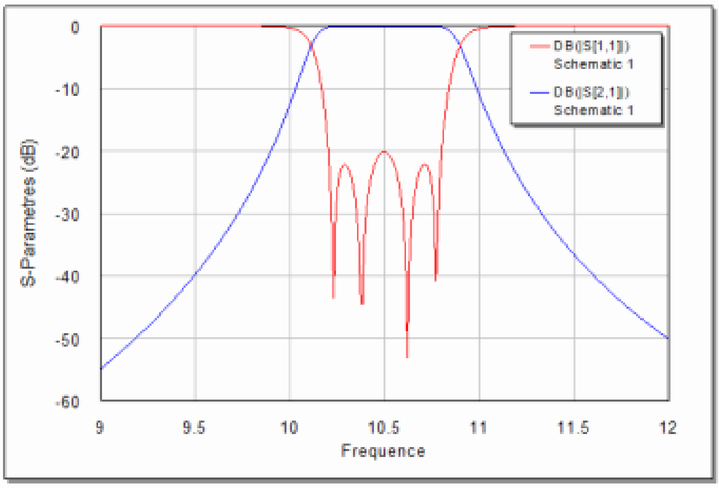

Figure 2.13: Ideal response of the Tchebychev bandpass filter of order 4.

2.6.3 Derivation and Extraction of External Quality Factor

The structure using a coaxial line illustrated in Fig.(2.14). is typical for the volume filter with coupled resonators. The coupling line, generally with a characteristic impedance of 50 Ω, is

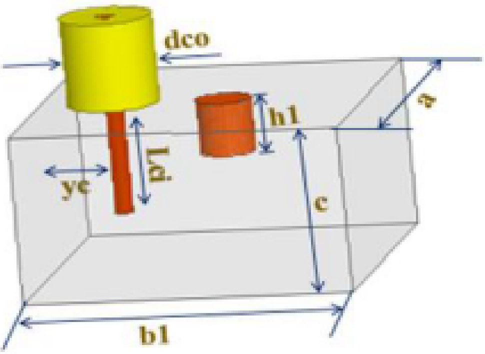

Figure 2.14: Coaxial line coupling structures for coupled resonator volume filters.

Connected to the resonators and the quality factor is controlled by the length dco and *dco*. The quality factor value determined by the phase of S_{11} is ([21]):

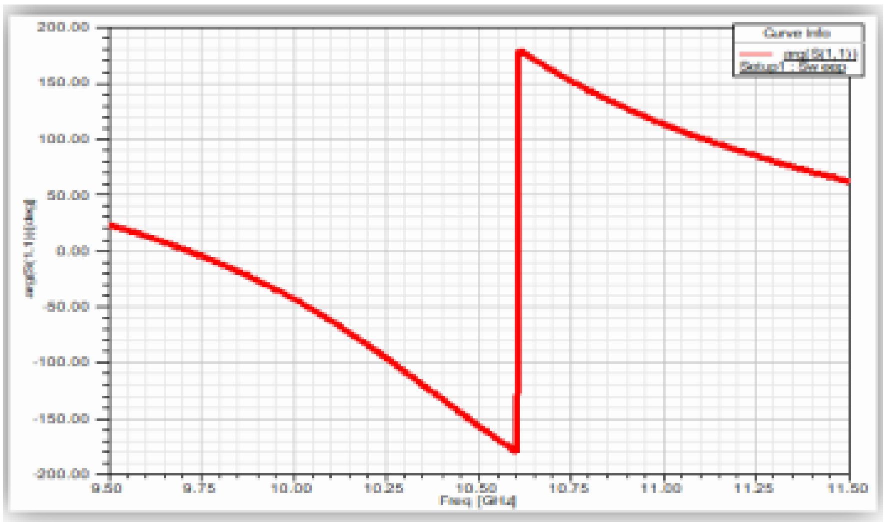

Figure 2.15: Phase response of the volume resonator for dimensioning the quality factor.

$$Q_e = Q_s = \frac{\omega_0}{\Delta\omega_{\pm 90}} = \frac{f_0}{f_2 - f_1} = \frac{10.60}{11.19 - 10.22} = 10.92 \tag{2.6.11}$$

The quality factor was determined by the reflection coefficient group delay S_{11} the group delay result is shown in Fig.(2.16).

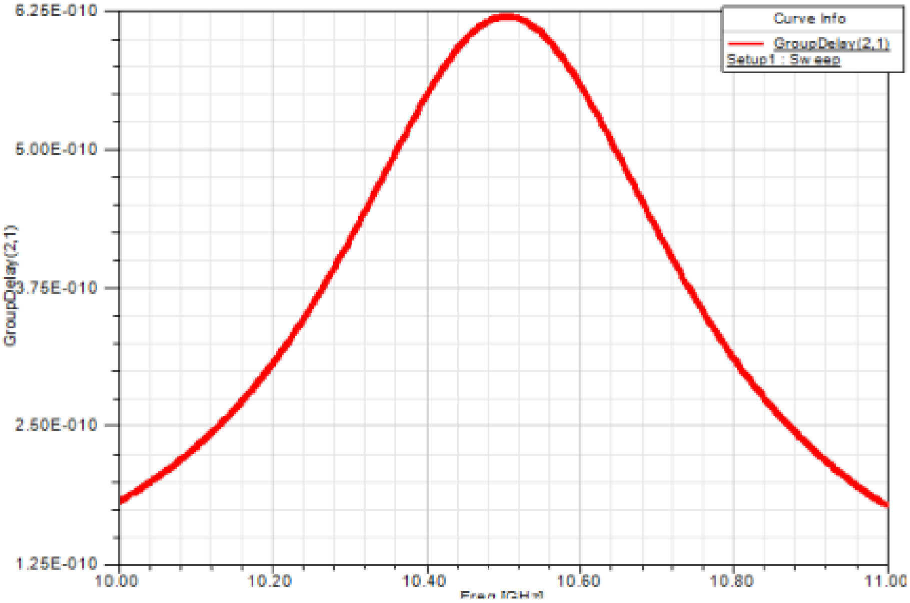

Figure 2.16: Transmission response of then doubly charged volume resonator for dimensioning the quality factor.

The values of the group delay and of the quality coefficient at the resonant frequency are calculated from the curve in Fig.(2.16), and are estimated at:

$$Q_e = Q_s = \frac{\omega_0 \tau_{s_{21}}(\omega_0)}{4} = \frac{2.\pi.10.5.10^9.6.25.10^{-10}}{4} \qquad (2.6.12)$$

2.6.4 Second-order filter with mixed coupling

The extraction of the coupling coefficient between the two resonators miscarried out by coupling the excitation and load inputs to the two resonators, which makes it possible to obtain two resonance peaks. The coupling structure is shown in the following figure:

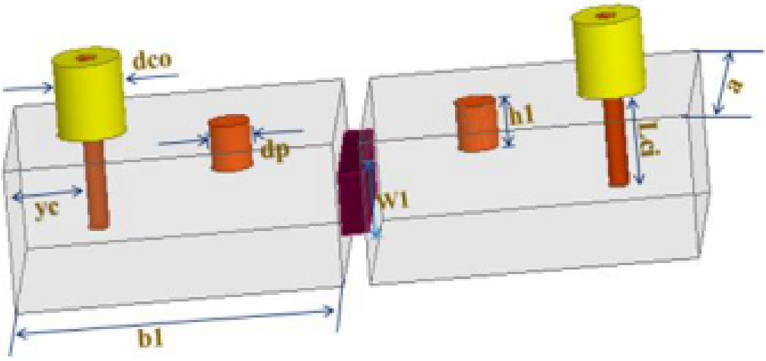

Figure 2.17: Structure of two coupled resonators (the first and the second).

The frequency response of the structure in the simulated figure below shows the two resonance peaks used to evaluate the coupling coefficient between the first and the second resonator.

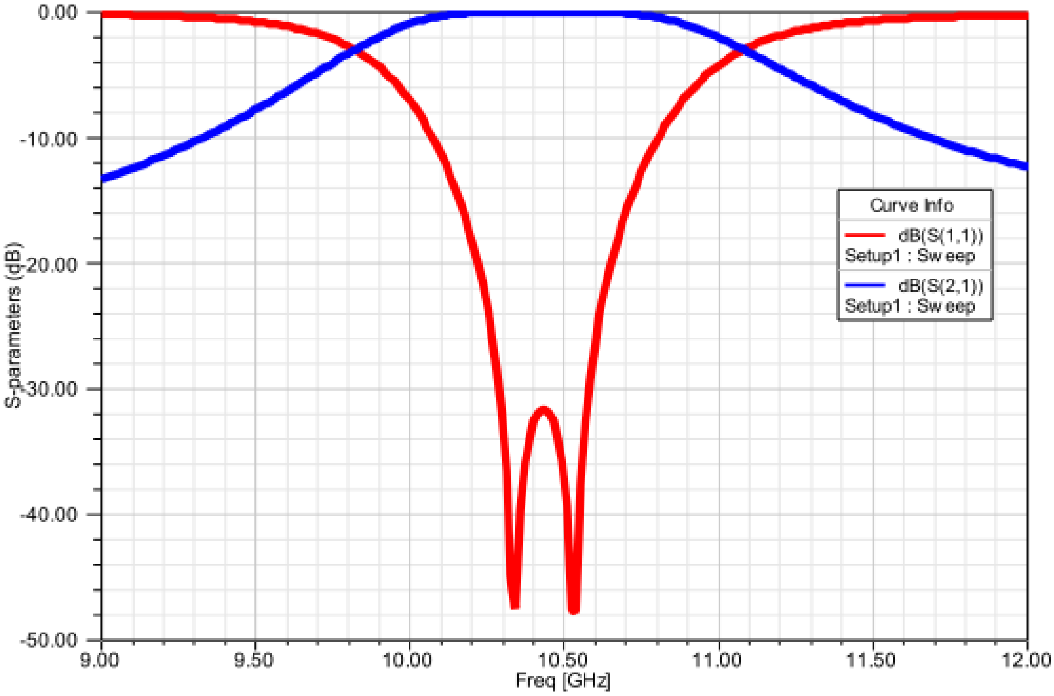

Figure 2.18: Frequency response between first resonator and second resonator .

2.6.5 Bandpass Filters

The topology of our band pass filter of order 4 is presented in Fig.(2.19), the quad resonators are coupled to gether using a rectangular waveguide, while the two end resonators are coupled to the excitation and load by means of a coaxial line with a characteristic impedance of 50 Ω. Resonators 01 and 04 are the input and output (I/O) resonators, respectively, and there is direct coupling between them.

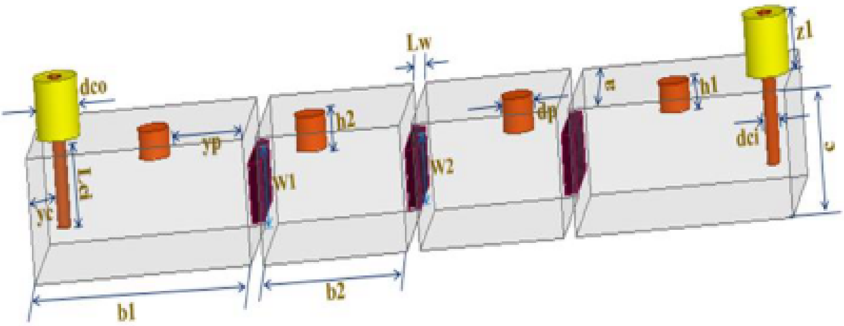

Figure 2.19: $3D$ structure of a volume filter with coupled resonators of order 4.

In murder tom validate the proposed design method, a direct-coupled fourth-order Tchebychev type bandpass filter with the same specifications as in the previous figure (with the center frequency $f_0 = 10.50\ GHz$, an bandwidth of $950\ MHz$ and return loss of $R = -20\ dB$) this frequency is synthesized using HFSS software (High Frequency Structure Simulator). The simulation is given in the figure below ([19]):

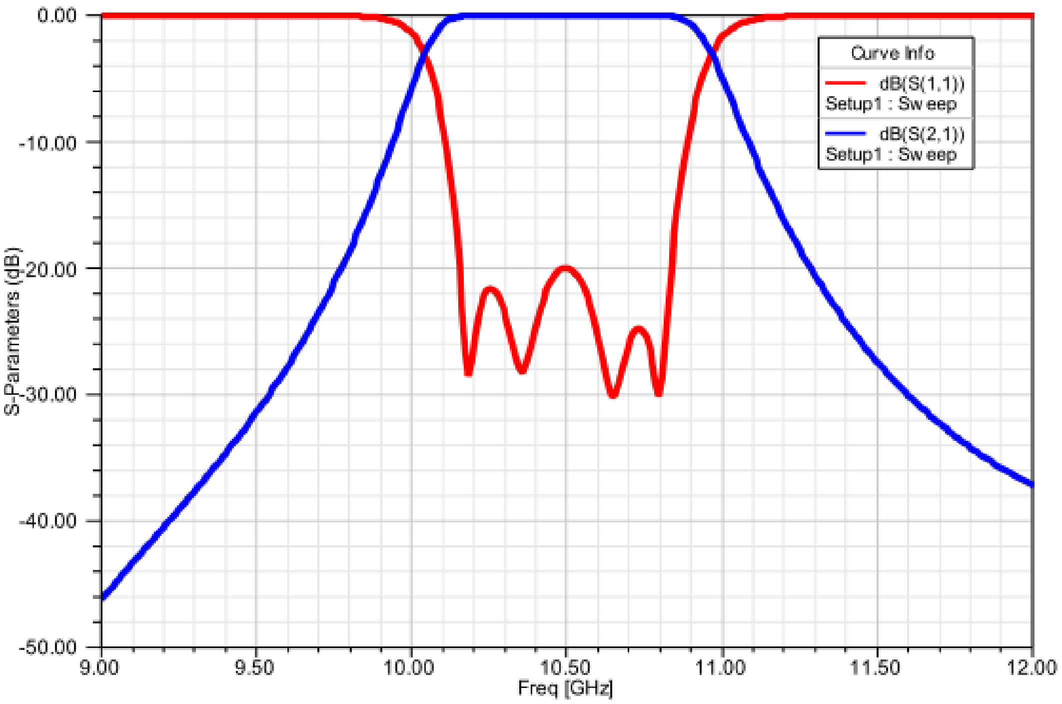

Figure 2.20: Simulation of the volume filter of four resonators.

The effect of variation in the length of the diameter of the cylinders dp and h_1 and h_2 on the frequency response of the $4th$ order filter:

The first parametric study shows the influence of the dp variation on the simulation results Fig.(2.21). When the variation dp increases (the length of the diameter of the cylinders), we see a decrease in the bandwidth, which means a shift in the bandwidth to the left. We can also see that the best result we obtained is at the value $dp = 3\ mm$ of reflection losses below $-20\ dB$ and bandwidth between 10.09 GHz and 10.97 GHz.

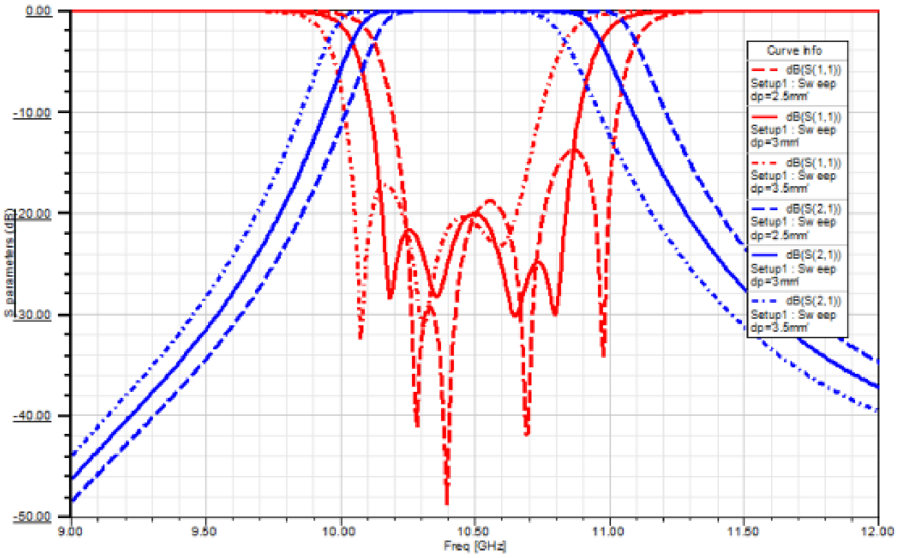

Figure 2.21: Proposed HFSS simulation results with the ”dp” variation effect.

Fig.(2.22). shows the proposed $HFSS$ simulation results with different values of the cylinder length h_1.We noticed that the bandwidth remains constant, but the reflection coefficients vary.

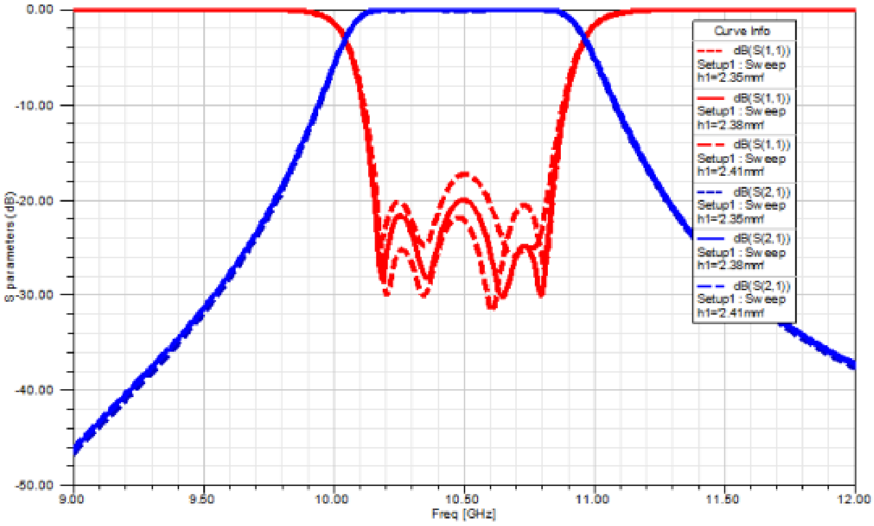

Figure 2.22: Proposed HFSS simulation results with the $''h_1''$ variation effect.

The Fig.(2.23). presents the simulation results of the frequency response as a function of different values of h_2. This parametric study highlights the impact of the variation of the length of the cylinder h_2' of the second cylinder. We observe as h_2 increases, the bandwidth shifts to the left, which results in bandwidth remaining constant.

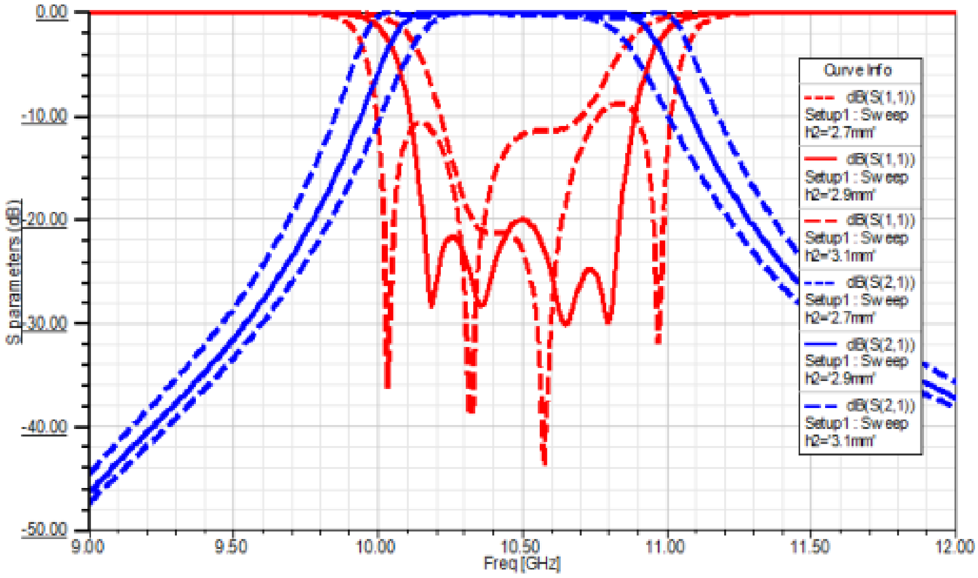

Figure 2.23: Proposed HFSS simulation results with the $''h_2''$ variation effect.

We now proceed to compare the simulation results of the $4th$ order bandpass filter. From the previous observations, we see a correspondence between the two sets of results. It is remarkable that the reflection coefficient of the filter obtained with AWR is less than $-20\ dB$, while the $HFSS$ software makes it possible to achieve a good adaptation with a reflection coefficient of then order of $-20\ dB$ over the entire range of frequency. This similarity between the results of the two soft ware confirms the consistency of the performance of the $4th$ order bandpass filter.

The electric and magnetic field distribution of the proposed bandpass filter is shown in

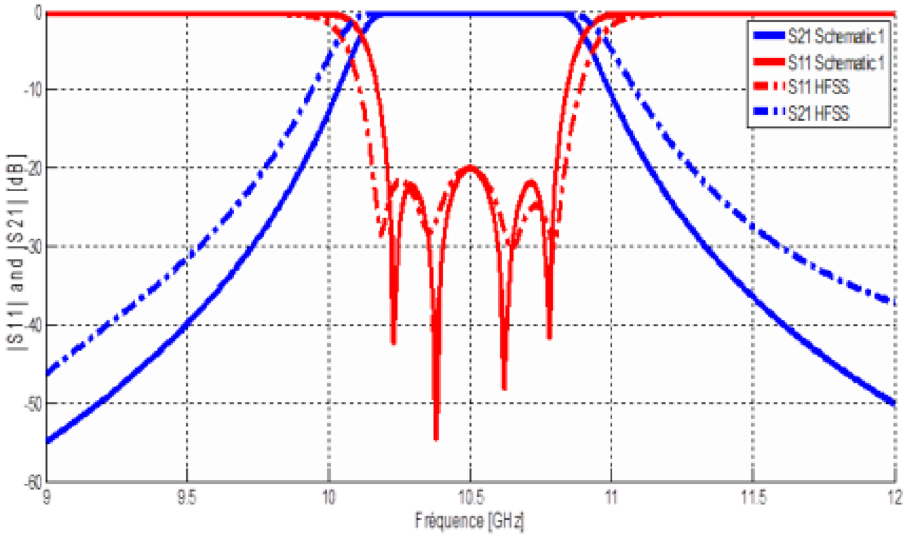

Figure 2.24: Simulation results of the Directly Coupled Bandpass Filter with HFSS software.

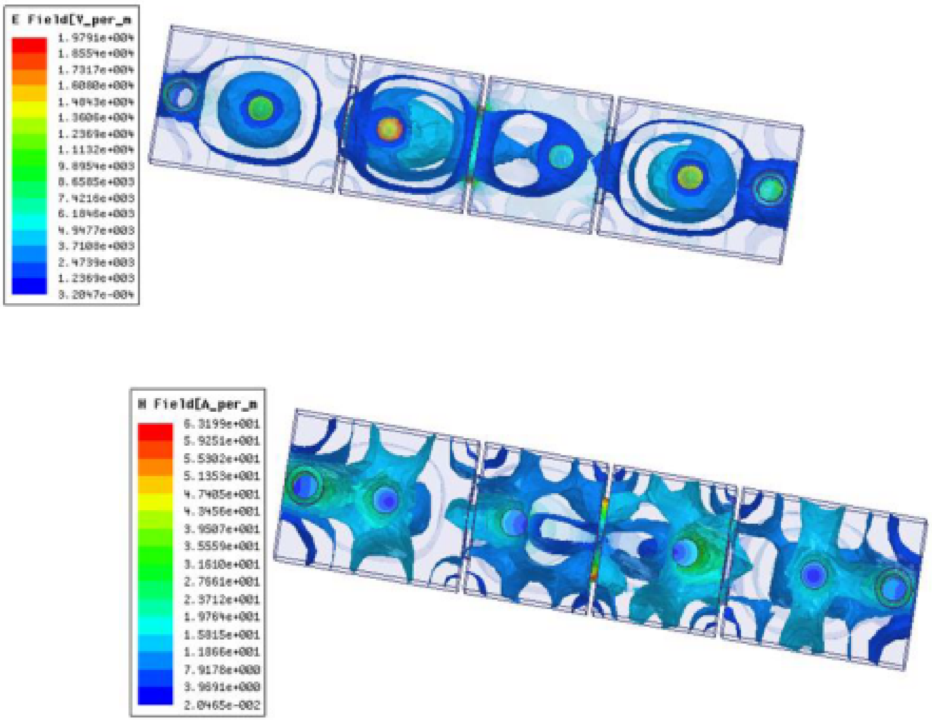

Figure 2.25: Electric field distribution and magnetic field of the 4th order bandpass filter.

2.7 Approximation and Synthesis of Online Pseudo-Elliptic Filters

The rectangular waveguide filter is one of the iris-based solid geometries with excellent size reduction. It aims to create novel structural configurations that allow a pseudo-elliptical electromagnetic response and synthesize a new class of Tchebychev filters. These designs, which employ $HFSS$ and AWR soft ware, are based on sophisticated approaches previously used to create filters with lumped components in rectangular waveguide with inductive irises. The final objective is to optimize filter selectivity using transmission zeros–which points to a pseudo-elliptical response–the analytical approach utilized to determine the filter cavity size and construct the suggested structures is detailed in depth. It proposes a pseudo-elliptical answer. This work proposes a volumetric bandpass filter for the X and Ku dual-band frequency of 11.85 GHz to 12.15 GHz, with a relative bandwidth of 2.5%. For the bandwidth, the filters show an insertion loss of 0.4/0.3 dB and a return loss of 20/23 dB. This indicates that the suggested designs operate well ([24]).

2.7.1 Equivalent Circuit and Analysis

Fig.(2.26) presents an analogous circuit for a narrowband three-pole dual-band rectangular waveguide filter. The i^{th} and j^{th} resonators are referred to by the mutual inductance, or coupling coefficient M_{ij}. At a limited frequency, the selectivity is determined by the cross-coupling m_{13}. At the input and output ports, the codes Q_{e1} and Q_{e3} identify the external quality factors [37]. An attenuation pole will be located on one side of the filter's bandpass. Asynchronous tuning of resonators is necessary to get an asymmetric filter frequency response. As a result, the resonating frequency of each resonator may vary and needs to be selected in a certain way to meet the filter requirements. [10] provides the angular resonant frequency:

$$\omega_{0i} = \frac{1}{\sqrt{L_i C_i}} = 2\pi f_{0i} \quad for \quad i = 1, 2, 3 \tag{2.7.1}$$

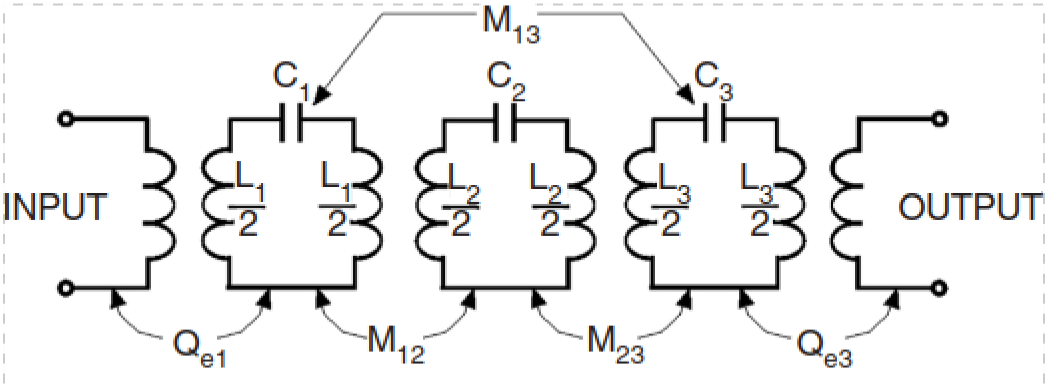

Figure 2.26: Equivalent circuit of 3^{rd} pole bandpass rectangular wave guide filter.

Where L_i and C_i are the induction and capacitance values of the equivalent circuit. To keep the filter physical configuration symetrical though the frequency response is asymetric, the following assumptions are made:

$$M_{12} = M_{23} \tag{2.7.2}$$

$$Q_{e1} = Q_{e3} \tag{2.7.3}$$

and

$$\omega_{01} = \omega_{03} \tag{2.7.4}$$

Fig.(2.27) presents the lowpass prototype of the filter transformed from the equivalent circuit Fig.(2.26). It employs J inverters with.

$$J_{12} = J_{23} = 1 \tag{2.7.5}$$

The proposed filter prototype is displayed in Fig.(2.28) Each resonator presents a frequency invariant is shown in Fig.(2.26) Each resonator represents an invariant frequency and J_{ij} are the characteristic admittance of the inverter. In order the studied case $J_{12} = J_{23} = 1$ along the main filter path, the bandpass inverter with admittance characteristic J_{13} accounts for cross coupling between adjacent resonators. g_i and B_i $(i = l,\ 2, 3)$ presents the capacitance and the frequency suspectable of the lowpass prototype, respectively. g_0 and g_4 present the resistive terminations at the input and output ports.

$$g_0 = g_4 \tag{2.7.6}$$

$$g_1 = g_3 \tag{2.7.7}$$

and

$$B_1 = B_3 \tag{2.7.8}$$

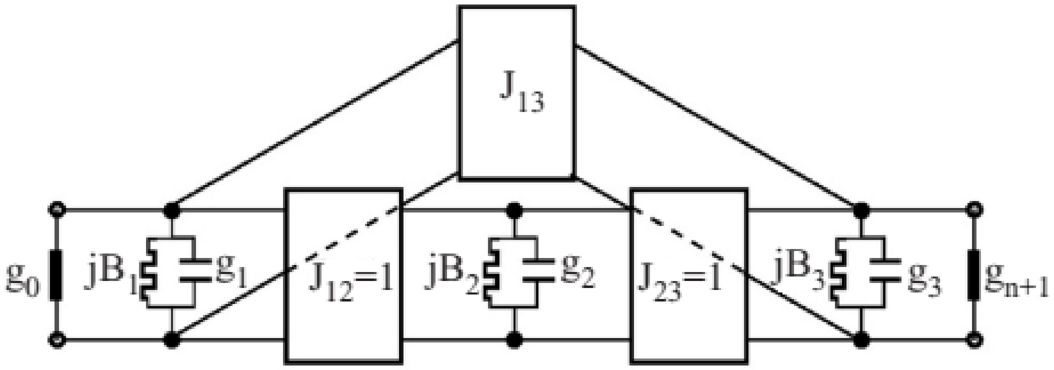

Figure 2.27: Low pass prototype of then proposed filter.

The unknown lowpass element values may be determined through a synthesis method The unknown low pass element values may be determined by a synthesis method. By using the lowpass to bandpass frequency transformation L_i and C_i can be solved as:

$$C_i = \frac{1}{\omega_0}\left(\frac{g_i}{FBW} + \frac{B_i}{2}\right) \tag{2.7.9}$$

$$L_i = \frac{1}{\omega_0}\left(\frac{g_i}{FBW} - \frac{B_i}{2}\right) \tag{2.7.10}$$

$$\omega_{0i} = \frac{1}{\sqrt{L_i C_i}} = \omega_0\sqrt{1 - \frac{B_i}{\frac{g_i}{FBW} + \frac{B_i}{2}}} \tag{2.7.11}$$

Where ω_0 is the angular frequency in centre frequency, and ω_{0i} is the angular resonance frequency of i^{th} resonator. FBW presents the fractional bandwidth of the filter. Finally, to derive the expressions for the external quality factors and coupling coefficients, susceptance slope parameter of each shunt resonator Fig.(2.26) can be defined as follows:

$$b_j = \omega_{0i} C_j = \frac{\omega_{0i}}{\omega_0}\left(\frac{g_i}{FBW} + \frac{B_i}{2}\right) \tag{2.7.12}$$

External quality factors Q_{e1} and Q_{en} and the coupling coefficient Mij can be found by:

$$Q_{e1} = \frac{b_i}{g_0} = \frac{\omega_{0i}}{g_0\omega_0}\left(\frac{g_1}{FBW} + \frac{B_1}{2}\right) \tag{2.7.13}$$

$$Q_{en} = \frac{b_n}{g_{n+1}} = \frac{\omega_{0n}}{g_{n+1}\omega_0}\left(\frac{g_n}{FBW} + \frac{B_n}{2}\right) \tag{2.7.14}$$

$$\begin{aligned} M_{ij/i\neq j} &= \frac{J_{ij}}{\sqrt{b_i b_j}} \\ &= \frac{\omega_0}{\sqrt{\omega_{0i}\omega_{0j}}} \frac{FBW.J_{ij}}{\sqrt{\left(g_i + \frac{FBW.B_i}{2}\right)\left(g_j + \frac{FBW.B_j}{2}\right)}} \end{aligned} \tag{2.7.15}$$

Where n is the filter degree or the resonator number.

2.7.2 Transmission Zeros Created By Superior Modes

For some applications it is necessary to introduce transmission zeros near the filter bandwidth to increase its selectivity. First, current methods in literature used for creating such zeros are investigated before starting implementing new techniques used for developing such a type of filters: Creating transmission zeros in microwave filters can be achieved using different methods:

Introducing couplings between non-adjacent resonators is one of the main applied methods as developed. Accordingly, Cross-coupling using the extracted poles method presents another efficient method that permits creating transmission zeros. It consists of allowing signals two itineraries through the structure in a specific way in which waves will be canceled each one by the other for a particular frequency; a transmission zero is consequently created. Such a method is commonly used for circular waveguide whose resonators operate in dual mode. Transmission zeros can be created by coupling two orthogonal modes as it is currently used in satellite communication systems by input and output multiplexers (IMUX and OMUX).

However, cross-coupling method suffers from strict limitations for the fact that the target structure requires at minimum three resonance cavities for one transmission zero that is expensive in cost and profile. In addition, machining circular waveguide is very delicate and requires high precision of the order of a micron. It is therefore very necessary to find an alternative solution to create zeros in a simple way. This can be obtained by using upper TE_{m0} propagation modes (with $m > 1$) that is brought to filter designing using rectangular waveguide. Upper modes are required to improve the filter electrical response and transmission zeros are can be easily obtained through coupling the fundamental mode TE_{10} to a specific upper mode TE_{m0} as it is already demonstrated by.

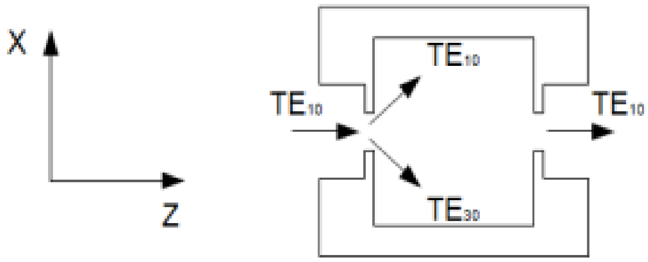

Figure 2.28: Dual-mode cavity.

Fig.(2.28) describes how a dual-mode rectangular waveguide operates consisting of the following elements: Two access guides (entrance and exit), a resonant cavities of a length equals to $\lambda g/2$ and inductive irises for coupling adjacent cavities.

The proposed filter structures employ a standard WR technology using identical waveguide for entry and exit. Upper TE_{m0} propagation modes are evanescent. Modes' length mustn't allow the fundamental mode to resonate and must be less than the wavelength half and ensure at the end almost zero amplitude for the evanescent waves to avoid superfluous reflections from the first obstacle.

To the pth resonance of the TE_{mn} propagation mode corresponds a TE_{mnp} resonant mode. When the wave TE_{m0} $(n = 0)$ is guided along a cavity of section $a > b$, its magnetic component along the z axis becomes:

$$H_Z = H_0 \cos(m\pi)e^{-j\beta z} \tag{2.7.16}$$

At the end of then resonator of length 1, H is written as follows:

$$H_Z = H_0 \cos(m\pi)e^{-j\beta l} \tag{2.7.17}$$

There is appearance of resonances for the particular frequency f_p such as:

$$\beta l = p\pi \tag{2.7.18}$$

The propagation constant in a resonant cavity is given by:

$$k_c^2 + \frac{p^2\pi^2}{I^2} = \mu_0\varepsilon_0 4\pi_{\iota}^2 f_p \tag{2.7.19}$$

Frequency are expressed using the celerity of light as:

$$\begin{aligned} f_p &= \frac{c}{2}\sqrt{\frac{m^2}{a^2}+\frac{n^2}{b^2}+\frac{p^2}{I^2}} \\ c &= \frac{1}{\sqrt{\mu_0\varepsilon_0}} \end{aligned} \tag{2.7.20}$$

- μ_0 : vacuum magnetic permittivity.
- ε_0 : vacuum magnetic permeability.
- m, n : TEmn mode indexes.
- a, b : guide sections.
- I : resonant cavity length.
- p : resonances mode rank

2.7.3 Single Mode Cavity

The section $(a \times b)$ of the guide is standard. The length of the cavity is determined by the wavelength at the resonant frequency (frequency and dimensions of the cavities are linked). The resonators are calculated on the first resonance TE_{101}. The harmonics defined for p greater than or equal to 2 constitute spurious feedback. The section of the guide is fixed by the MR standards. The length is given from the previous equation.

$$I = p\sqrt{\frac{1}{4\frac{f_0^2}{c^2}-\frac{m^2}{a^2}-\frac{n^2}{b^2}}} \tag{2.7.21}$$

By way of illustration, let's calculate the dimensions of a resonant cavity at 12 GHz. We calculate the length of the resonant cavity: $1 = 16,56$ mm.It is a half-wave (half-wavelength) cavity. We know that the irises separating each cavity have non-zero electrical lengths.

$mode\ indices\ celerity$	$MR75$	$central\ frequency$
$m = 1$	$a = 19.05$	$c = 3.108\ m/s$
$n = 0$	$b = 9.53$	$f = 12\ GHz$
$p = 1$		

Table 2.2: The dimensions of a resonant cavity.

2.7.4 Implantation of Third Pole Bandpass Filter

The first filter operates between X and Ku bands at 12 GHz. The zero transmission is here to the left of the bandwidth. This is generally more difficult to obtain than a zero located to the right of the strip. It is one degree higher than the first filter. The additional pole is provided by the addition of a single-mode resonant cavity on the TE_{101} fundamental. For dual-band rectangular waveguide filter, the HP standard at 12 GHz is determined by the name $MR75$.

The characteristics of which are as follows:

- Section of then $MR75$ guide: 19.05 $mm \times 9.53$ mm.
- Cutoff frequency: 7.88 GHz.
- Tolerance $\pm 7.6 \mu m$
- Frequency range: $10 - 15$ GHz.
- Linear attenuation between 12.7 and 32.5 $dB/100m \rightarrow\approx$ 28.5 $dB/100$ m at 12 GHz.

The specifications imposed for this first filter are as follows:

- Central frequency: 12 GHz
- Bandwidth : 300 MHz (2.5%) : $11.85 - 12.15$ GHz (Tchebychev frequency).
- Losses by Ripple in the Band : 0.044 dB.
- Return losses in the band: 20 dB.
- Order : 3
- Transmission zero: 1 to 11.75 GHz (zero to the left).

Third order

The third order is the cascading of a dual-mode cavity and a single-mode cavity. It therefore allows only one zero for three poles. $n = 3$ and $nz_{max} = 1$

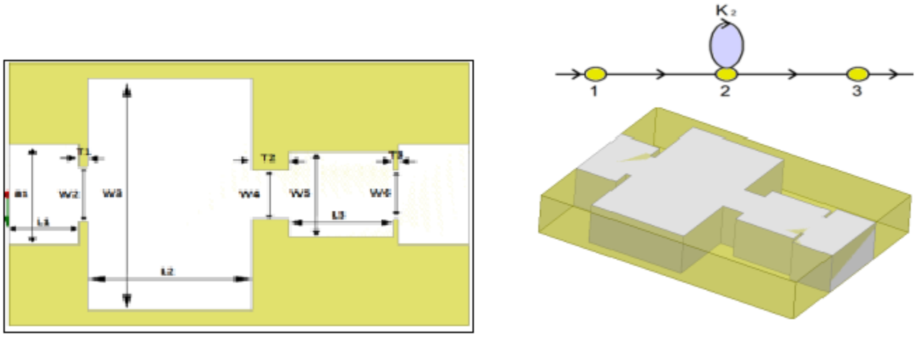

Figure 2.29: Proposed 3^{rd} pole bandpass rectangular waveguide cross coupled filter: (a) $2D$, (b) $3D$ design.

$Name$	a_1	w_2	w_3	w_4	w_5	w_6
$Value$	19.04	10.4	44.01	9.32	16.05	9.35
$Name$	L_1	L_2	L_3	T_1	T_2	T_3
$Value$	10	23.6	14.95	1.3	5.3	0.69

Table 2.3: Optimized filter dimensions.

Fig.(2.29) Ideal response of the 3 pole bandpass rectangular waveguide cross coupled filter

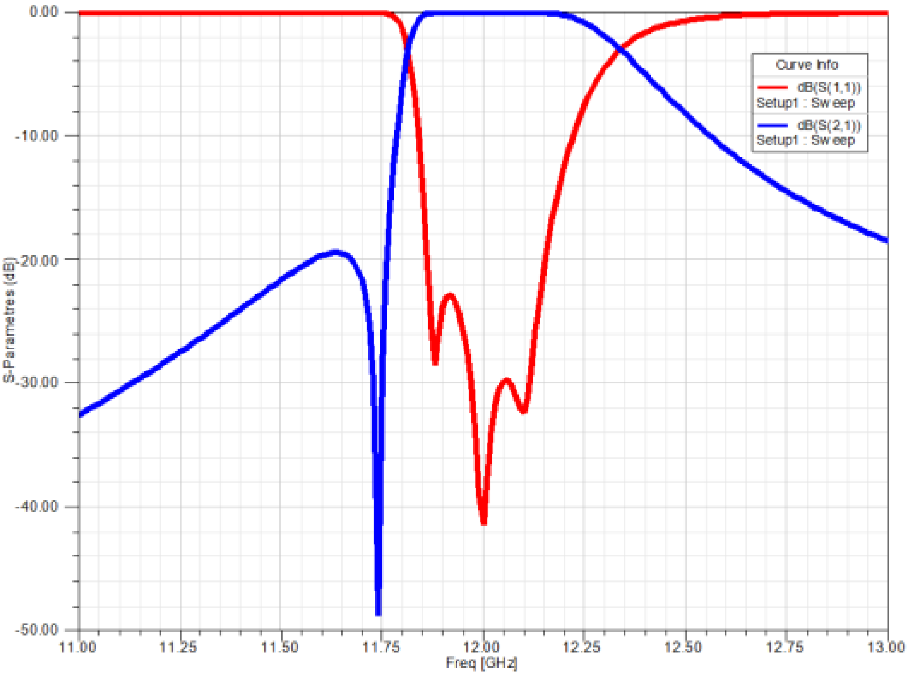

Figure 2.30: Electromagnetic response of the 3rd pole bandpass rectangular waveguide cross coupled filter.

The filter is gradually synthesized. It must start by simulating the first cavity: that is to say the first two resonators and zero. Guide calculates the dimensions of the two cavities to have zero at 11.75 GHz (dual mode cavity) and resonance at 12 GHz (single mode cavity). Zero is located as expected at 11.75 GHz and the poles are very apparent below this frequency. It is already know that it will be necessary to reduce the lengths of the cavities in order to increase the resonant frequency. On the other hand, the zero is well placed: the width of the two-mode cavity is fixed. The pole appears much lower than expected. Aft er several optimizations, the final dimensions of the filter are determined as shown in Table1.

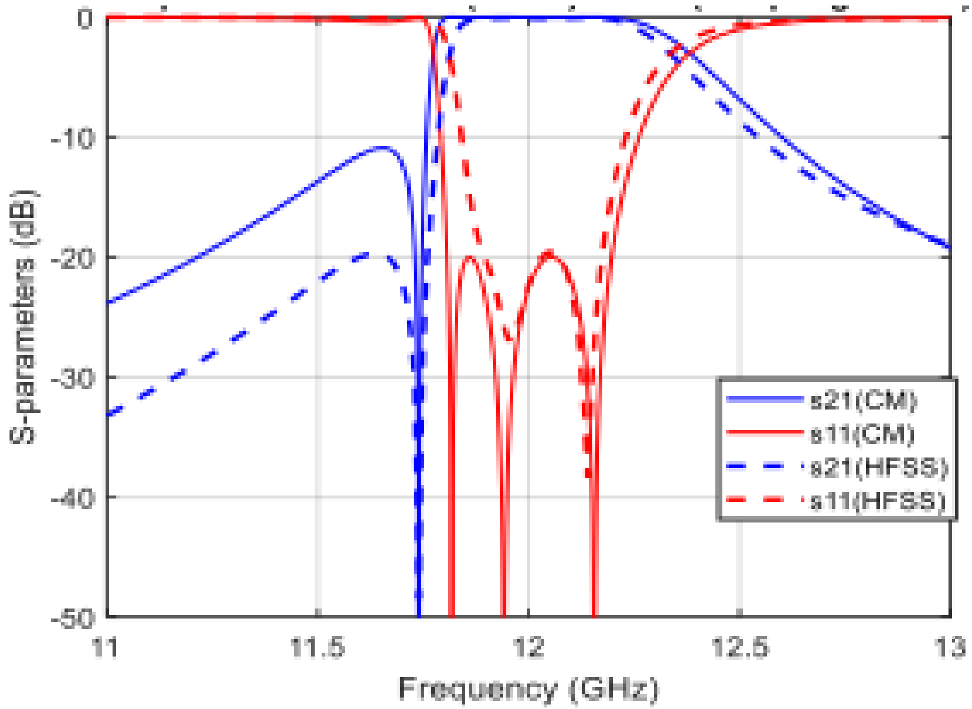

Figure 2.31: Comparison of HFSS and CM responses of then 3^{rd} pole bandpass rectangular waveguide cross coupled filter.

The electric and magnetic fields at the surface of the rectangular waveguide filter at the different operating frequency are illustrated in Fig.(2.32) and Fig.(2.33), respectively.

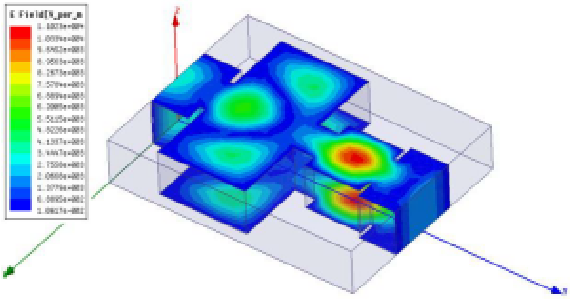

Figure 2.32: Distribution of then electric field at 12 GHz.

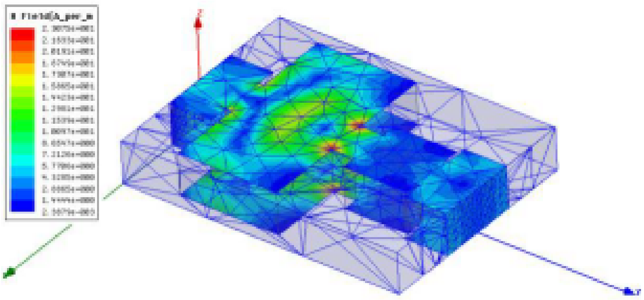

Figure 2.33: Distribution magnetic of then electric field at 12 GHz.

2.7.5 Design and Implantation of Four Pole Bandpass and Filter

The second filter operates also X and Ku bands at 12 GHz and the specifications with two zero transmission are displayed in as follows:

- Central frequency: 12 GHz.
- Bandwidth : 300 MHz (2.5%) : $11.85 - 12.15GHz$.
- Losses by Ripple in the Band : $-0.044dB$.
- Return losses in the band : 20 dB.
- Order : 4
- Transmission zero : 1 to 11.75 GHz (zero to the left).

The 4^{th} pole rectangular waveguide cross coupled filter is designed to be simulated using a copper metallization on a substrate with a relative dielectric constant of 1.

Fourth order

Two dual-mode cavities produce four poles and two transmission zeros. These can be arranged to the right or to the left of the passband or even on each side of the latter, for a symmetrical response or not. $n = 4$ and $nz_{\max} = 2$.

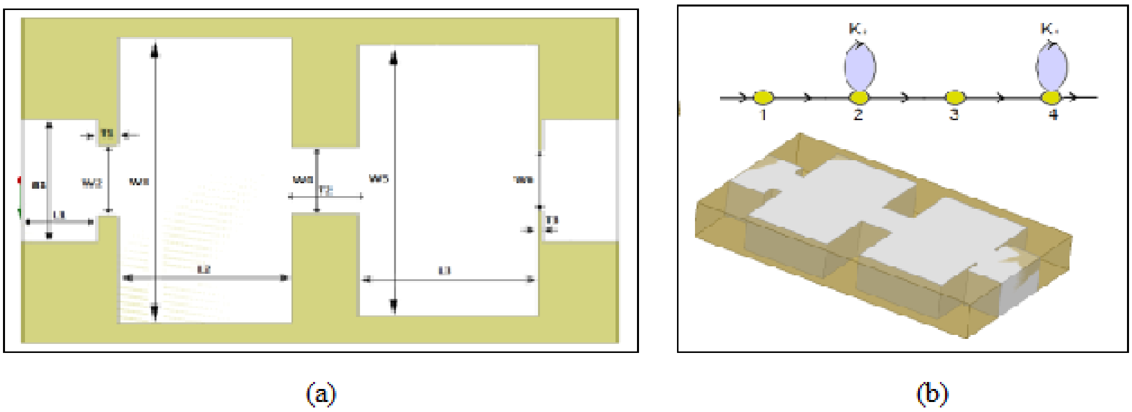

Figure 2.34: Proposed 4^{th} pole bandpass rectangular waveguide cross coupled filter: (a) $2D$, (b) $3D$ design.

$Name$	a_1	w_2	w_3	w_4	w_5	w_6
$Value$	19.05	10.84	44.1	10.2	41.96	9.3
$Name$	L_1	L_2	L_3	T_1	T_2	T_3
$Value$	10	23.09	23.96	2.8	8.92	0.7

Table 2.4: Optimization filter dimensions 4 order.

Based on the centre frequency and required fractional bandwidth, the element values of the lowpass prototype g_0, g_1, g_2, g_3, g_4 and g_5 are founded as:

$$g_1 = 0.9314, \quad g_2 = 1.2920, \quad g_3 = 1.5775 \tag{2.7.22}$$

$$g_4 = 0.7628, \quad g_5 = 1.2210, \ J_{12} = J_{34} = 1.0 \tag{2.7.23}$$

The filter coupling matrix and scaled denormalized external quality factors can be calculated using the following formulas ([26]):

$$m = \begin{bmatrix} 0 & 0.93 & 0 & 0 & 0 & 0 \\ 0.93 & 0 & 0.91 & 0 & 0.18 & 0 \\ 0 & 0.91 & 0 & 0.7 & 0 & 0 \\ 0 & 0 & 0.70 & 0 & 0.91 & 0 \\ 0 & 0.18 & 0 & 0.91 & 0 & 0.93 \\ 0 & 0 & 0 & 0 & 0.93 & 0 \end{bmatrix} \tag{2.7.24}$$

External quality factor

$$Q_{eS} = \frac{g_0 g_1}{FBW} = \frac{0.9314}{0.038} = 37.25 \tag{2.7.25}$$

Q_e	M_{12}	M_{23}	M_{34}	M_{14}	Q_s
37.25	0.0228	0.0175	0.0228	0.0046	37.25

In this section, 4-Resonator filter with tow FTZ is designed and simulated. The circuit will be synthesized in AWR as distributed element bandpass filter.

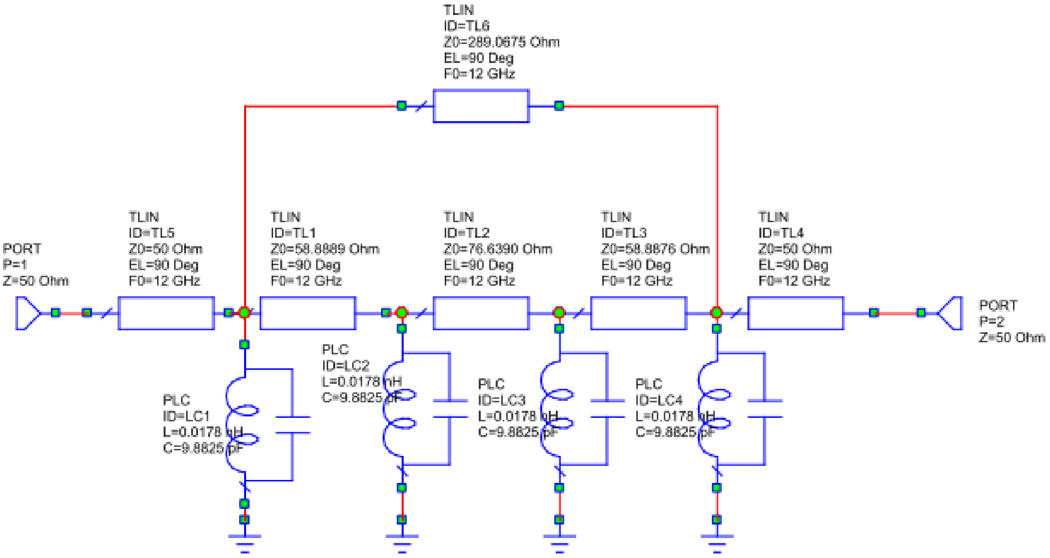

Figure 2.35: Equivalent circuit of lumped element for the proposed 4^{th} pole bandpass rectangular waveguide cross coupled filter in AWR.

As shown in Fig.(2.36) the theoretical frequency response of the filter resonates at $12GHz$. so the resultant insertion and return losses derived from AWR design is given in Fig.(2.35). Both $FTZs$ are visible in the frequency response. One FTZ is located at about 11.75 GHz and the other is located at

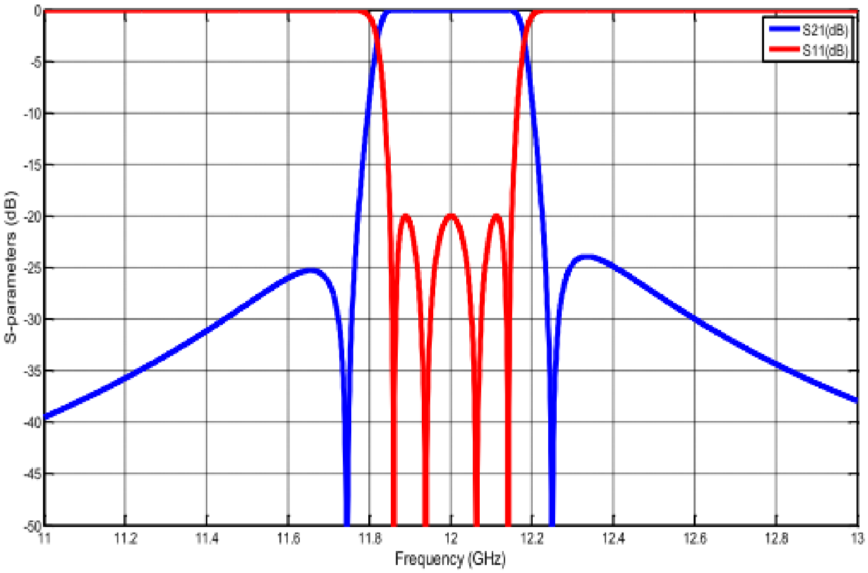

Figure 2.36: Ideal response (CM) of the proposed 4th pole bandpass rectangular waveguide cross coupled filter.

about 12.25 GHz. The filter has very good rejection for both upper and lower stop bands.

Fig.(2.37) displays simulated response when implementing the filter structure for a bandpass of more than 12 GHz from 11.85 GHz 12.15 GHz. The distances between the resonators are further tuned and the final response of the bandpass filter including the input and return losses is shown in Fig.(2.36).

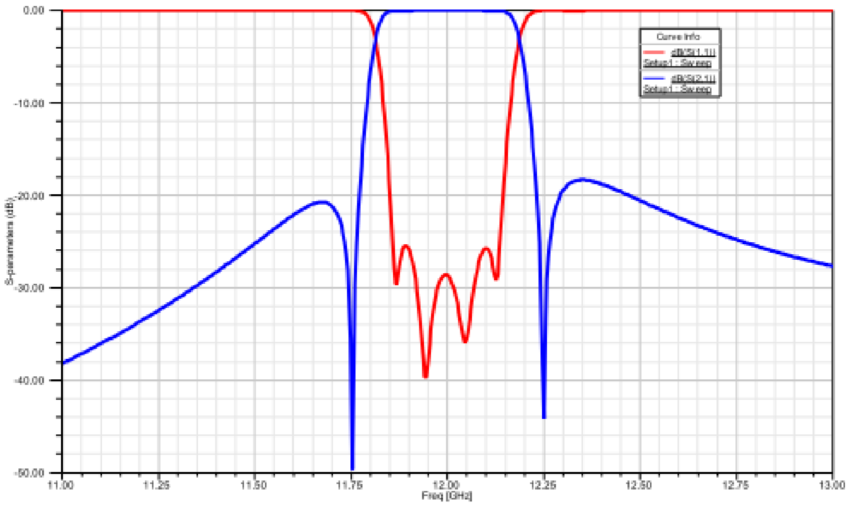

Figure 2.37: Simulated (HFSS) response of the proposed 4th pole bandpass rectangular waveguide cross coupled filter.

Fig.(2.38) shows the response of the EM model of the designed filter in comparison with the response of the distributed model.

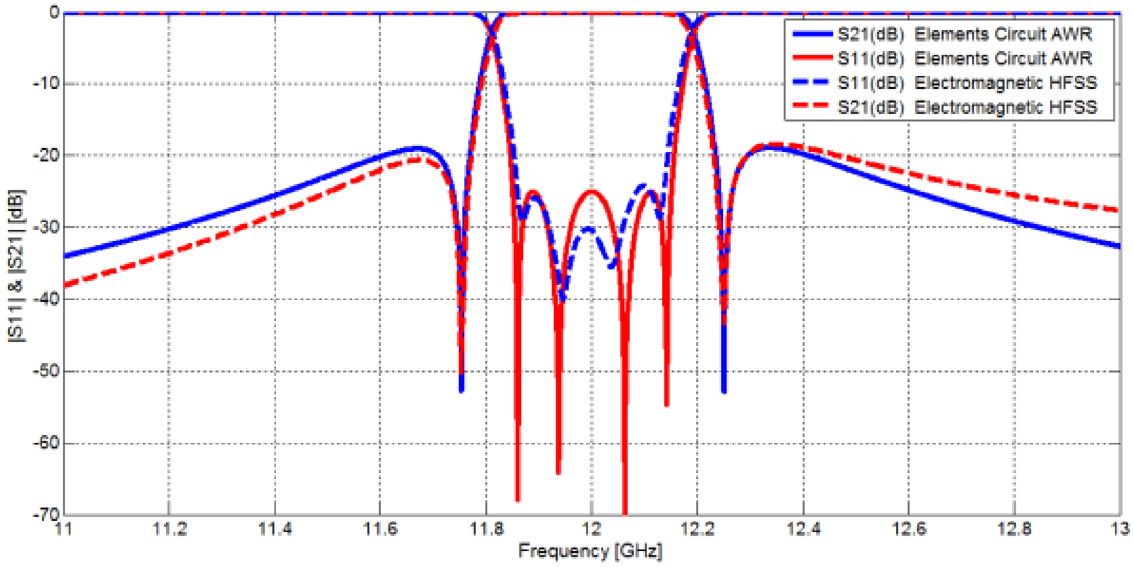

Figure 2.38: Comparison of $HFSS$ and CM responses of then proposed 4^{th} pole bandpass rectangular waveguide cross coupled filter.

Excellent agreement between ideal and simulated responses is achieved. The insertion loss is about 0.3 dB and return loss is around 23 dB for the cross-coupled waveguide filter. As expected, two transmissions zero on the right and left side of the band is observed ([18]) at 11.85 GHz and 12.15 GHz respectively with an out-of-band rejection of more than 25 dB at this point. The simulations of E-field and H-field on the structure were performed [6]. The simulation results are shown in Fig.(2.39) and Fig.(2.40), where the E-field has significant impact on the rectangular section of structure at all resonance frequency, while the H-field has very small impact.

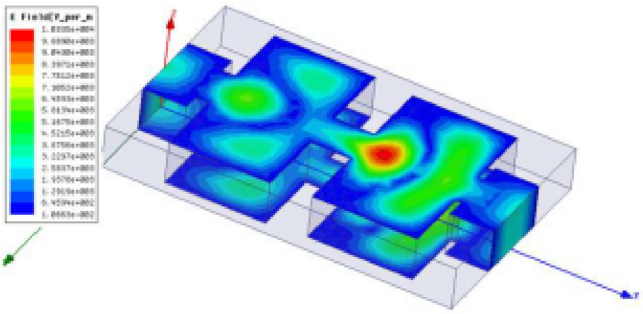

Figure 2.39: Distribution of the electric field at $12GHz$.

In the first cavity, it is clearly observed that two electric field maxima of the second harmonic TE_{102} are created. At the same time where a third electric field maxima of the TE_{301} is created in the second cavity. The coupling between the two modes is controlled by waveguide dimensions a and 1 that fixes the transmission zero position.

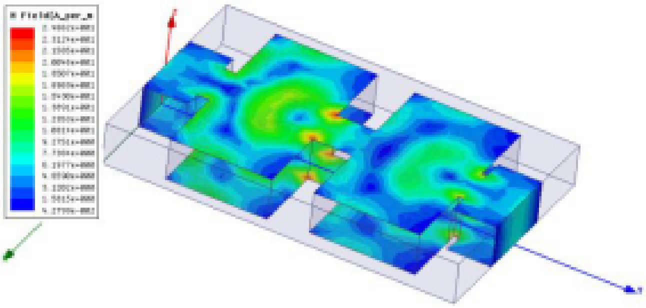

Figure 2.40: Distribution of the magnetic field at 12 GHz.

2.8 Conclusion

This chapter examines the design and synthesis of rectangular bandpass waveguide filters, focusing on propagation modes and resonator configurations. It discusses TE and TM mode parameters, focusing on the dominant TE_{10} mode. The study also examines waveguide resonators and wavelength transformation techniques. Two examples are considered for practical applications: synthesis of a direct coupling bandpass filter and approximation of online pseudo-elliptic filters. The findings contribute to microwave filter design and modern communication system applications.

Chapter 3

Development and Optimization of Compact Filters Microwave

3.1 Introduction

Microwave filters are essential components in a microwave system. Thus, much literature is available regarding the designs and implementations of microwave filters in various wireless communication systems. Combine bandpass filters are the most compact microwave filters [22]. This work presents a sizing method and a global optimization for diagnosing bandpass filters with coupled resonators. The process can extract the coupling matrix of measured or simulated admittance parameters EM from a lossy narrowband coupled resonator bandpass filter. The optimization method is used to eliminate phase shift effects of EM-simulated parameters caused by the transmission lines loaded at the ports of a filter. [22] This chapter proposes several combined bandpass filters designed and optimized using the extraction of the admittance technique. HFSS and AWR simulators create a rough electromagnetic filter model based on a Tchebychev lowpass prototype with frequency transformation. The method is based on introducing additional internal ports in the filter design to extract the multiport admittance matrix. The filter polynomial characteristics are generated from the simulated scattering parameters using the Coupling matrix. After several iterations, an exemplary filter model with optimal physical dimensions is developed, providing an ideal frequency response. The optimized filter is tuned using an admittance technique, which extracts the system quickly compared to manual experience tuning.

3.2 Coupling Matrix Theory

Following the determination of the design polynomials, an association is established between the implementation of the circuit and the approximation theory. Matrixes come into play at this juncture. The utilization of matrix operations, including inversion, similarity transformation, and partitioning, becomes feasible when the circuit is represented in matrix form, thereby augmenting its practicality. These operations streamline the processes of synthesizing, reconfiguring the topology, and simulating the performance of intricate circuits. However, it should be noted that the coupling matrix can incorporate specific practical characteristics of the filter elements. Every element within the matrix can be distinctly associated with a particular component of the final microwave device. This allows for the attributions of the electrical properties of individual elements, including the quality factor Q values associated with each resonator cavity, to be accounted for. Accomplishing this using a polynomial representation of the filter's characteristics may be challenging if attainable.

3.3 General $N \times N$ Coupling Matrix of N-Coupled Resonator Circuit

Atia and Williams [42] introduced a coupling matrix-based design method for a band-pass waveguide cavity filter in the early 1970s. They implemented the $(n \times n)$ coupling matrix, which is derived from a bandpass circuit prototype depicted in Fig.(3.1).

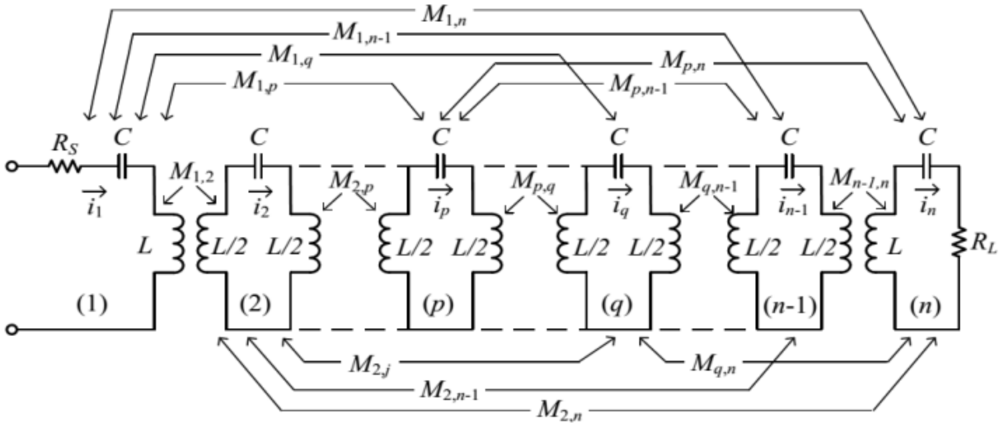

Figure 3.1: Multi coupled series-resonator bandpass prototype network.

Transistors or magnetic couplings are utilized to connect the cascaded Nth-order filter. Each resonator comprises an inductor $L = 1H$ and a capacitor $C = 1F$. Consequently, each resonator operates at a frequency of $1Hz$ and represents the source and load resistances. (It is important to note that lessens is presumed in the equivalent lumped circuit; resistance and conductance are solely present in the source and load.) reflects the current through the cycle of every resonator. The denotation for the coupling between resonators p and q is a natural number that remains constant concerning frequency. It is possible to apply the coupling matrix theory to circuits that contain asynchronously tuned resonators or the general (nn) coupling matrix. The formulation of the general (nn) coupling matrix is elaborated in [22]. For filters featuring resonators that are coupled magnetically and electrically, distinct schematics are created.

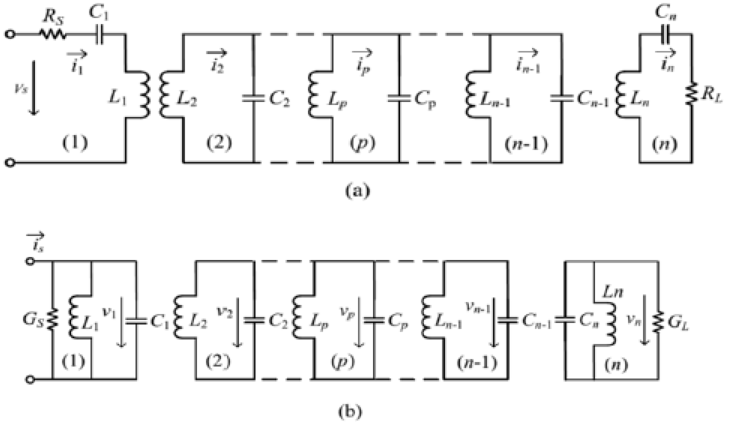

Figure 3.2: Equivalent filter circuit of n-coupled resonators for (a) loop-Equation formulation and (b) node-equation formulation [42].

The equivalent circuit featuring magnetically coupled resonators is illustrated in Fig.(3.2)(a). The coupling matrix is obtained by deriving an impedance matrix from a set of loop equations using Kirchhoff voltage law. The alternative electrically coupled circuit is illustrated in Fig.(3.2)(b). According to Kirchhoff current law, the coupling matrix is obtained using an admittance matrix formulated as a set of node equations. A comprehensive matrix [A] composed of coupling coefficients and external quality factors, irrespective of the nature of then coupling, is introduced by the researchers in [32].

$$\begin{aligned}
[A] &= [q] + p[U] - j[m] \qquad (3.3.1)\\
&= \begin{bmatrix} \frac{1}{q_{e1}} & 0 & \cdots & 0 \\ 0 & 0 & \cdots & 0 \\ \vdots & \vdots & \ddots & \vdots \\ 0 & 0 & \cdots & \frac{1}{q_{en}} \end{bmatrix} + p \begin{bmatrix} 1 & 0 & \cdots & 0 \\ 0 & 0 & \cdots & 0 \\ \vdots & \vdots & \ddots & \vdots \\ 0 & 0 & \cdots & 1 \end{bmatrix} - j \begin{bmatrix} m_{1,1} & m_{1,2} & \cdots & m_{1,n} \\ m_{2,1} & m_{2,2} & \cdots & m_{2,n} \\ \vdots & \vdots & \ddots & \vdots \\ m_{n,1} & m_{n,2} & \cdots & m_{n,n} \end{bmatrix}
\end{aligned}$$

$$p = j\frac{1}{FBW}\left(\frac{\omega}{\omega_0} - \frac{\omega_0}{\omega}\right) \qquad (3.3.2)$$

The identity matrix $[U]$, the complex lowpass frequency variable p, the center frequency of the filter $[FBW]$, and p represent the center frequency and fractional bandwidth, respectively. $(i = 1$ and $n)$ represent the resonator's scaled external quality parameters. are the normalized coupling coefficients between resonator q and p, respectively. The S-parameters can be computed utilizing the scaled external $(i = 1$ and $n)$ and matrix $[A]$, as described in reference [5]:

$$\begin{aligned}
S_{11} &= \pm\left(1 - \frac{2}{q_{e1}}[A]^{-1}_{1,1}\right) \qquad (3.3.3)\\
S_{21} &= 2\frac{1}{\sqrt{q_{e1}q_{en}}}[A]^{-1}_{n,1}
\end{aligned}$$

3.4 $N \times N$ and $N + 2$ Coupling Matrixes

The $n + 2$ coupling matrix, which is an extension of the general (nn) coupling matrix, expresses a two-port circuit. (**??**) presents a general $n + 2$ coupling matrix.

$$[m]_{(n+2)\times(n+2)} \begin{bmatrix} m_{s,s} & m_{s,1} & \dots & m_{s,n-1} & m_{s,I} & m_{s,I} \\ m_{1,s} & m_{1,1} & \dots & m_{1,n-1} & m_{1,n} & m_{1,I} \\ \vdots & \vdots & \ddots & \vdots & \vdots & \vdots \\ m_{n-1,s} & m_{n-1.1} & \cdots & m_{n-1,n-1} & m & m_{n-1,I} \\ m_{n,s} & m_{n,1} & \cdots & m_{n,n-1} & m_{n,n} & m_{n,I} \\ m_{I,s} & m_{I,1} & \cdots & m_{I,n-1} & m_{I,n} & m_{I,I} \end{bmatrix}_{(n+2)\times(n+2)} \tag{3.4.1}$$

Resonator i is self-coupling, where the subscripts (s) and (l) denote the source and load, respectively. Asynchronous tuning is achieved when a subset of the filter's entries take on non-zero values. The $n+2\times n$ coupling matrix comprises supplementary columns and rows to accommodate the source and load, respectively, in contrast to the general (n) coupling matrix. In addition to establishing the coupling between the load and resonator, they also establish the self-coupling between the source and the load. The following are the benefits of the $n+2$ coupling matrix due to the additional columns and rows ([45]):

A single resonator may be coupled to multiple ports, whereas one port may be connected with various resonators. Coupling is a feasible process between the burden and the source. Thus, the $(n\times n)$ coupling matrix lacks generality compared to the $n+2$ coupling matrix.

3.5 Physical realization of coupling matrix

Once the normalized coupling matrix $[m]$ for a coupled resonator topology has been determined, the prototype-normalization of the matrix $[m]$ at the desired bandwidth can be used to derive the actual coupling matrix [M] of a coupled-resonator device with the given specification ([35]): Calculated by prototype de-normalization of the matrix $[m]$ at a desired bandwidth, as follows ([35]):

$$Q_{eS}=\frac{g_0g_1}{FBW}; \qquad Q_{eL}=\frac{g_ng_{n+1}}{FBW} \tag{3.5.1}$$

$$M_{i,i+1}=\frac{FBW}{\sqrt{g_ig_{i+1}}}; \qquad i=1 \;\; to \;\; n-1 \tag{3.5.2}$$

$$m_{i,i+1}=\frac{M_{i,i+1}}{FBW}; \qquad i=1,\dots n \tag{3.5.3}$$

3.6 Band pass filter based on an electronic circuit

The process of developing bandpass filters through electronic circuit design consists of the subsequent stages:

- Specifications include the cutoff frequency, center frequency, filter type, filter order n, filter ripple level, filter bandwidth BW, and fractional bandwidth FBW.
- The process of ascertaining the values of the elements.
- The computation of the external quality factors (Q_{ext} and Q), which are associated with the elements gi and the coupling elements $M_{(i,i+1)}$.
- The combined element $R_0L_0C_0$ of resonators is computed.
- Utilising lumped elements to compute impedances in a series of equivalent circuits.

3.7 Design Specifications and Initial Microstrip Filter

Table 3.1 shows the specifications imposed for this filter. The circuit to be synthesized is defined in environment as a distributed element bandpass filter.

Function	**Tchebychev**
$Order$	$N = 4$
$Center\ Frequency$	$1.2\ GHz$
$Lar\ (passband\ ripple)$	$0.04321\ dB$
$Bandwith\ at - 3dB$	$BW = 154.1\ MHz$
$return\ loss : RL$	$< -20\ dB$
TFZ	$fzt1 = 1.08\ GHz$ et $fzt2 = 1.37\ GHz$

Table 3.1: The specifications of the filter.

3.7.1 Frequency response of the ideal bandpass filter

Once the order filter is determined, knowing the maximum ripple of 0.04321 dB and the specifications defined in the specifications, we obtain the coefficients g_i $(i = 1, ..., 4)$ of the bandpass prototype of the type filter Tchebychev:

g_0	g_1	g_2	g_3	g_4	g_5
1	0.9314	1.2920	1.5775	0.7628	1.2210

Using the specifications defined in the specifications, to calculate the relative bandwidth, quality factor and coupling coefficients, respectively:

$$\omega_0 = 2\pi f_0 = 7.5398\ rad/s \quad with \quad FBW = \frac{BW}{f_0} = 0.1284 = 12.84\% \tag{3.7.1}$$

$$Q_e = \frac{g_0 g_1}{FBW} = \frac{1 \times 0.9314}{0.128416} = 7.2538 \tag{3.7.2}$$

Coupling coefficients

M_{12}	M_{23}	M_{34}	M_{14}
0.1099	0.1229	0.1099	-0.0282

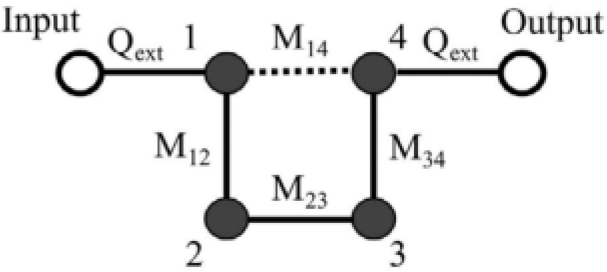

Figure 3.3: Coupling diagram of Four-pole cross-coupled microstrip resonator filter.

Design the four-pole microst cross-coupled filter based on the prescribed general coupling matrix:

$$[m] = \left\{ \begin{array}{llll} 0 & 0.8559 & 0 & -0.2196 \\ 0.8559 & 0 & 0.9571 & 0 \\ 0 & 0.9571 & 0 & 0.8559 \\ -02196 & 0 & 08559 & 0 \end{array} \right\} \tag{3.7.3}$$

3.7.2 Equivalent Circuit of the Filter

The filter specifications translate into the desired coupling matrix elements $M_{(i,i+1)}, Q_{en}$, and Q_{ext}. Fig.(3.4) shows the circuit diagram for this filter, where the lumped elements $R_0L_0C_0$ represent the four synchronously tuned resonators and the quarter-wave transmission lines. These transmission lines have an electrical length $EL = \pm 90^0$ at the central frequency f_0. The corresponding design parameters for the bandpass filter are: Lumped elements $R_0L_0C_0$ of resonators:

$$L_0 = \frac{Z}{\omega_0 Q_e} \times 10^9 \ nH = 0.88731 \ nH \tag{3.7.4}$$

$$C_0 = \frac{Z}{\omega_0 Q_e} \times 10^{12} \ pF = 19.824 \ pF \tag{3.7.5}$$

$$R_0 = 100000 \ \ \Omega \tag{3.7.6}$$

The impedances of the resonators:

$$Z_{i,i+1} = \frac{Z}{Q_e M_{i,i+1}} \tag{3.7.7}$$

When $Z_0 = 50 \ \Omega$ is the supply impedance at the I/O ports:

$$Z_{12} = 60.86\Omega, \tag{3.7.8}$$

$$Z_{23} = 54.45\Omega, \tag{3.7.9}$$

$$Z_{34} = 60.86\Omega, \tag{3.7.10}$$

$$Z_{14} = -237.1579\Omega \tag{3.7.11}$$

The band-pass filter prototype operates using the characteristic impedance of the positive quarter-wave resonator lines and a parallel $R_0L_0C_0$ resonant circuit. The filter's equivalent circuit is shown in Fig.(3.4) after calculating the elements of the series and parallel branches.

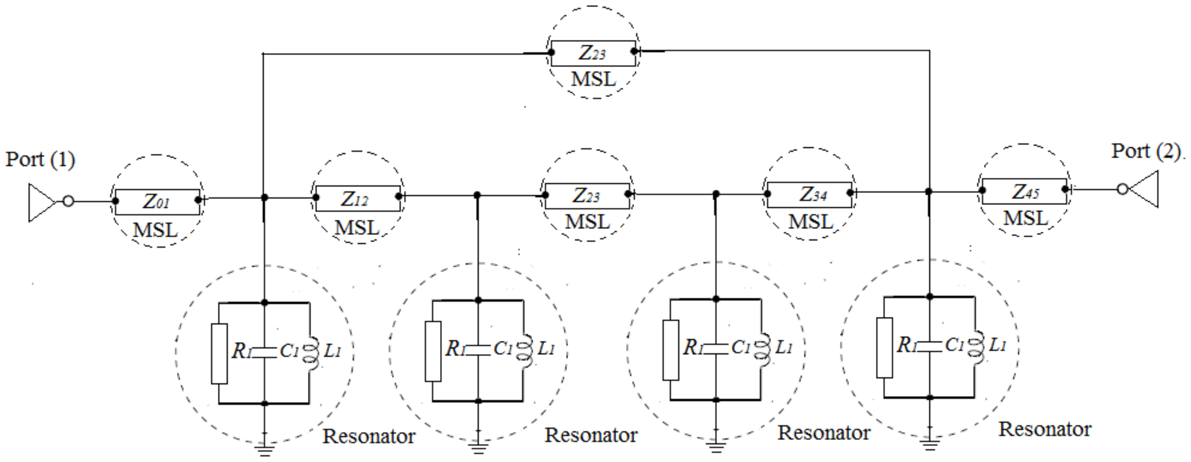

Figure 3.4: Band pass filter with lumped elements of order 4 with circuit resonant $R_0L_0C_0$ parallel.

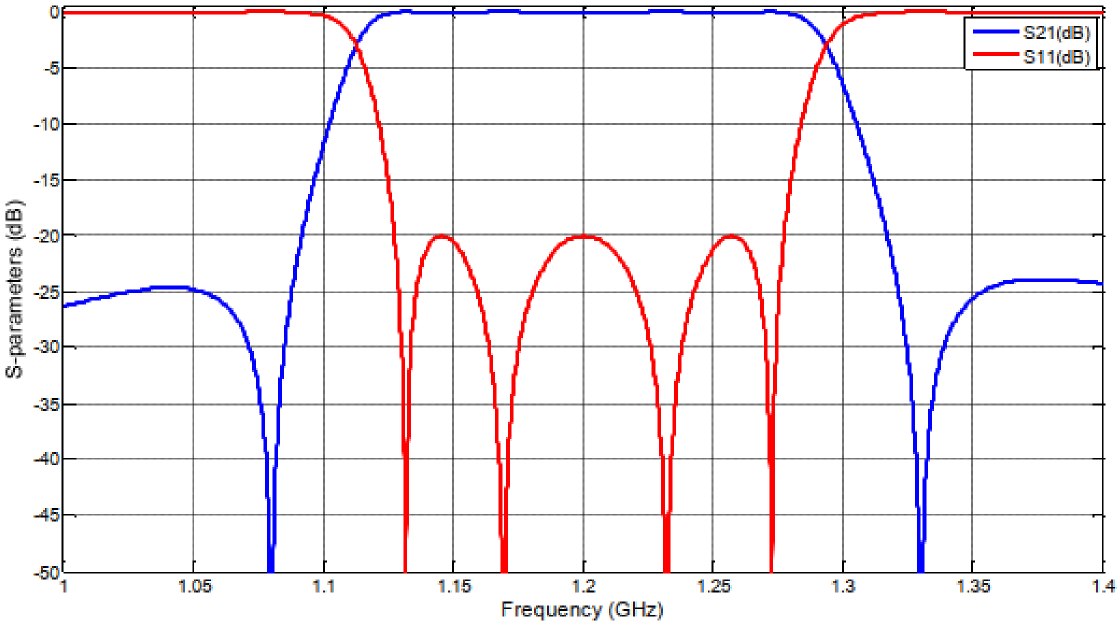

Figure 3.5: Ideal response for the 4th order bandpass filter.

As determined by AWR, Fig.(3.5) illustrates the ideal reflection and transmission response of the equivalent circuit in lumped elements. Our bandpass filter's frequency response indicates that its center occurs at 1.20 GHz. At 154.1 MHz, there are reflection losses of $-20\ dB$; this is a narrow frequency band.

3.7.3 EM design of the band pass filter in planar technology

3.7.3.1 Cross-coupled filter

Fig.(3.6) illustrates the schematic representation of our order 4 bandpass filter. This filter operates within the frequency range of L and comprises four folded quarter-wave resonators, each with its own folded wavelength [19]. Consequently, the dielectric substrate has a thickness denoted as h, and the filter topology is compact.

One end of the filter is short-circuited (via-hole grounding), while the other is open-circuited. The input and output (I/O) resonators, numbered 1 and 4, are inter-coupled, with cross- coupling occurring between them. The simulation is performed on a "$RO4003$" substrate with the following properties: a thickness of 0.813 mm, a dielectric loss tangent of 0.0027, and a relative permittivity of $\epsilon_r = 3.55$.

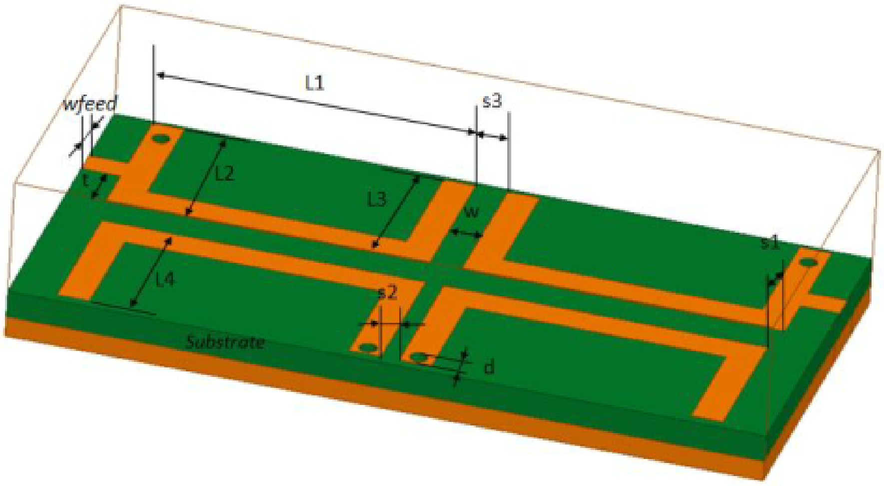

Figure 3.6: $3D$ Structure. Four-pole cross-coupled microscopic resonator filter.

3.7.3.2 The filter dimensions

In the context of full-wave electromagnetic (EM) simulations for the design of a microstrip filter, it is more efficient computationally to decompose the filter into distinct components and have each component simulated by the EM simulator to derive the desired design parameters by a general coupling matrix. They are

$Parameters$	x_1	y_1	H	H_s	L_1	L_2	L_3
$Values$	25	52	0.017	0.813	10.9	11	22
$Parameters$	L_4	s_1	s_2	s_3	T	W_{feed}	W
$Values$	10.5	0.9	0.25	1.13	2.3	2	2

Table 3.2: Dimensions of the band pass filter.

subsequently combined to produce the global filter's response. Demonstrating the efficacy of This CAD methodology for developing narrowband filters is a four-pole cross-coupled filter, as illustrated in Fig.(3.6).

3.7.3.3 Quality factor extraction

The external quality factor of the I/O resonator is determined in Fig.(3.7). In the simulation, the resonator is presumed to operate without any loss. $A\ 50 - ohm$ line is connected to port 1 at a specific location denoted as t. To obtain the external quality factor Q_{en}, port 2 is coupled weakly to the resonator to determine the bandwidth of the response magnitude $S21$, which is- 3 dB.

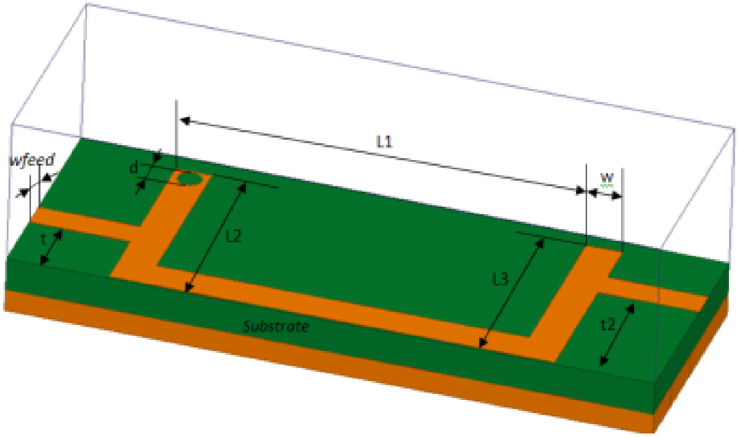

Figure 3.7: Implementation for extraction of the external quality factor.

3.7.3.4 Extraction of Q_{en} from a volume resonator by group delay

The quality factor was established by analyzing the reflection coefficient group delay S_{11}. The result of the group delay outcome is shown in Fig. (3.8).

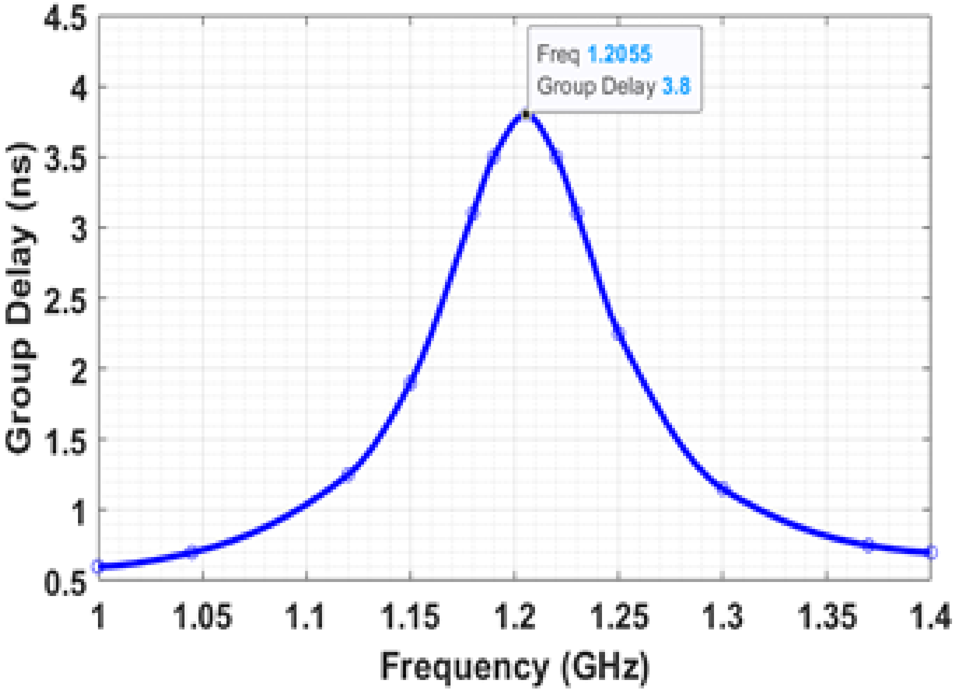

Figure 3.8: Group delay of a volume resonator for quality factor sizing .

The group delay values and quality coefficients at the resonant frequency have been meticulously derived from the data presented in Fig.(3.9), resulting in the following estimations:

$$\tau_{s_{11}} = \frac{\omega_0 \tau_{s_{11}}(\omega_0)}{4} = \frac{2 \times \pi \times 3.8 \times 1.2055}{4} = 7.1920 \tag{3.7.12}$$

The table below presents the values of several iterations to calculate the quality factor by varying the port location indicated by Table (3.3):

T	$f_0(GHz)$	τ	Q_e
0.2	0.9609	1.9	2.8678
0.4	1.0672	2.72	4.5597
0.6	1.0852	2.78	4.7389
0.8	1.1273	2.83	5.0112
1	1.119	4.15	7.2965

Table 3.3: Dimensions and Parameters Extraction.

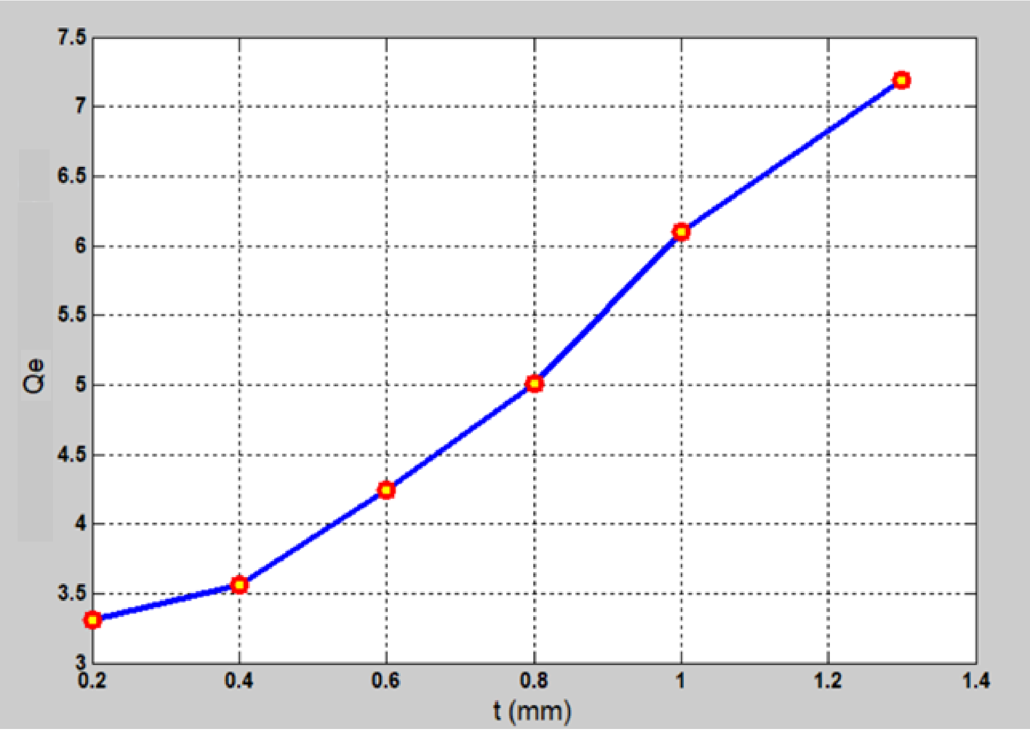

Figure 3.9: Design of then curve of Q_{en} against t.

Fig.(3.9) illustrates the findings presented in Table 3.3 The design of the Q-versus-t curve can be deduced, as illustrated in Fig.(3.10). In this instance, as t increases, the branch line is redirected towards the resonator short-circuit (via-hole grounding); consequently, the source's coupling becomes weakened, resulting in an increase in Q_{en}.

3.7.3.5 Coupling coefficient extraction

The interaction between two resonators is contingent upon the distance that separates them. Proximity between two resonators leads to disruption in their resonances due to the coupling that links them. The HFSS simulator can determine the resonant frequency of both even and odd modes. The coefficient for inter-resonator coupling, denoted as (k), can be calculated using the following formula:

$$K = \frac{f_2^2 - f_1^2}{f_2^2 + f_1^2} \tag{3.7.13}$$

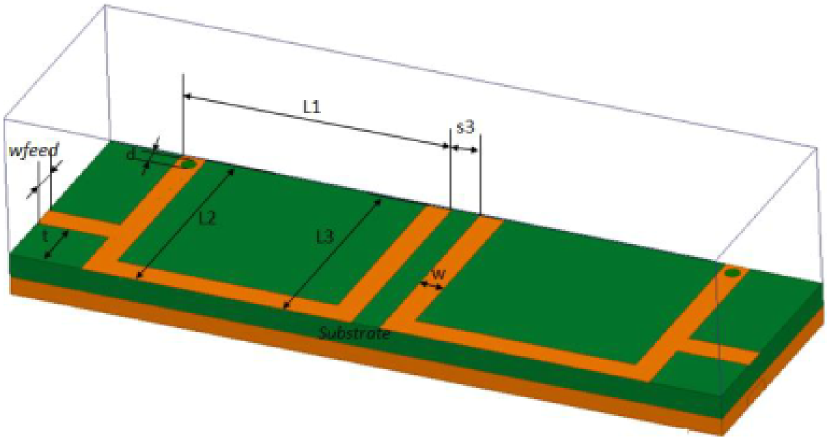

Figure 3.10: Arrangement for extracting coupling coefficient M_{14} .

An electromagnetic simulation layout of the figure is employed to derive the cross-coupling between resonators 1 and 4 from the filter configuration depicted in Fig.(3.10). The coupling between them, in this instance, is governed by the electric field and is therefore referred to as electric coupling. To attain a pair of transmission zeros at finite frequency, M_{14} and M_{23} must have opposite signatures. Consequently, this implementation of cross-coupling is essential. As illustrated in simulated Fig.(3.11), the structure's frequency response comprises two resonance peaks utilized to assess the coupling coefficient between the initial and fourth resonators.

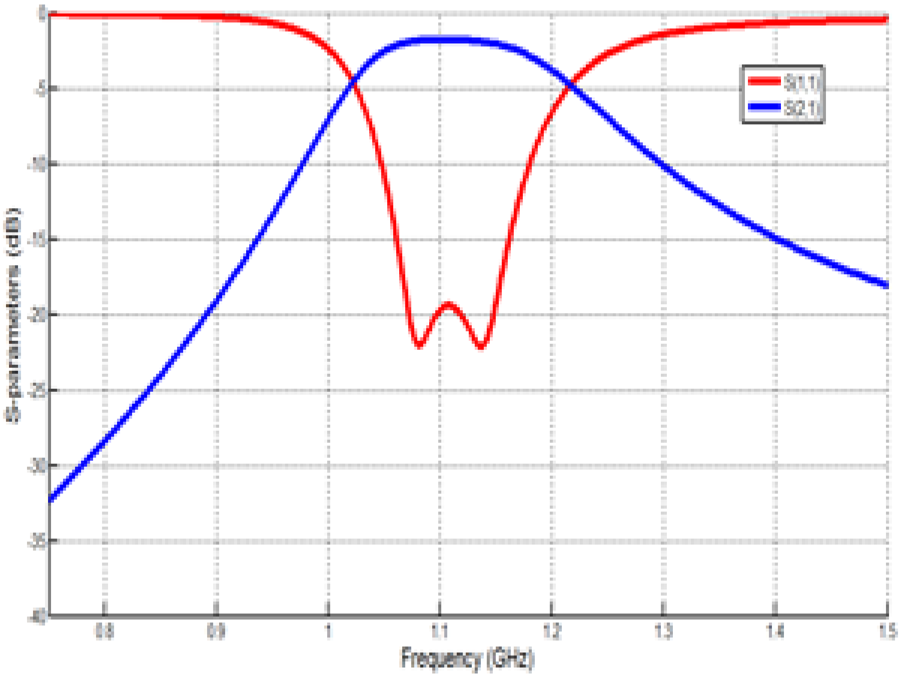

Figure 3.11: Response Electromagnetic of the 2nd order bandpass filter .

3.7.3.6 Effect of the spacing Soon, the frequency response of the filter

The first parametric study shows the influence of the S_1 spacing on the simulation results. When the space S_1 increases (space between the first and second resonators), we can see that the bandwidth decreases, which implies a narrower bandwidth. We can also see that the best result we obtained is $S_1 = 0.9\ mm$ of reflection losses below $-25\ dB$ and band width between $1.13\ GHz$ and $1.28\ GHz$. The variation of the coefficients of the filter matrix $[S]$ as a function of frequency for these different values is shown in the graphs of Fig.(3.12).

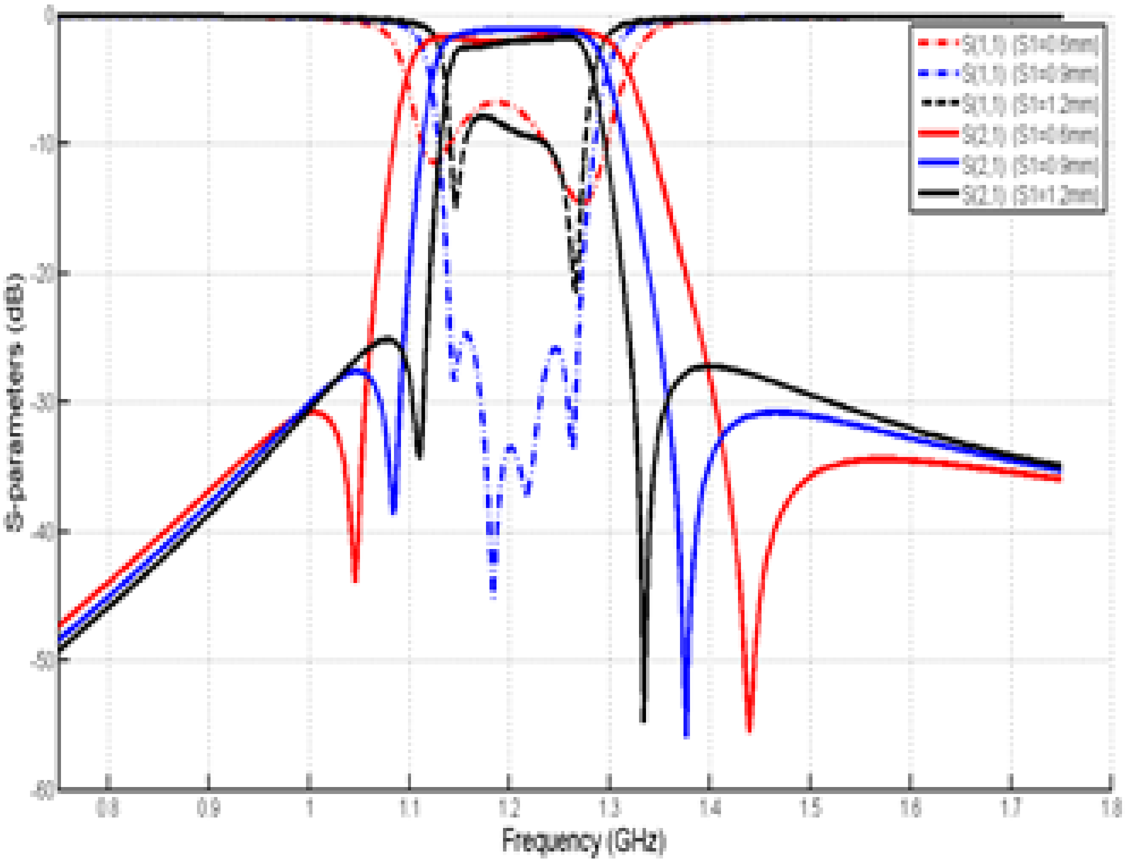

Figure 3.12: Frequency response of then CCM filter against the design goals after optimization.

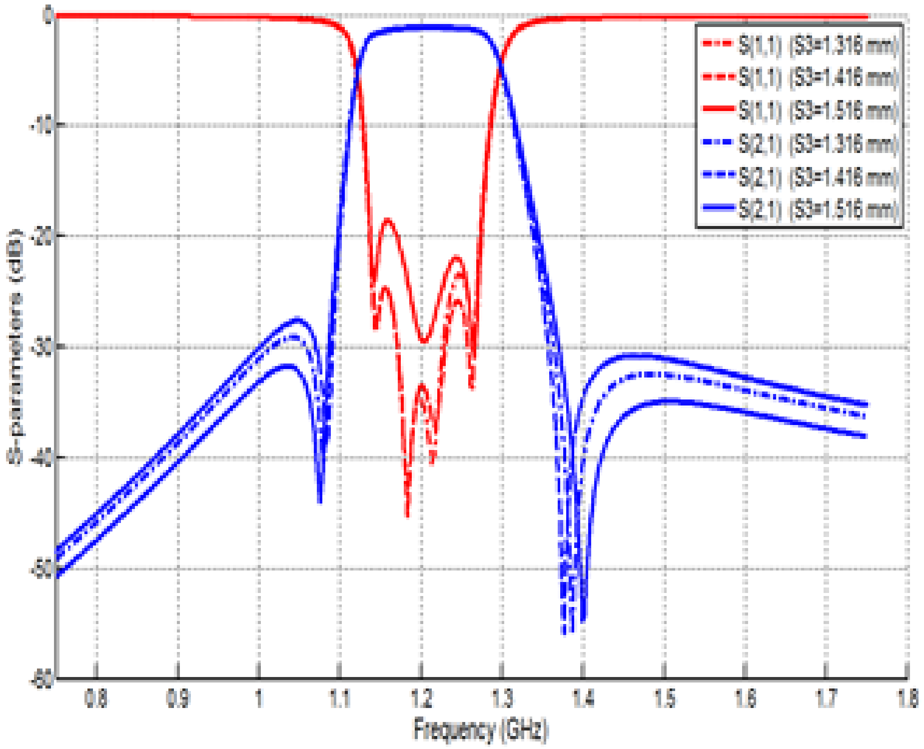

Figure 3.13: HFSS simulation results proposed with different values of S_3.

Fig.(3.13) illustrates the simulation results in S_{11} and S_{21} proposed with different S_3 values. This parametric study shows the influence of the S_3' spacing between the first and fourth resonators. As the S_3' gap increases, the upper cutoff frequency and the band gap point are shift ed slightly downwards, which means a narrower bandwidth.

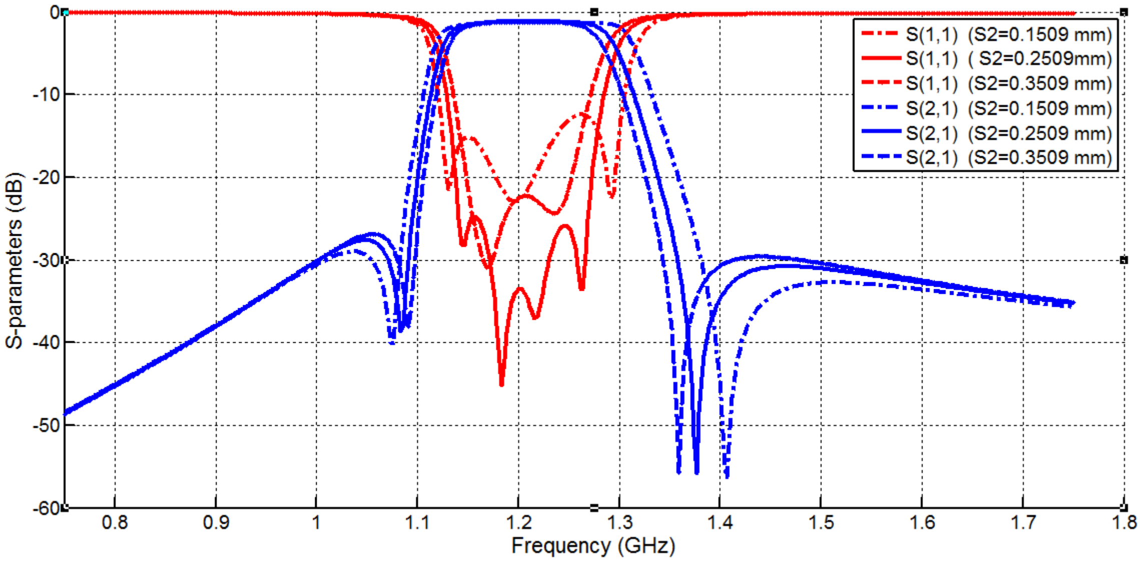

Figure 3.14: HFSS simulation results proposed with different values of S_2..

Fig.(3.14) shows the results of the HFSS simulation proposed with different values of S_2. This second parametric study shows the spacing "S_2" influence between the second and third resonators. When "S_2" increases, the lower cutoff frequency stays the same, and the upper cutoff frequency moves lower. Therefore, S_2 is the second parameter affecting the **HFSS** result: when S_2 increases, the bandwidth is reduced.

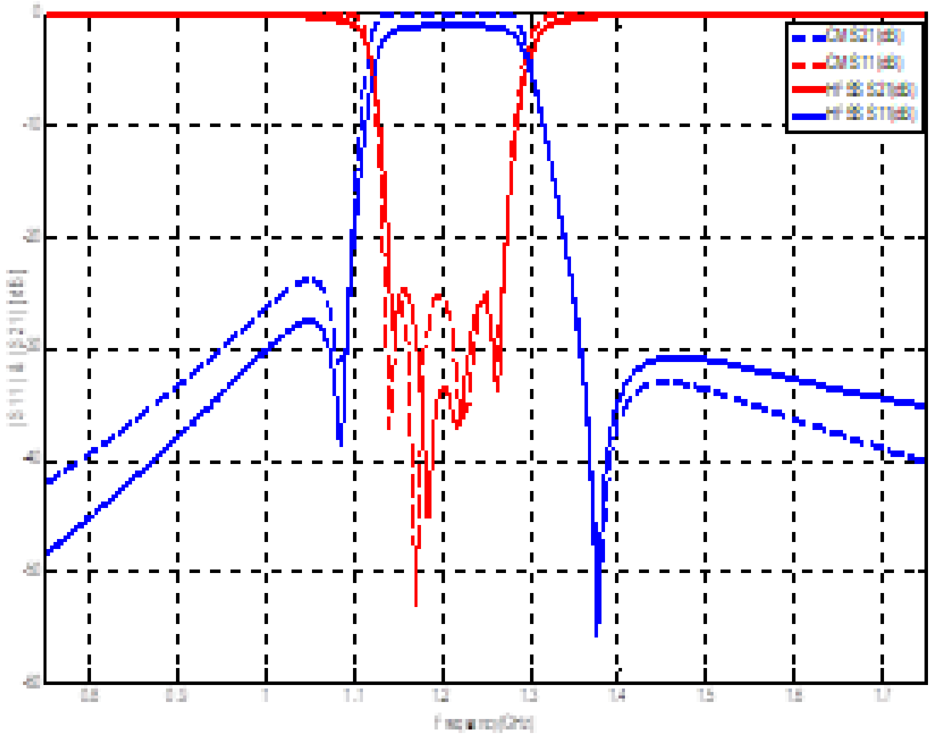

Figure 3.15: Final response of the cross-coupled bandpass four-pole filter after optimization compared with the ideal response.

In Fig.(3.15), it is observed that the proposed filter has attained a filtered bandwidth ranging from 1.13 GHz to 1.28 GHz, centered at 1.2 GHz. Within the passband, the insertion loss measures approximately -1.1 dB, while the return loss registers below -24.7 dB, achieving a value of -44.9 dB at the frequency of 1.18 GHz.

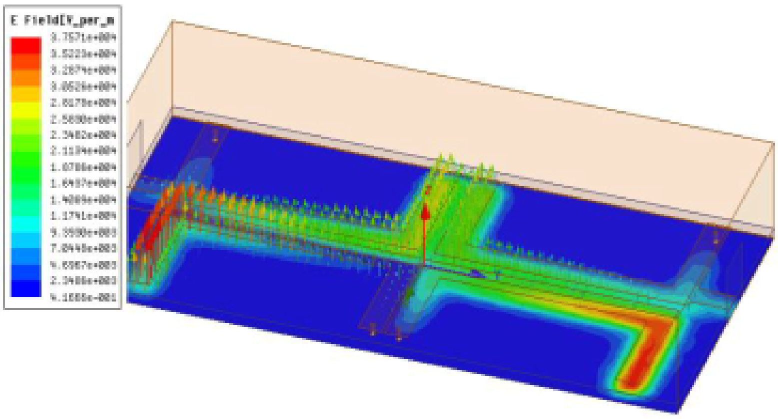

Figure 3.16: Distribution of then electric field at 1.2 GHz.

Exceptional rejection levels are achieved beyond the filtered band region, with attenuation measuring below $-39.3dB$ at the 1.08 GHz frequency and hitting a peak rejection of $-55.8dB$ at 1.37 GHz. The designed filter, featuring two finite transmission zeros, demonstrates the anticipated frequency response. Fig.(3.15) compares the simulated response of the proposed four-pole microscopic bandpass filter and the ideal coupling matrix response, showcasing a remarkable alignment between the two. Additionally, Fig.(3.16) displays the electric field distribution of the proposed bandpass filter. Table 3.4 presents a performance comparison between the proposed work and recently published works. The table indicates that the microscopic filter under consideration possesses favorable parameters, including minimal insertion loss and substantial isolation between two channels at the operational frequency. This characteristic is critical in contemporary communication systems. As a result, the overall performance of the proposed circuit is comparatively superior to that of the alternative filters.

$Refs$	$order$	$Center\ frenquency$ $in\ GHz$	$Bandwith$ in MHz	$Retun$ $loss\ dB$
[31]	04	1.26	75.6	18 dB
$Work\ in\ HFSS$	04	1.20	153.9	24.7 dB
$Work\ in\ AWR$	04	1.20	154.1	25 dB

Table 3.4: Comparison of characteristics between the Microscopic filter and the recently introduced Microscopic filters.

3.7.4 Fabrication and Experimental Results

A cross-coupled filter has been fabricated on a 30×20 mm^2 substrate. A substrate with a relative permittivity of 3.55 and thickness of 0.508 mm is used.

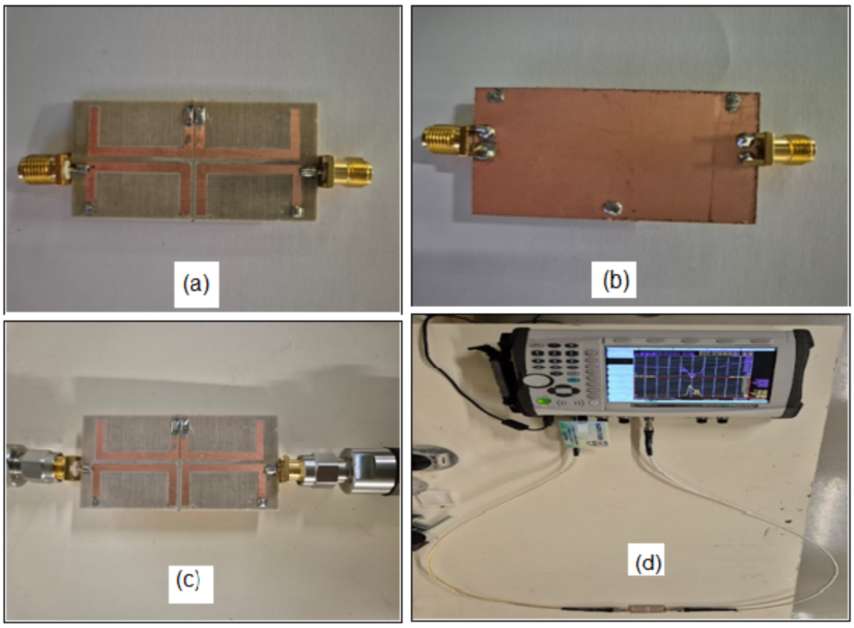

Figure 3.17: Photograph of the proposed filter. (a).(c) Top view, (b) layer view.(d) the experimental measurement.

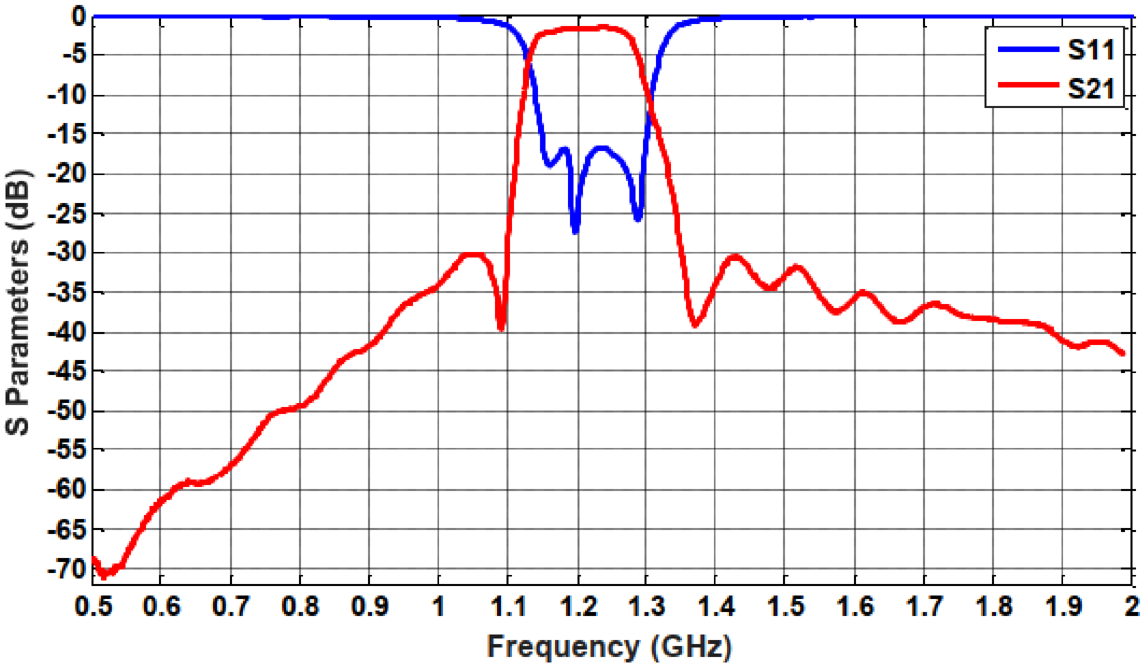

Figure 3.18: Measured S-parameter response.

Fig.(3.18) illustrates the measured outcomes of then cross-coupled filter. Shows that the suppression of out-of-band frequency in the measured data closely mirrors the results obtained through simulation. Comparable responses in the pass-band region are observed in simulations and actual measurements. The simulation data reveals:

≻ Bandwidth: 0.151 GHz

≻ Centre Frequency (f_C) : 1.2 GHz

This measured findings holds significant importance in confirming the efficacy of the filter design. The alignment between simulation and measurement results, particularly in out-of-band suppression and pass-band response, indicates the filter's functionality as intended.

3.8 filter design DualMode Open-Loop Resonators

3.8.1 Introduction

Microwave devices are increasingly prevalent today, making precise simulation before implementation essential. The second part of the chapter presents the design results of microwave filters achieved using the HFSS (High-Frequency Structure Simulator) soft ware.

This comprehensive tool facilitates the design of filters and the plotting of their frequency responses. In the second part of this chapter, we explore a new type of miniature microscopic dual-mode resonator for filter applications. The open-loop resonator is renowned for its versatility in designing cross-coupled resonator filters. Several filter examples demonstrate the applications of this innovative dual-mode resonator.

3.8.2 Bandpass Filter Based on an Electronic Circuit

The design of bandpass filters based on electronic circuits is based on the following steps: Specification: filter type, filter order n, filter ripple level, filter bandwidth BW, relative bandwidth FBW, cutoff frequency, and centre frequency determination of the values of the elements gi.

$\succ$ Calculation of then coupling elements $M_{i,i+1}$ and the external quality factors (Q_{e1} and Q), which are linked to the elements g_i.

$\succ$ Calculation of localised elements $R_0L_0C_0$ of resonators.

$\succ$ Calculation of series impedances of equivalent circuits with lumped elements.

3.8.3 Dual-Mode Open-Loop Resonators

3.8.3.1 Two-pole dual-mode open-loop resonators

Example A

- **Filter specifications:**

$Settings$	$Values$
$Filter\ order\ (Number\ of\ poles)$	02
$Type\ of\ approximation$	$Tchebychev$
$Central\ frequency\ f_0$	$1.063\ GHz$
$Bandwidth\ (BW)\ a-3\ dB$	$0.120\ GHz$
$Amplitude\ of\ l'ondulation\ LAr\ (passband\ ripple)$	$0.1\ dB$
$Attenuation$	$< -20\ dB$
TFZ	$fzt_1 = 1.1667\ GHz$

Table 3.5: The following Specifications of the filter.

• **Frequency response of the ideal bandpass filter**: Once the order of the filter is determined, knowing the maximum ripple of $0.1\ dB$ and the specifications defined in the specifications, we obtain the coefficients g_i $(i = 0, ..., 3)$ of the bandpass prototype of the type filter Tchebychev:

g_0	g_1	g_2	g_3
1	0.8431	0.6620	1.3554

Using the specifications defined in the specifications to calculate: Relative bandwidth:

$$\omega_0 = 2\pi f_0 = 6.675664 \tag{3.8.1}$$

$$FBW = \frac{BW}{f_0} = 0.1128 = 11.28\% \tag{3.8.2}$$

Quality Factor:

$$Q_{e1} = \frac{1}{ms1^2 \times FBW} = \frac{1}{1.0372^2 \times 0.1128} = 8.2407 \tag{3.8.3}$$

$$Q_{e2} = \frac{1}{ms2^2 \times FBW} = \frac{1}{0.6734^2 \times 0.1181} = 19.5499 \tag{3.8.4}$$

The resonant frequency :

$$f_{01} = f_0.\left(1 - \frac{m11 \times FBW}{2}\right) = 1.063 \times \left(1 - \frac{1.6127 \times 0.1181}{2}\right) = 0.96 \quad GHz \tag{3.8.5}$$

$$f_{02} = f_0.\left(1 - \frac{m22 \times FBW}{2}\right) = 1.063 \times \left(1 - \frac{-1.5589 \times 0.1181}{2}\right) = 1.1564\, GHz \tag{3.8.6}$$

Coupling coefficients:

$$M_{i,i+1} = \frac{1}{\sqrt{g_i g_{i+1}}} \tag{3.8.7}$$

Q_{e1}	M_{12}	M_{21}	Q_{e2}
8.2407	0.1578	0.1578	19.5499

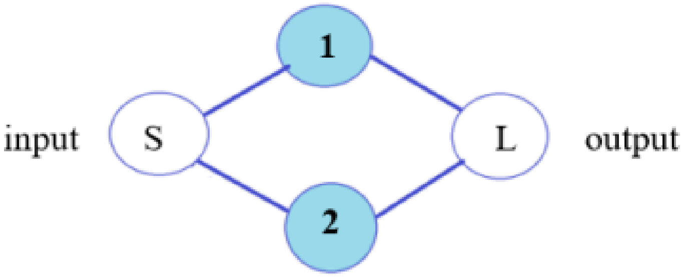

Figure 3.19: Coupling structure for a two pole dual-mode open-loop resonator filter ([22]).

- **Coupling matrix :**

$*$ *Normalized*: Where node S denotes the source or input, node L denotes the load or output, and nodes 1 and 2 represent the odd and even modes ([22]), respectively. For this coupling structure, an $n+2$ coupling matrix is given by:

$$m = \begin{bmatrix} 0 & m_{s1} & m_{s2} & 0 \\ m_{s1} & m_{11} & 0 & m_{L1} \\ m_{s2} & 0 & m_{22} & m_{L2} \\ 0 & m_{L1} & m_{L2} & 0 \end{bmatrix} \tag{3.8.8}$$

$$m = \begin{bmatrix} 0 & 1.0372 & 0.6734 & 0 \\ 1.0372 & 1.6127 & 0 & -1.0372 \\ 0 & 0 & -1.5589 & 0.6734 \\ 0 & -10372 & 06734 & 0 \end{bmatrix} \tag{3.8.9}$$

it should be noted that $m_{L1} = -m_{S1}$ for the odd mode and $m_{L2} = m_{S2}$ for the even mode. Using the formulations introduced in ([22])

$*$ *Dénormalized*: Aft er determining the normalized coupling matrix $[m]$ for a coupled resonator topology, the actual coupling matrix $[M]$ of a coupled resonator device with given specification can be calculated by prototype de-normalization of the matrix $[m]$ at a desired bandwidth, as follows:

$$M_{i,i+1} = m_{i,i+1} \times FBW \quad for \quad i = 1 \;\; to\; n - l \tag{3.8.10}$$

3.8.3.2 Filter equivalent circuit

The filter specifications result in desired coupling matrix elements $M_{i,i+1}, Q_e$ and Q_s. The circuit diagram for this filter is shown in Fig.(3.20), where the lumped elements $R_0L_0C_0$ represent the four synchronously tuned resonators and quarter-wave transmission lines, which have an electrical length EL $= \pm 90^0$ at frequency central f_0, The corresponding design parameters for the bandpass filter are: The localized elements $R_0L_0C_0$ of resonators:

$$L_0 = \frac{Z}{\omega_0 Q_e} \times 10^9 \;\; nH = 1.0273 \;\; nH \tag{3.8.11}$$

$$C_0 = \frac{Z}{\omega_0 Q_e} \times 10^{12} pF = 0.22364 \; pF \tag{3.8.12}$$

$$R_0 = 100000\ \Omega \tag{3.8.13}$$

Resonator impedances :

$$Z_{i,i+1} = \frac{Z}{Q_e M_{i,i+1}} \tag{3.8.14}$$

When $Z_0 = 50\Omega$ is the power supply impedance at the dE/S ports:

$$Z_{12} = 42.9497\ \Omega \tag{3.8.15}$$

The bandpass filter prototype operates using the characteristic impedance of the positive two-wave resonator lines and a parallel $R_0L_0C_0$ resonant circuit. After calculating the elements of the series and parallel branches, the equivalent circuit of the filter is illustrated in Fig.(3.20):

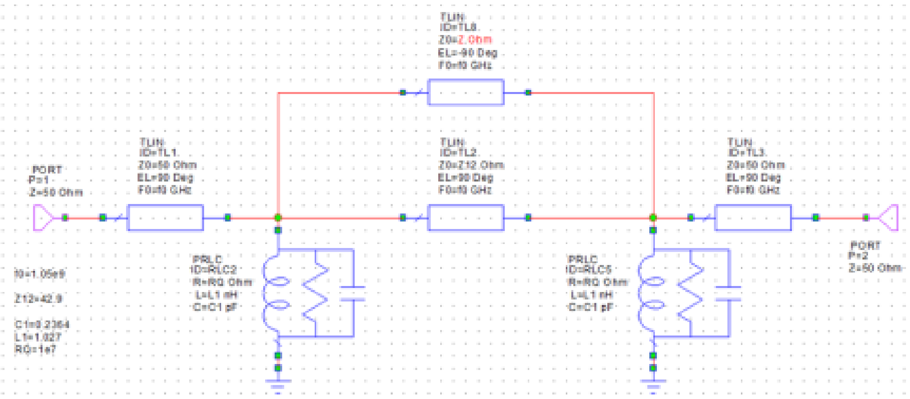

Figure 3.20: Bandpass filter with localized elements of order 2 with circuit resonant $R_0L_0C_0$ parallel.

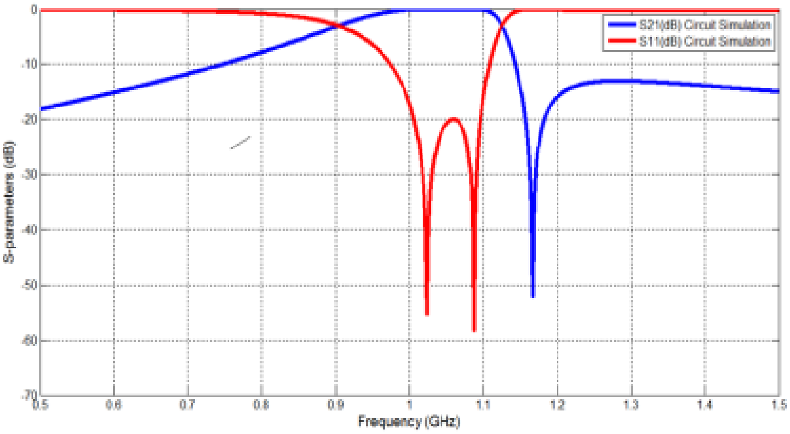

Figure 3.21: Ideal response of then Tchebychev bandpass filter of order 2.

The ideal response in transmission and reflection of the equivalent circuit in lumped elements, analyzed with AWR is shown in Fig.(3.21).

3.8.3.4 EM design of the bandpass filter in planar technology

Fig.(3.22) shows the basic topology of a dual-mode microscopic open-loop resonator. The dual-mode resonator consists of an open loop with an open gap, g.

The open loop has a line width of W_1 and assize of $L_{la} \times L_{lb}$. A loading element with an open stepped impedance stub is tapped from inside onto the open loop. The loading element has dimensions of L_{2a} and W_{2a} for the narrow line section and L_{2b} and W_{2b} for the wide-line section. The resonator is coupled to the input and output (I/O) ports with a feed structure with a W line width and coupling spacings. The port terminal impedance is W feed. The first two resonating modes, existing in the resonator of Fig.(3.22), are referred to as the odd and even modes.

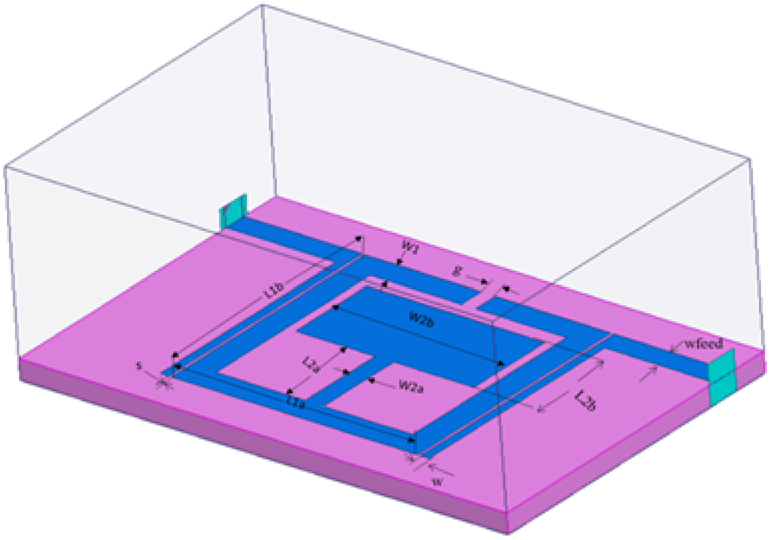

Figure 3.22: Topology of a dual-mode microscopic open-loop resonator.

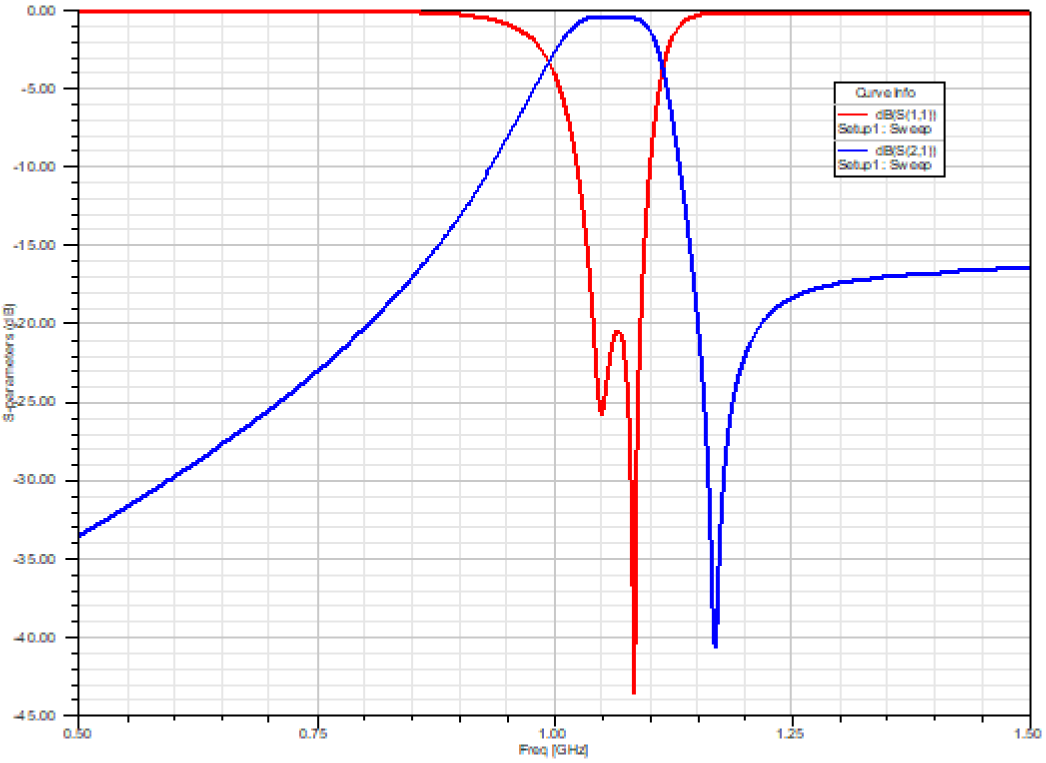

Figure 3.23: EM simulated responses of the filter whit HFSS.

We present in Fig.(3.23), the simulation results of the filter (two pole dual mode open- loop) and transmission obtained with the HFSS soft ware. The central frequency of this filter is of order 3 and $f = 1.063\ GHz$ and the bandwidth is approximately $0.120\ GHz$. The frequency response shows that $|S_{11}|$ is less than $-20\ dB$ between $0.89\ GHz$ and $1.02\ GHz$.

3.8.3.5 The Electromagnetic design of the applied filter

This geometric configuration is simulated on a $RO3010$ substrate having a relative permittivity $\epsilon_{\mathrm{r}} = 10.2$, a dielectric loss tangent 0.017 and a thickness of $h = 1.27\ mm$.

Settings	x_1	y_1	H	H_{s}	L_{la}	L_{lb}	L_{2a}	L_{2b}	W_{2a}	W_{2b}	s	g	W_{feed}	Wl
Values	20	30	0.017	1.27	15.1	15	5.5	5.5	0.7	8.1	0.2	0.9	2	1.5

Table 3.6: Planar bandpass filter dimensions for example A.

Example B

- **Filter specifications**:

$Settings$	$Values$
$Filter\ order\ (Number\ of\ poles)$	02
$Type\ of\ approximation$	$Tchebychev$
$Central\ frequency\ f_0$	$1.0155 GHz$
$Bandwidth\ (BW)\ a-3\ dB$	$0.120\ GHz$
$Amplitude\ of\ l`ondulation\ LAr\ (passband\ ripple)$	$0.1 dB$
$Attenuation$	$< -20\ dB$
TFZ	$fzt_1 = 0.8409\ GHz$

Table 3.7: The following specifications of the filter B.

Frequency response of the ideal bandpass filter: Once the order of the filter is determined, knowing the maximum ripple of $A_r = 0.1\ dB$ and the specifications defined in the specifications, we obtain the coefficients g_i $(i = 0, 1, 2, 3)$ of the bandpass prototype of the type filter Tchebychev:

g_0	g_1	g_2	g_3
1	0.8431	0.6620	1.3554

Using the specifications defined in the specifications to calculate: Relative bandwidth :

$$\omega_0 = 2\pi f_0 = 6.37734\ rad/s \qquad FBW = \frac{BW}{f_0} = 0.1181 = 11.81\% \quad (3.8.16)$$

Quality Factor:

$$Q_{e1} = \frac{1}{ms1^2 \times FBW} = \frac{1}{0.9024^2 \times 0.1181} = 10.398 \quad (3.8.17)$$

$$Q_{e2} = \frac{1}{ms2^2 \times FBW} = \frac{1}{0.5714^2 \times 0.1181} = 25.9340 \quad (3.8.18)$$

The resonant frequency :

$$f_{01} = f_0 \left(1 - \frac{m_{11} \times FBW}{2}\right) = 1.0155 \times \left(1 - \frac{-1.0918 \times 0.1181}{2}\right) = 1.08 \quad GHz \quad (3.8.19)$$

$$f_{02} = f_0 (1 - \frac{m_{22}.FBW}{2}) = 1.0155 \times (1 - \frac{1.3487 \times 0.1181}{2}) = 0.9346 GHz \quad (3.8.20)$$

Coupling coefficients:

$$M_{i,i+1} = \frac{1}{\sqrt{g_i g_{i+1}}} \tag{3.8.21}$$

Q_{e1}	M_{11}	M_{22}	Q_{e2}
10.398	0.1744	0.1744	25.9340

(3.8.22)

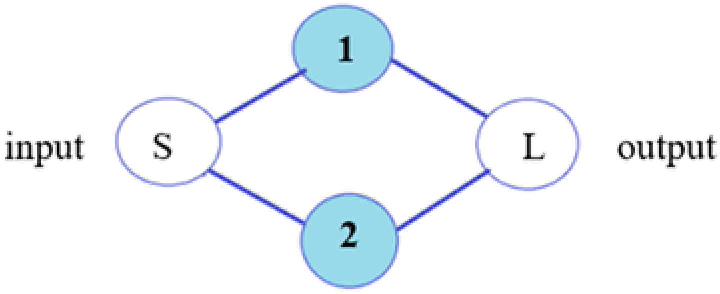

Figure 3.24: Coupling structure for a two-pole dual-mode open-loop resonator filter ([22])..

- **Coupling matrix**

$*$ *Normalized:* where the node S denotes the source or input, the node L denotes the load or output, and the nodes 1 and 2 represent the odd and even modes ([22]), respectively. For this coupling structure, an $n+2$ coupling matrix is given by:

$$m = \begin{bmatrix} 0 & 0.9024 & 0.5714 & 0 \\ 0.9024 & -1.0918 & 0 & -0.9024 \\ 0 & 0 & 1.3487 & 0.5714 \\ 0 & -09024 & 05714 & 0 \end{bmatrix} \tag{3.8.23}$$

it should be noted that $m_{L1} = -m_{S1}$ for the odd mode and $m_{L2} = m_{S2}$ for the even mode. Using the formulations introduced in ([22])

- **Filter equivalent circuit:**

The localized elements $R_0 L_0 C_0$ of resonators:

$$L_0 = \frac{Z}{\omega_0 Q_e} \times 10^9 \; nH = 1.255 \;\; nH \tag{3.8.24}$$

$$C_0 = \frac{Z}{\omega_0 Q_e} \times 10^{12} \; pF = 0.22364 \; pF \tag{3.8.25}$$

$$R_0 = 100000 \; \Omega \tag{3.8.26}$$

Resonator impedances :

$$Z_{i,i+1} = \frac{Z}{Q_e M_{i,i+1}} \tag{3.8.27}$$

When $Z_0 = 50\ \Omega$ is the power supply impedance at the I/O ports:

$$Z_{12} = 42.9497\ \Omega \tag{3.8.28}$$

Equivalent scheme under AWR

The band pass filter prototype operates using the characteristic impedance of the positive two-wave resonator lines, and a parallel $R_0L_0C_0$ resonant circuit. After calculating the elements of the series and parallel branches, the equivalent circuit of the filter is illustrated in Fig.(3.25):

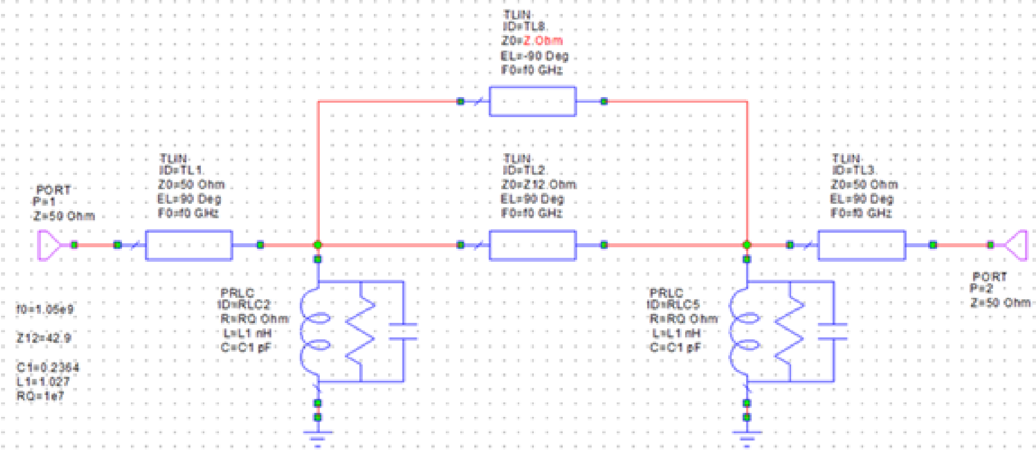

Figure 3.25: bandpass filter with localized elements of order 2 with circuit resonant *RLC* parallel..

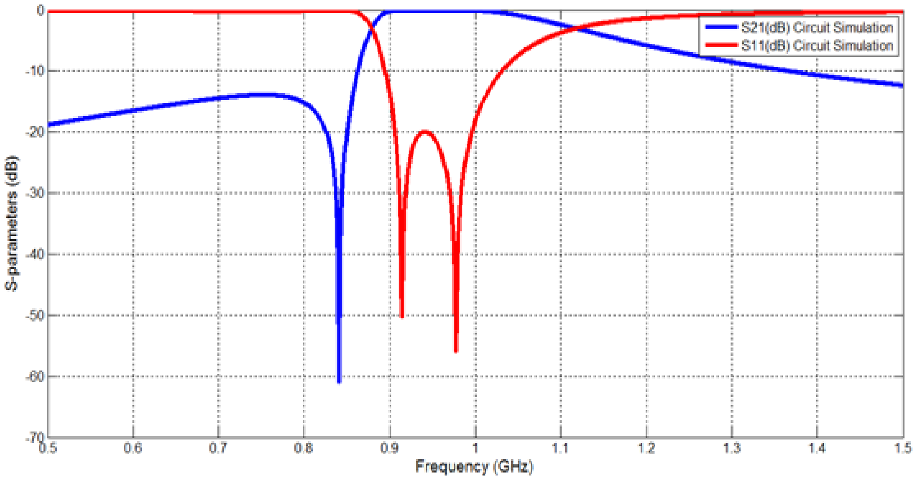

Figure 3.26: Ideal response of then Tchebychev bandpass filter of order 2.

The ideal response in transmission and reflection of the equivalent circuit in lumped elements, analyzed with AWR is shown in Fig.(3.26).

EM design of the bandpass filter in planar technology

Fig.(3.27) displays the layout of the designed filter. The two small open stubs attached to the loading element inside the open loop are deployed for additional control of the even- mode characteristics, which also allow efficient utilization of the circuit area inside the open loop

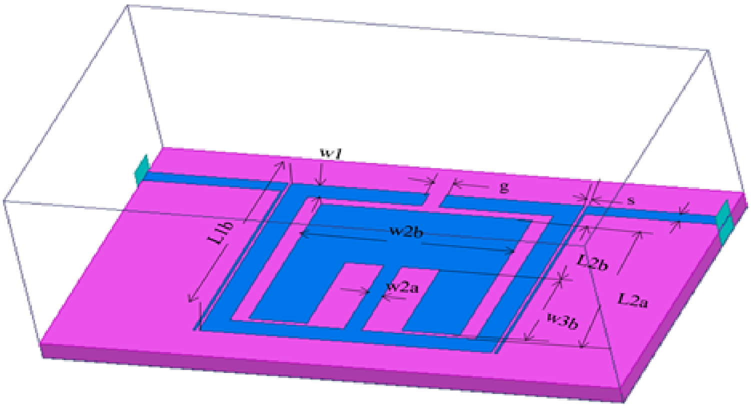

Figure 3.27: Topology of a two-port microscopic dual-mode open loop filter.

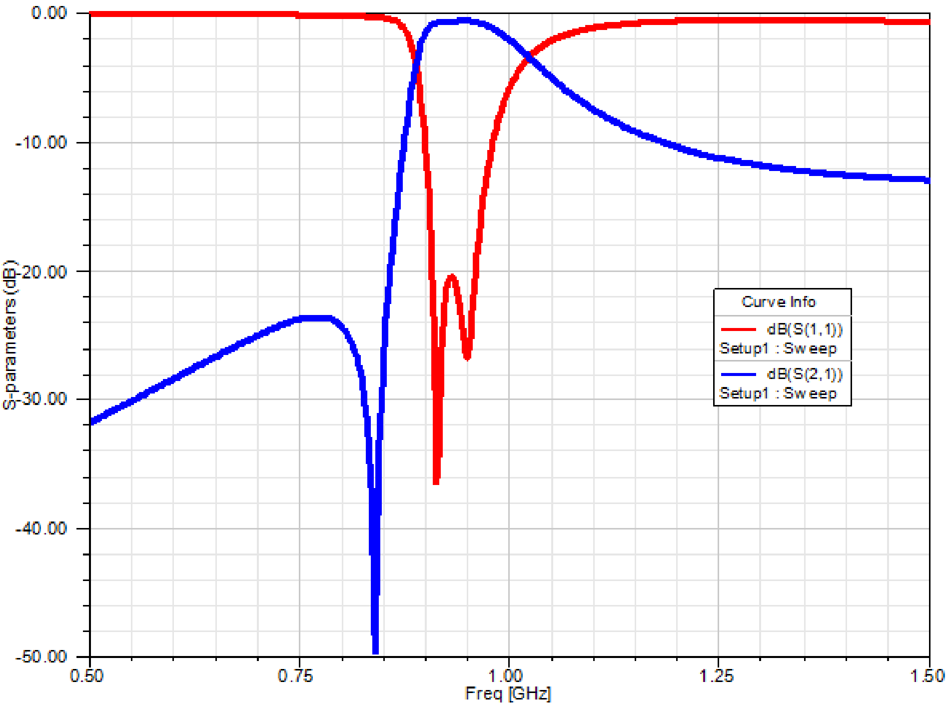

Figure 3.28: EM-simulated responses of then filter with HFSS.

We present in Fig.(3.28), the simulation results of the filter (two pole dual mode open-loop) and transmission obtained with the **HFSS** soft ware. The central frequency of this filter is of order 3 and $f = 1.0155\ GHz$ and the bandwidth is approximately $0.120\ GHz$. The frequency response shows that $|S|$ is less than $-20\ dB$ between $0.89\ GHz$ and $1.02\ GHz$.

3.8.4 The Electromagnetic Design of the Applied Filter

This geometric configuration is simulated on a $RO3010$ substrate having a relative permittivity $\epsilon_{\mathrm{r}} = 10.2$, a dielectric loss tangent 0.017 and a thickness of $h = 1.27\ mm$.

Settings	x_1	y_1	H	L_{1a}	L_{1b}	L_{2a}	L_{2b}
Values	20	30	0.017	1.27	15.1	15	5.5
Settings	W_{2a}	W_{2b}	s	g	W_{feed}	W_1	
Values	0.7	8.1	0.2	0.9	2	1.5	

Table 3.8: the filter dimensions for example B.

3.8.5 The Dimensions

The first two resonating modes, existing in the resonator of Fig. (3.28), are referred to as the odd and even modes, Depending on the dimensions of the resonator these two modes can have the same or different modal frequency and, for the latter, the modal resonant frequency of one mode can be either higher or lower than that of the other one. The characteristics of the dual-mode open-loop resonator are investigated by full-wave electromagnetic (EM) simulation. To excite the resonator, two ports are weakly coupled to the resonator with a large spacing s.

3.8.6 Field Distribution

The HFSS soft ware was used to perform a frequency analysis in the (land 2) GHz band L of this structure. Fig.(3.29) illustrate the distribution of then field lines. electrical bandpass filter and electric field mapping of the filter

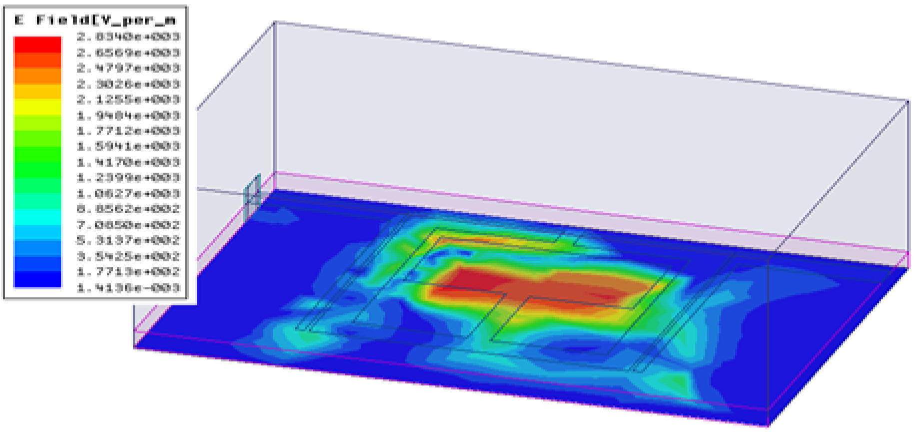

Figure 3.29: Distribution of the electric field of the $3th$ order bandpass filter.

3.8.7 Three -pole Dual-Mode Open-Loop Resonators

- **Filter specifications:**

$Settings$	$Values$
$Filter\ order\ (Number\ of\ poles)$	03
$Type\ of\ approximation$	$Tchebychev$
$Central\ frequency\ f_0$	$1.05\ GHz$
$Bandwidth\ (BW)\ a - 3\ dB$	$0.115\ GHz$
$Amplitude\ of\ l'ondulation\ LAr\ (passband\ ripple)$	$0.1\ dB$
$Attenuation$	$< -20\ dB$
TFZ	$fzt_1 = 1.0955\ GHz$

Table 3.9: the specifications of the filter C.

3.8.7.1 Frequency response of the ideal bandpass filter

Once the order of the filter is determined, knowing the maximum ripple of $A_r = 0.1\ dB$ and the specifications defined in the specifications, we obtain the coefficients g_i, $(i = 1, ..., 4)$ of the bandpass prototype of the type filter Tchebychev:

N	g_1	g_2	g_3	g_4
3	1.0316	1.1474	1.0316	1.0000

Using the specifications defined in the specifications to calculate:

Relative bandwidth:

$$\omega_0 = 2\pi f_0 = 6.594\ rad/s \qquad FBW = \frac{BW}{f_0} = 0.1095 = 10.95\% \tag{3.8.29}$$

Quality Factor:

$$Q_{e1} = \frac{1}{ms1^2 \times FBW} = \frac{1}{0.85^2 \times 0.1095} = 12.64 \tag{3.8.30}$$

$$Q_{e2} = \frac{1}{ms2^2 \times FBW} = \frac{1}{0.58^2 \times 0.1095} = 27.1475 \tag{3.8.31}$$

Coupling coefficients:

$$M_{i,i+1} = \frac{1}{\sqrt{g_i g_{i+1}}} \tag{3.8.32}$$

Q_{e1}	M_{11}	M_{22}	M_{33}	Q_{e2}
12.64	0.1744	0.1744	0.1744	27.1475

(3.8.33)

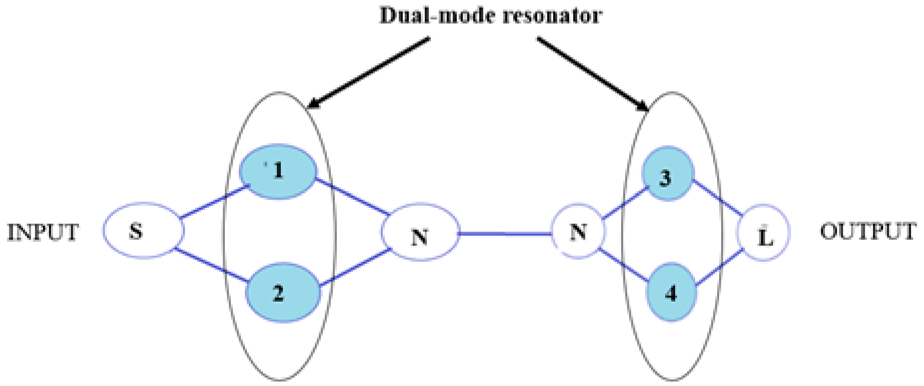

Figure 3.30: Order 3 coupling graph of the filter ([22]).

Coupling matrix

∗ *Normalized:*

The extracted coupling matrix is given by :

$$m = \begin{bmatrix} 0 & 0.58 & 0.58 & 0.01 & 0 & 0 & 0 & 0 \\ 0.58 & 0.96 & 0 & -0.85 & 0 & 0 & 0 & 0 \\ 0.58 & 0 & -1.01 & 0.85 & 0 & 0 & 0 & 0 \\ 0.01 & -0.85 & 0.58 & 0 & 1.1 & 0 & 0 & 0 \\ 0 & 0 & 0 & 1.1 & 0.74 & -0.6 & 0.46 & 0.01 \\ 0 & 0 & 0 & 0 & 0.46 & 0 & 1.06 & 0.46 \\ 0 & 0 & 0 & 0 & 0.01 & -0.7 & 0.46 & 0 \end{bmatrix} \tag{3.8.34}$$

Filter equivalent circuit

The localized elements $R_0L_0C_0$ of resonators:

$$L_0 = \frac{Z}{\omega_0 Q_e} \times 10^9 \ nH = 1.1075 \ nH \tag{3.8.35}$$

$$C_0 = \frac{Z}{\omega_0 Q_e} \times 10^{12} \ pF = 0.23336 \ \ pF \tag{3.8.36}$$

$$R_0 = 100000 \ \Omega \tag{3.8.37}$$

Resonator impedances:

$$Z_{i,i+1} = \frac{Z}{Q_e M_{i,i+1}} \tag{3.8.38}$$

When $Z_0 = 50 \ \Omega$ is the power supply impedance at the I/O ports:

$$Z_{12} = 42.9497 \ \Omega \tag{3.8.39}$$

$$Z_{23} = 54.4571 \ \Omega \tag{3.8.40}$$

The bandpass filter prototype operates using the characteristic impedance of the positive two-wave resonator lines and a parallel $R_0L_0C_0$ resonant circuit. After calculating the elements of the series and parallel branches, the equivalent circuit of the filter is illustrated in Fig.(3.31)

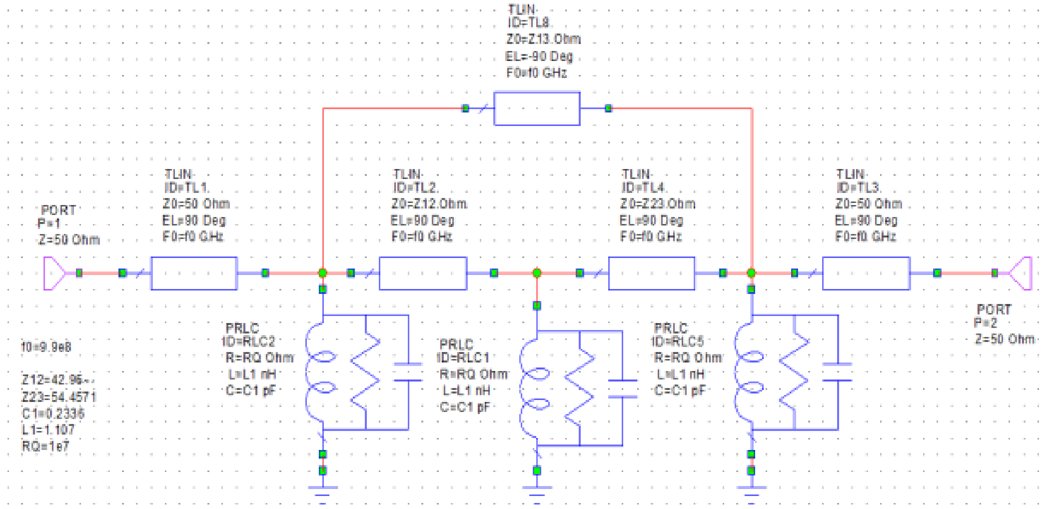

Figure 3.31: bandpass filter with localized elements of order 3 with circuit resonant $R_0L_0C_0$ parallel.

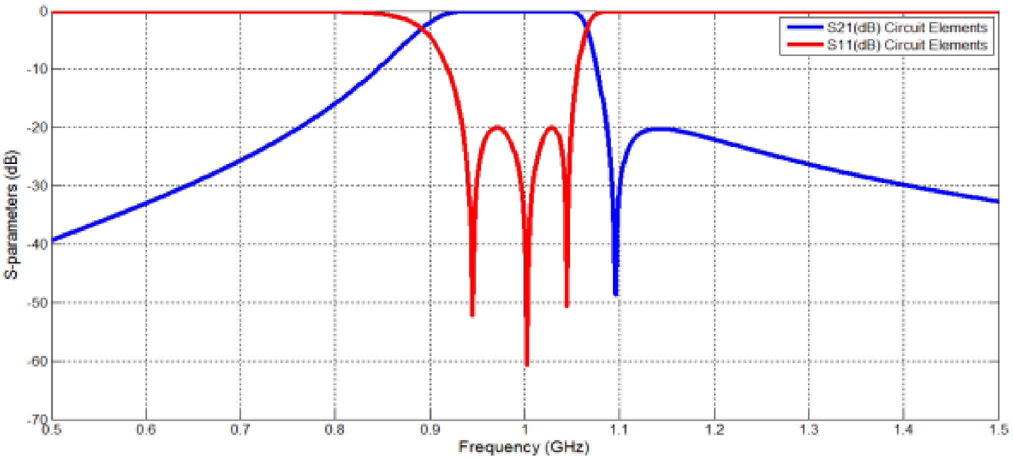

Figure 3.32: Ideal response of the Tchebychev bandpass filter of order 3.

Fig.(3.32) shows the ideal transmission and reflection response of the equivalent circuit in lumped elements analyzed with AWR. Our bandpass filter's frequency response appears to be centred on 1.05 GHz.

3.8.8 Design of the Bandpass Filter in Planar Technology

Fig.(3.33) a displays the layout of the designed filter. The two small open stubs attached to the loading element inside the open loop are deployed for an additional control of the even- mode characteristics, which also allow an efficient utilization of the circuit area inside the open loop

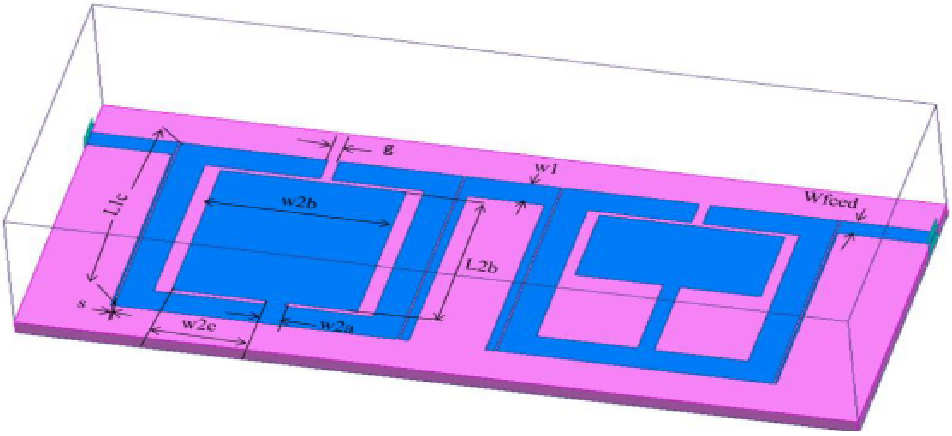

Figure 3.33: Structure of filter with three resonators.

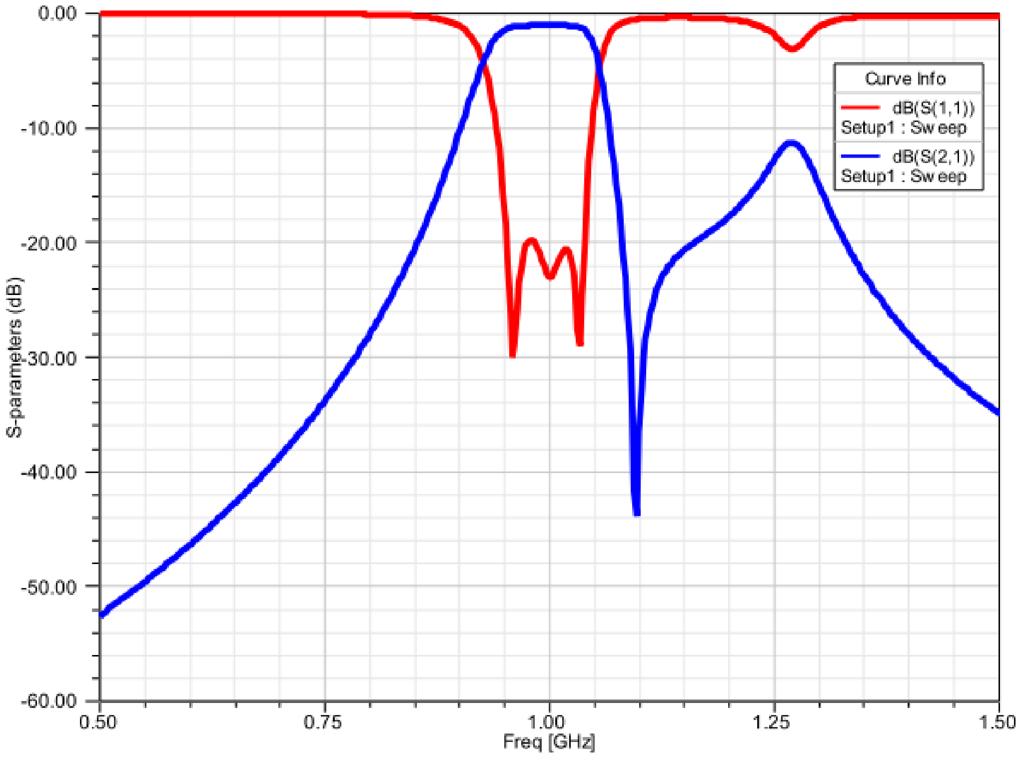

Figure 3.34: EM-simulated responses of the filter with HFSS.

We present in Fig.(3.34), the simulation results of the filter (four pole dual mode open-loop) and, transmission obtained with the HFSS soft ware. The central frequency of this filter is of order 3 and $f = 1.05\ GHz$ and the bandwidth is approximately $0.115\ GHz$. The frequency response shows *that* $|S_{ll}|$ is less than $-20\ dB$ between $0.9277\ GHz$ and $1.0559\ GHz$.

3.8.9 Influence of Geometric Parameters

3.8.9.1 Variation of via hole diameter W_1

The following curves present the influence of some geometric parameters on the frequency response of the parameters S. Fig.(3.35) shows the variations of the coefficient reflection and transmission as a function of frequency, taking the diameter of the via (W_1) as set to vary. In our simulation, we chose three diameter values: $W1 = 1.51\ mm$, $W1 = 1.71\ mm$ (this is the reference model), $W1 = 1.91\ mm$.

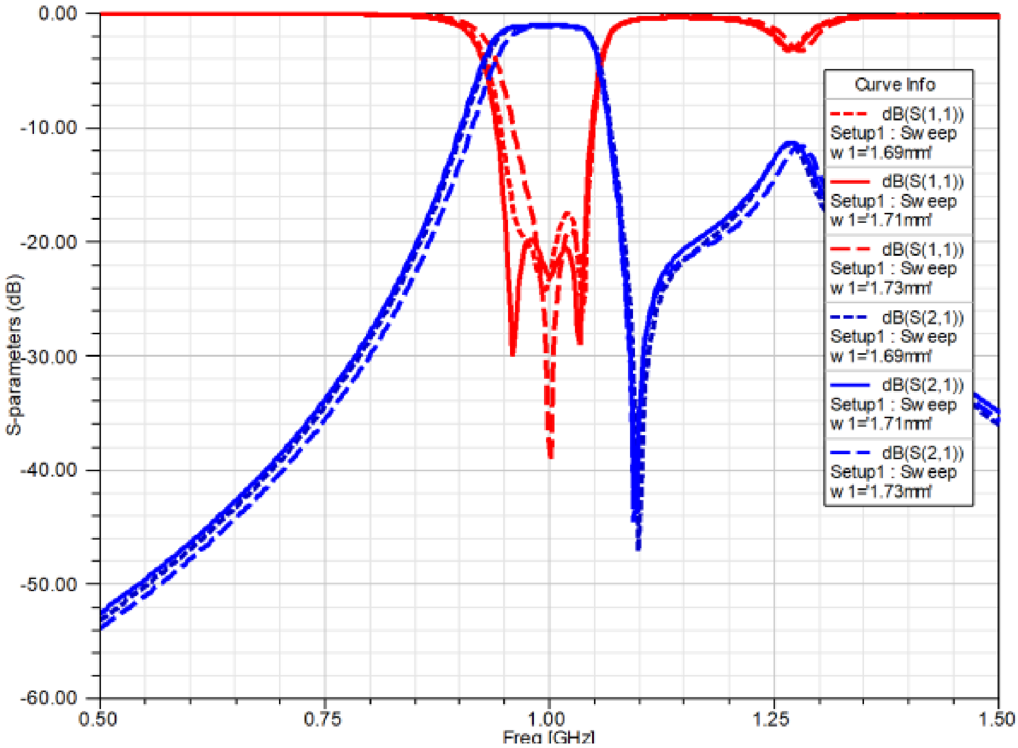

Figure 3.35: Simulation results of the planar technology cell proposed with different $-W_1$ values.

3.8.9.2 The effect of the spacing S on the frequency response of the filter

The first parametric study shows the influence of the S_1 spacing on the simulation results Fig.(3.36). When the S_1 space increases (space between the first resonator and the second resonator), we can see that the bandwidth decreases, which implies a narrower bandwidth. We can also see that the best result we obtained is at the value $S_1 = 0.62$ mm of reflection losses below -20 dB and bandwidth between 0.925 GHz and 1.075 GHz.

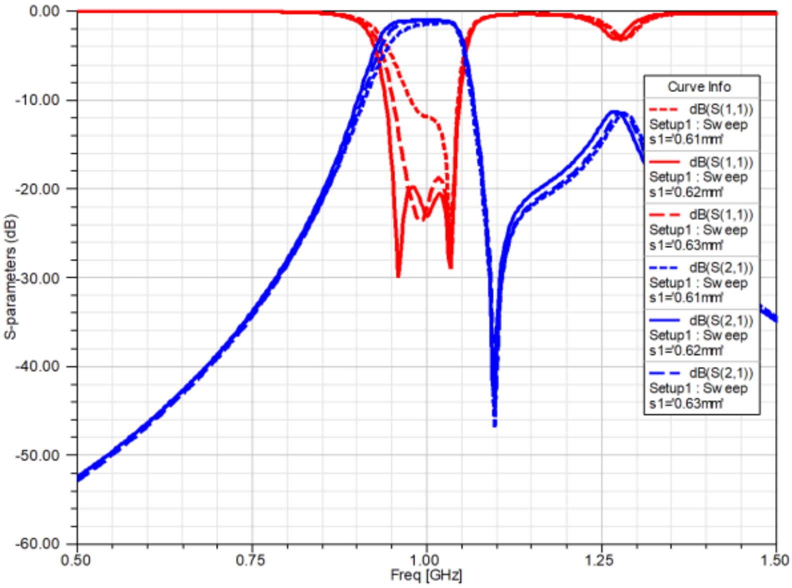

Figure 3.36: Shows the proposed HFSS simulation results with different values of S_2.

This second parametric study shows the influence of the $'S_2'$ spacing between the second and third resonators. When $'S_2'$ increases, the lower cutoff frequency remains the same and the upper cutoff frequency moves lower. Therefore, $'S_2'$ is the second parameter that affects the $HFSS$ result: when $'S_2'$ increases, the reduced bandwidth.

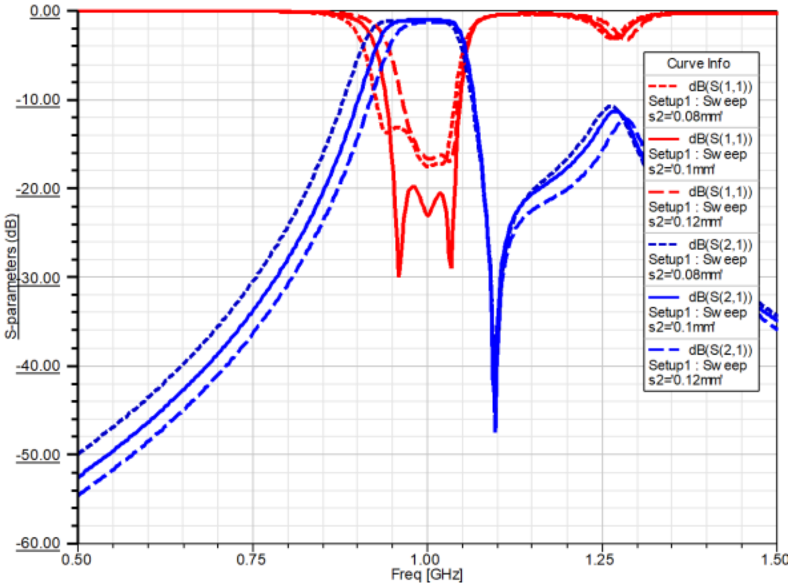

Figure 3.37: Résultats de simulation HFSS proposée with différentes valuers de S_2.

The electric field distribution of then proposed bandpass filter is shown in Fig.(3.38)

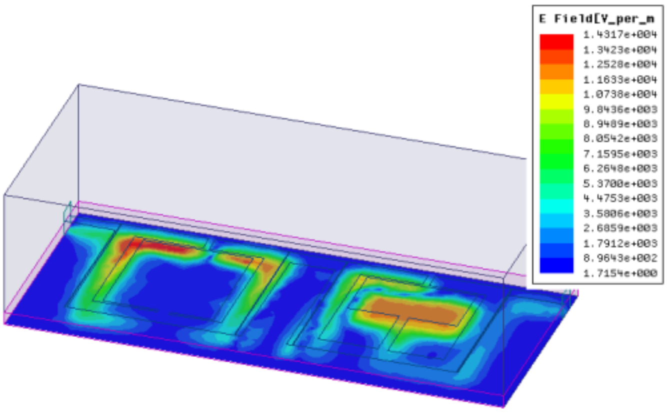

Figure 3.38: Distribution of then electric field of the $3rd$-order bandpass filter.

Fig.(3.38) illustrates the electric field distribution of the $3rd$-order bandpass filter. We notice that the maximum of the E fields is represented by dark colors (high intensity)

In all cases, only one modal resonant frequency is affected, while the other is hardly changed. It can be shown that the mode whose resonant frequency is being affected is an even mode.

3.9 Conclusion

This chapter concludes with an analytical method using Tchebychev polynomials to calculate the synthesis parameters of a bandpass microscopic cross-coupled filter. The technique involves the following steps: determining the coupling matrix, establishing the quality factor (Q-factor) coefficients crucial for filter performance, and defining the initial geometric dimensions. Additionally, a novel miniature microscopic dual-mode resonator for filter applications is explored. This open-loop resonator stands out for its versatility in designing cross-coupled resonator filters. Various examples highlight the innovative applications of this dual-mode resonator, demonstrating its potential to advance filter design technology.

Chapter 4

Analytical and Synthesis filters Design Substrate Integrated Waveguide (SIW)

4.1 Introduction

In this chapter, we present analytical and synthesis filters design substrate integrated waveguide (SIW), a method for creating waveguide, which are structures that guide electromagnetic waves from one point to another. SIW technology finds particular application in microwave and millimeter-wave frequency. The innovation of SIW lies in its ability to integrate waveguide structures into planar substrates, such as printed circuit boards (PCBs), offering a bridge between traditional waveguide technology and planar circuitry. This integration facilitates the development of more compact, lightweight, and cost-effective high-frequency components and systems.

We created an SIW waveguide, embedding two rows of metallic copper in a dielectric substrate and placing them between two parallel metal plates (usually the top and bottom layers of a PCB). These vias and plates form a rectangular waveguide structure that confines and guides electromagnetic waves. The SIW's dimensions, like traditional waveguide, determine the operational frequency band and the mode of propagation of the electromagnetic waves within it.

SIW technology has the following critical advantages:

Reduced Size and Weight: By integrating waveguide structures into planar substrates, SIW components are smaller and lighter than their conventional counterparts.

Lower Cost: SIW can leverage standard PCB manufacturing processes, reducing the cost of high-frequency components and systems.

High Performance: SIWs maintain the high-quality factor and low loss characteristics of traditional waveguide, which is beneficial for high-frequency applications.

Integration and Compatibility: SIW makes putting complex microwave and millimeter-wave circuits on a single substrate easier by connecting to other flat systems and components.

SIW technology has found applications in various areas, including antennas, filters, couplers, and more, particularly in sectors such as telecommunications, radar systems, and satellite communications, where high-frequency performance is critical. Its development and adoption continue to grow as demands for compact, high-performance, and cost-effective microwave and millimeter-wave components increase.

4.2 Analytical Design and Optimization of Hexagonal cavities

4.2.1 Equivalent Circuits and Analysis

The most basic CT filter is a three-pole trisection filter, which serves as the building block for filters with a higher degree. The operation of the device is illustrated in Fig.(4.1) (a), where the coupling coefficients M_{12} and M_{23} symbolize the connections between resonators that are adjacent to one another, M_{13} represents the cross-coupling, and Q_{e1} andQ_{e3} correspond to the input and output couplings, respectively. The formula for calculating the resonant angular frequency of resonator i is $1/\sqrt{L_i C_i} = \omega_{0i} = 2\pi f_{0i}$. Trisection filters may have a symmetrical physical configuration despite the fact that their frequency response ought to be asymmetric. To simplify, we will denote M_{12} as M_{23}, Q_{e1} as Q_{e3}, and ω_{01} as ω_{03}.

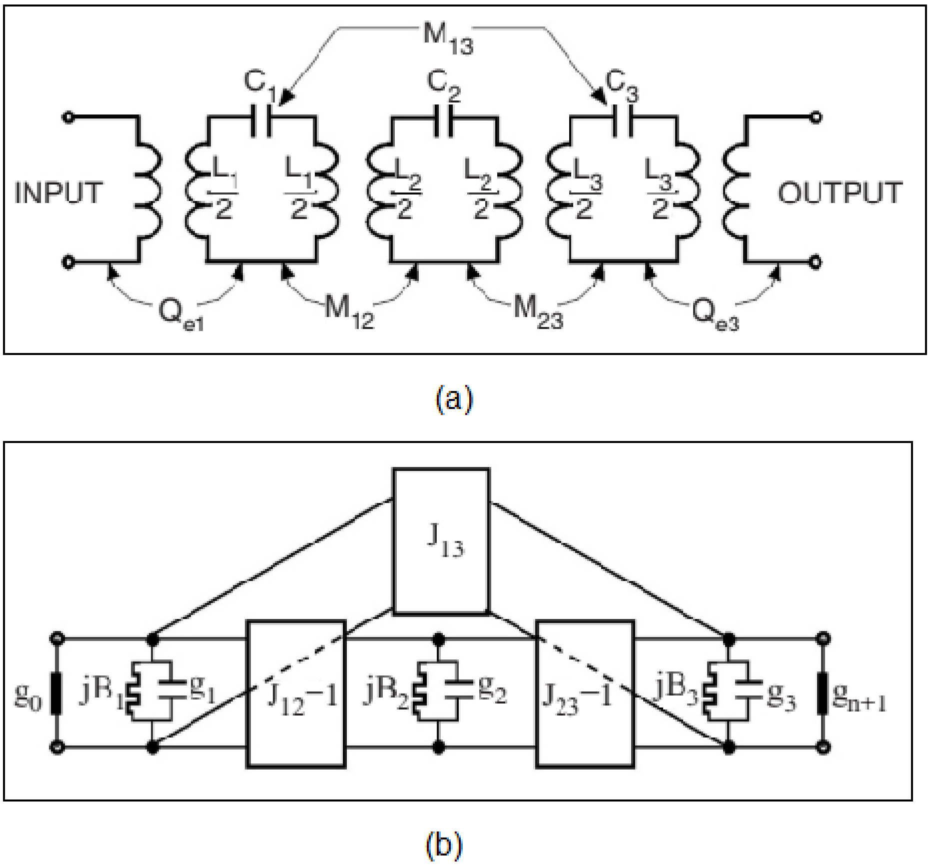

(a)

(b)

Figure 4.1: (a) An equivalent trisection bandpass filter circuit. (b) Prototype low pass filter associated with it [10].

The selectivity at a limited frequency, M_{13}, will be determined by the cross-coupling [19]. The external quality factors at the input and output ports are denoted by Q_{e1} and Q_{e3}. Due to the attenuation pole on one side of the passband of a trisection filter, asynchronous tuning of the resonators is necessary to produce an asymmetric filter frequency response. As a result, each resonator may have a different resonance frequency, which must be selected to meet the filter specifications. [46] Determine resonator I's angular resonant frequency.

$$\omega_{0i} = \frac{1}{\sqrt{LiCi}} 2\pi f_{0i} \quad for \quad i = 1, 2, 3 \tag{4.2.1}$$

The equivalent circuit's capacitance and inductance values are L_i and C_i. Although the frequency response is symmetric, the following presumptions are made to maintain the symmetry of the filter's physical construction [19].

$$M_{12} = M_{23} \tag{4.2.2}$$

$$Q_{e1} = Q_{e3} \tag{4.2.3}$$

$$\omega_{01} = \omega_{03} \tag{4.2.4}$$

The low-pass prototype filter in Fig.(4.1) (a) is derived from the corresponding circuit in Fig.(4.1) (b). J inverters are used with [19].

$$J_{12} = J_{23} \tag{4.2.5}$$

Fig.(4.1) (b) depicts the lowpass prototype of the suggested filter. J_{ij} is the typical admittance of the inverter, and each resonator is a frequency-invariant admittance inverter. In this instance, $J_{12} = J_{23} = 1$ for the inverters situated along the filter's primary channel. Cross-coupling between neighboring resonators is considered by the bypass inverter with a typical admittance of J_{13} [19]. The symbols gi and B_i $(i = 1, 2, 3)$ indicate the low pass prototype filter's capacitance and frequency invariant susceptance. The resistive terminations at the input and output ports are denoted by g_0 and g_4.

$$g_0 = g_4 \ ; \quad g_1 = g_3 \tag{4.2.6}$$

$$B_1 = B_3 \tag{4.2.7}$$

A synthesis method could be used to find the values of the unknown low-pass elements [11]. We can solve for L_i and C_i by using the low pass-to-band pass frequency transformation plus a little bit of modification.

$$C_i = \frac{1}{\omega_0}(\frac{g_i}{FBW} + \frac{Bi}{2}) \ , \quad L_i = \frac{1}{\omega_0}(\frac{g_i}{FBW} + \frac{B_i}{2}) \tag{4.2.8}$$

$$\omega_{0i} = \frac{1}{\sqrt{L_i C_i}} = \omega_0 \sqrt{1 - \frac{B_i}{\frac{g_i}{FBW} + \frac{B_i}{2}}} \tag{4.2.9}$$

The fractional bandwidth of the bandpass filter is denoted by FBW, the angular frequency in the center frequency is represented by ω_0, and the angular resonance frequency of the I_{th} resonator is represented by ω_{0i}.

To obtain the coupling coefficients and external quality factors [19] equations , we must first determine the susceptance slope parameter for each shunt resonator in Fig.(4.1) (a). This is done as follows:

$$b_i = \omega_{0i} C_i = \frac{\omega_{0i}}{\omega_0}(\frac{g_i}{FBW} + \frac{B_i}{2}) \tag{4.2.10}$$

It is, therefore, possible to determine the coupling coefficient $M_{ij,}$ the external quality factor, Q_{e1} and Q_{en}, and [30]:

$$Q_{e1} = \frac{b_i}{g_0} = \frac{\omega_{0i}}{g_0 \omega_0}(\frac{g_i}{FBW} + \frac{B_i}{2}) \tag{4.2.11}$$

$$Q_{en} = \frac{b_n}{g_{n+1}} = \frac{\omega_{0i}}{g_{n+1} \omega_0}(\frac{g_n}{FBW} + \frac{B_n}{2}) \tag{4.2.12}$$

$$M_{ij/i \neq j} = \frac{J_{ij}}{\sqrt{(b_i b_j}} = \frac{\omega_0}{\sqrt{\omega_{0i} \omega_{0j}}}(\frac{FBW.J_{ij}}{\sqrt{(\frac{g_i}{FBW} + \frac{B_i}{2})(\frac{g_i}{FBw} + \frac{Bj}{2})}} \tag{4.2.13}$$

Where n is the filters degree or the resonator number.

4.2.2 Trisection Filter Design

This introduces a novel three-pole bandpass hexagonal resonator filter design utilizing SIW technology for mobile and communication systems. The design is focused on meeting stringent specifications without sacrificing size and electrical performance. They propose innovative hexagonal resonators employing SIW technology and circular cavities. The filter design offers flexibility, accommodating centre frequency of 7.95 GHz with various fractional bandwidths. The structures are simulated using the High-Frequency Structure Simulator software developed by Ansoft

4.2.2.1 Specifications and Initial Compline Filter Model

The filter has been meticulously engineered to adhere to the specified requirements in the Table below:

Center frequency	f_0= 7.95 GHz
Bandwidth	BW= 0.28GHz (FBW=14%)
Pass band ripple	LAR = 0.0431dB
Pass band return loss	RL=20dB
Stop band rejection level	40 dB

Table 4.1: The specified target parameters for the Substrate Integrated Waveguide (SIW) bandpass filter are detailed below

The utilization of a Third-order Tchebychev low-pass prototype filter with a ripple level of 0.04321 dB was initially incorporated into the amalgamated Filter designs [46]. The low-pass prototype filter underscores the requirement for a filter order of $n = 3$. The characteristics of the low-pass prototype filter are defined by the parameters [15]:

g_0	g_1	g_2	g_3	g_4
1	1.0316	1.1474	1.0316	1

The generalized coupling matrix and the scaled external quality actors are utilized in dimensional synthesis, dependent upon the centre frequency and absolute bandwidth. The relationships expounded in references [[31], [47]] are pivotal in the process of de-normalizing the normalized coupling matrix.

$$Q_{es} = \frac{g_0 g_1}{FBW}, \quad Q_{eL} = \frac{g_n g_{n+1}}{FBW} \tag{4.2.14}$$

$$M_{i,J+1} = \frac{FBW}{\sqrt{g_i g_{i+1}}}, \quad i = 1 \ to \ \ n-1 \tag{4.2.15}$$

$$m_{i,i+1} = \frac{M_{i,i+1}}{FBW}, \quad i - 1, ...n \tag{4.2.16}$$

The lowpass prototype filter is characterised by the values g_0, g_1, g_2, g_3, and g_4. FBW is an acronym that stands for fractional bandwidth. The composite filter is specifically engineered to function at a frequency of 7.95 GHz. The formulas [46] may be used to calculate the coupling matrix of the filter and the scaled denormalized external quality factors [46]. The coupling matrix can be calculated using the equations provided in [46]. By determining the scaled denormalized external quality factors, the performance of the filter at 7.95 GHz can be further analyzed and optimized for specific requirements. This meticulous approach ensures that the lowpass prototype filter operates effectively within the desired fractional bandwidth, meeting the necessary specifications for its intended application.

$$m = \begin{bmatrix} 0 & 0.9192 & 0.9192 \\ 0.9192 & 0 & 0.192 \\ 0.9192 & 0.9192 & 0 \end{bmatrix} \tag{4.2.17}$$

$$Q_{es} = \frac{g_0 g_1}{FBW} = 29.1059 \tag{4.2.18}$$

Q_e	M_{12}	M_{23}	M_{13}	Q_s
29.1059	0.0326	0.0326	0.0344	29.1059

he equation illustrates the correlation between: $Q_{e,s}$: the external quality factor of the input and output ports, f_{0i}: the resonance frequency of each resonator, and M_{ij}: the coupling coefficient between two neighbouring resonators ([10]).

The capacitance C_0 and inductance L_0 have been calculated, with the value of each being determined through the utilization of the following formulas ([19]):

$$C_0 = \frac{Q_{eS}}{\omega_0 \times Z} = 11.727\ pF \tag{4.2.19}$$

$$L_0 = \frac{Z}{\omega_0 \times Q_{eS}} = 346.08\ nH \tag{4.2.20}$$

The series impedances Z_{12}, Z_{23}, Z_{34} are ([11]):

$$Z_{i,i+1} = \frac{Z}{M_{i,i+1} \times Q_{eS}} \tag{4.2.21}$$

Z_i	L_0,C_0	f_0 (GHz)
$Z = 50\ \Omega$	$L_0 = 346.08\ nH$	$7.95\ GHz$
$Z_{31} = 50\ \Omega$	$C_0 = 11.722\ pf$	
$Z_{12} = 52.731\ \Omega$		
$Z_{23} = 52.731\ \Omega$		

Table 4.2: Capacitance C_0, Inductance L_0, Impedance Z_i

Fig.(4.2) shows two coupling structures in cascaded trisection or CT filters: primary or direct coupling and cross-coupling. Each CT section consists of three directly coupled resonators with cross-coupling, generating a singular attenuation pole at a specific frequency, with positive cross-coupling causing the pole to appear on the lower passband.

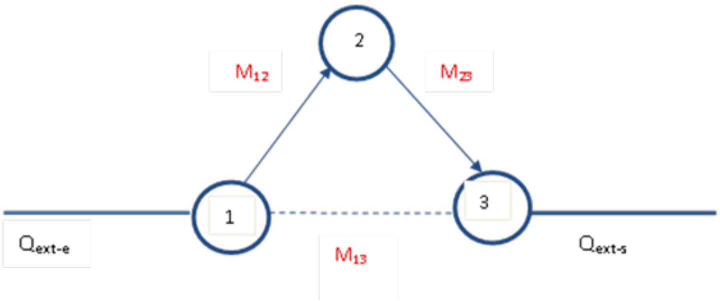

Figure 4.2: Coupling structures that are characteristic of cascaded trisection (CT) filters. ([2]).

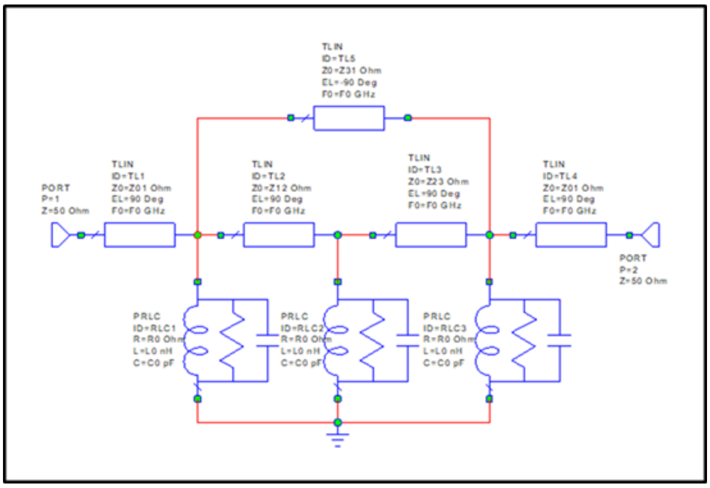

Figure 4.3: AWR Office schematic circuit for the synthesis of a three-pole filter.

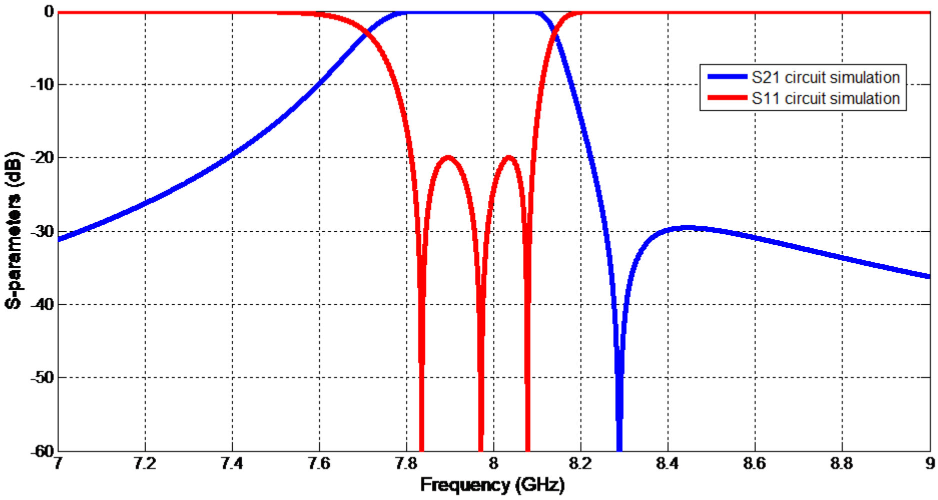

Figure 4.4: Frequency response analysis of the third-order filter about the specified design objectives..

4.2.3 Group Delay Method

Fig.(4.5) ([19]) depicts the analogous circuit of the first resonator when connected to the input feed source. Conductance G signifies the input coupling.

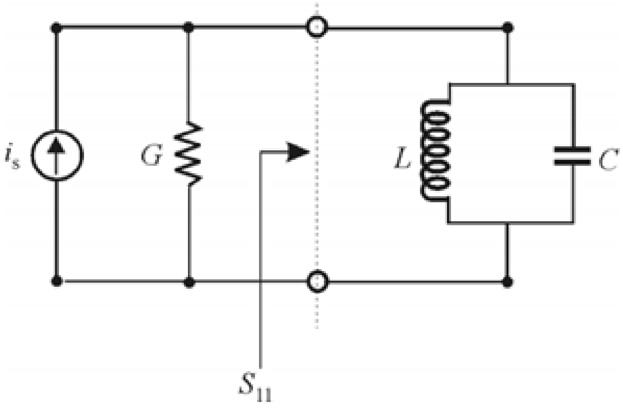

Figure 4.5: The circuit equals the element positioned for the group delay ([19]).

The reflection coefficient looking into the single resonator, with respect to a feed line of characteristic admittance G, is given by ([3]).

$$S_{11} = \frac{G - Y_{in}}{G + Y_{in}} = \frac{1 - Y_{in}}{1 + Y_{in}/G} \tag{4.2.22}$$

The impedance Y_{in} seen looking into the single resonator is ([3]):

$$S_{11} = \frac{G - Y_{in}}{G + Y_{in}} = \frac{1 - Y_{in}}{1 + Y_{in}/G} \tag{4.2.23}$$

$$Y_{in} = j\omega C + \frac{1}{j\omega L} = j\omega_0 C(\frac{\omega}{\omega_0} - \frac{\omega_0}{\omega}) \tag{4.2.24}$$

Where $\omega_0 = 1/\sqrt{LC}$. For frequency near resonance, $\omega = \omega_0 + \Delta\omega$, where $\Delta\omega \ll \omega_0$, Y_{in} is approximated by ([15]):

$$Y_{in} \approx j\omega_0 C \frac{2\Delta\omega}{\omega_0} \tag{4.2.25}$$

Substituting equation (4.2.23, 4.2.24) in the reflection coefficient S_{11} of the resonator and noting that $Q_e = (\omega_0 C/G)$,we get:

$$S_{11} = (\frac{1 - jQ_e(2\Delta\omega/\omega_0)}{1 + jQ_e(2\Delta\omega/\omega_0)} \tag{4.2.26}$$

When the frequency offset from resonance is [3, 5]: $\Delta\omega_{\pm} = \pm\omega_0/2Q_e$, the phase of S_{11} takes.

4.2.4 Parameters Extraction Process

Fig. (4.6) displays the suggested structure that incorporates a combination of electric and magnetic coupling. The structure is constructed using $RT/Duroid$ 4003c, which has a dielectric permittivity (εr) of 2.2, a substrate thickness (h) of 0.508, and a loss tangent ($tan\delta$) of 0.0009 at a frequency of 10 GHz. The metal via holes have a diameter of $d = 0.5$ mm and are spaced apart by a center-to-center distance of $p = 1$ mm. The mixed connection structure is achieved by etching three slot lines on the top and bottom metal planes. Electric coupling may be regulated by modifying the diameters of the slot lines, whereas magnetic coupling is contingent upon the width of the iris window ([46]). Thus, the simultaneous presence of electric fields results in the formation of a combined coupling ([10]). A simulation was conducted using a two-coupled cavity model, as shown in Fig.(4.6), to analyze the mixed coupling structure. The simulations were conducted using the Ansys HFSS full-wave simulator. The starting dimensions of the TE101-mode-based substrate integrated waveguide (SIW) cavity may be obtained by using the relationships provided in the reference ([11]).

$$lz = \frac{c}{\sqrt{\varepsilon r}} \times \frac{\mu\prime}{2\pi fr} \tag{4.2.27}$$

The effective length of the waveguide, Iz, is determined by the diameter of the metal across, equal to $2r$, and the spacing between adjacent lanes, denoted as p (if p is sufficiently small). The equation (4.2.27) was enhanced in ([10]) by including the d/w ratio since this correlation becomes invalid for a higher diameter value, d.

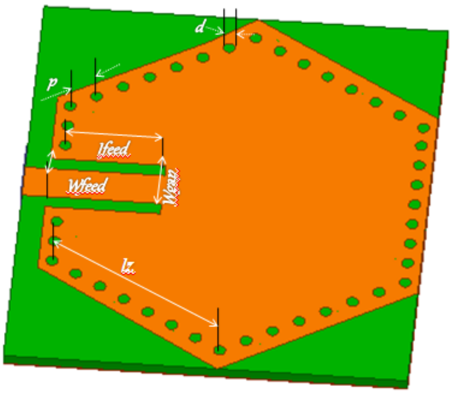

Figure 4.6: First-order combine filter configuration [46].

The simulated S-parameters of the first-order filter.

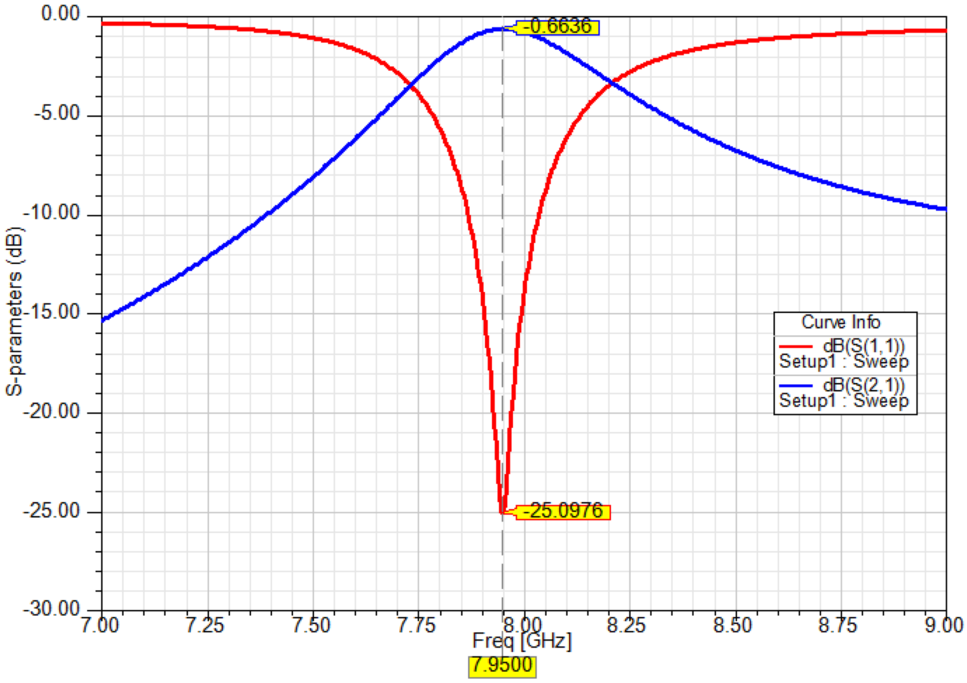

Figure 4.7: Simulated S-parameters of the second-order filter.

4.2.5 Extraction of External Quality Factor

To calculate the external coupling coefficient necessary for the design's group delay technique ([10]), as demonstrated in Fig. (4.8), a coaxial feed line will be employed for introducing the signal into the filter structure. Subsequently, the external quality factor plays a crucial role in defining the distance between the feed line and the filter's initial resonator. This quality factor was derived through an examination of the group delay associated with the reflection coefficient S_{11} ([3]), as illustrated in Fig.(4.9). The methodology for determining the input coupling to a single resonator using the group delay technique entails a thorough analysis of the group delay related to the reflection coefficient S_{11} and the group delays ([12]) is given by.

$$\tau = -(\partial\emptyset)/(\partial\omega) \tag{4.2.28}$$

Note that the group delay has its maximum value at resonance when $\omega = \omega_0$: $\tau_{max} = (\omega_0) = \tau = (4Q_e)/\omega_0$.

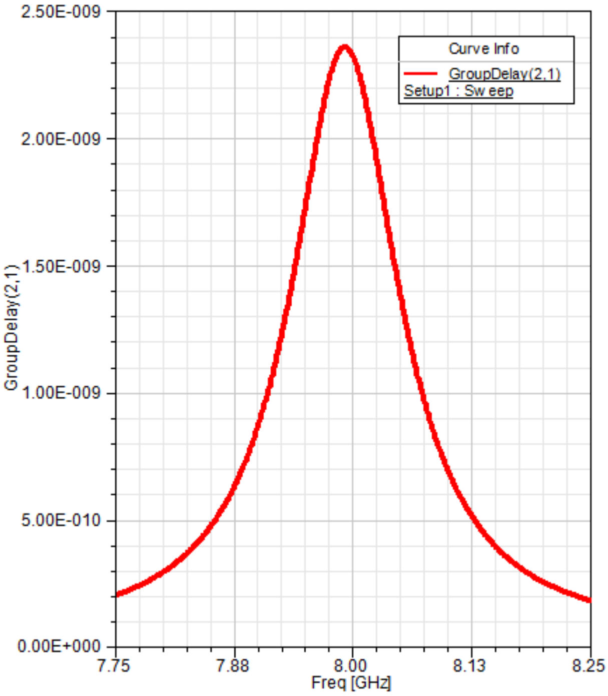

Figure 4.8: Response of the group delay compline filter.

$$Q_e = \frac{\omega_0 \tau_{s_{11}}(\omega 0)}{4} = 29.02302 \tag{4.2.29}$$

$$\tau = \frac{4Q_e}{\omega_{01}} \frac{1}{1 + (2Q_e(\omega - \omega_0)/\omega_0))^2} \tag{4.2.30}$$

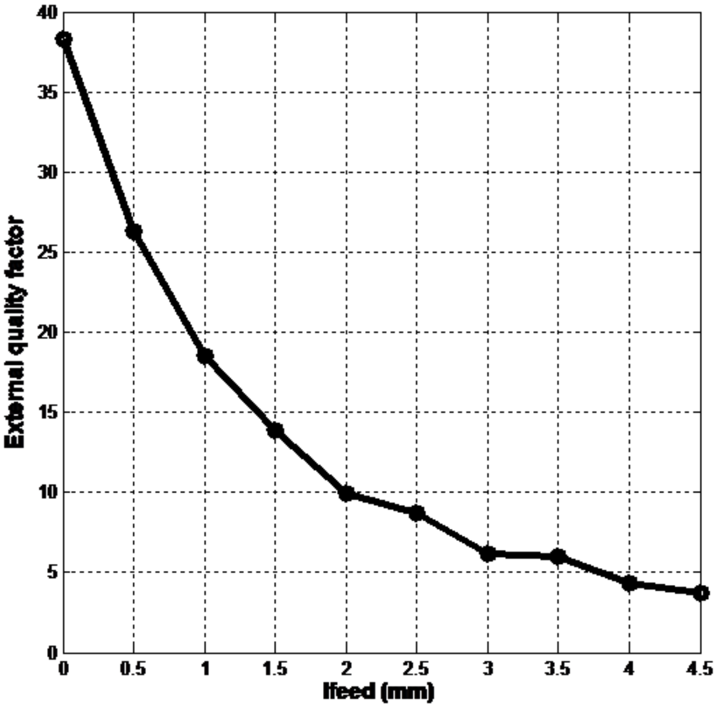

Figure 4.9: External quality factor (ifeed=0.36mm)

4.2.6 Second-Order filter with Mixed Coupling

The setup of the second-order filter utilizing the suggested mixed electric and magnetic coupling arrangement is depicted in the following in Fig.(4.10).

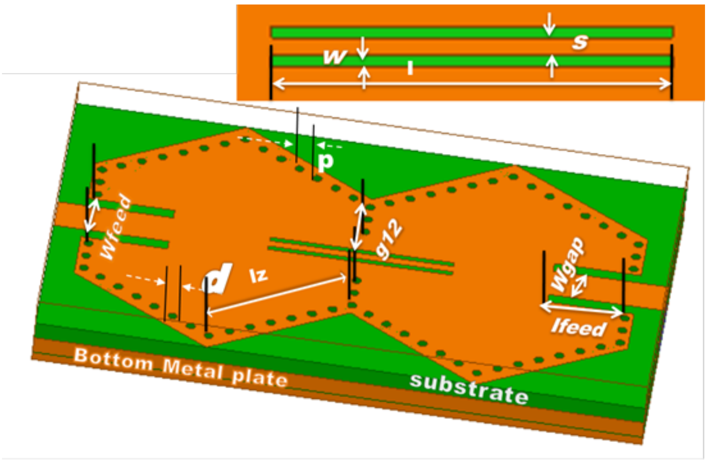

Figure 4.10: The second-order filter with mixed-coupling

Fig.(4.11) ([10]) displays the simulated S-parameters of the second-order filter that incorporates both electric and magnetic coupling.

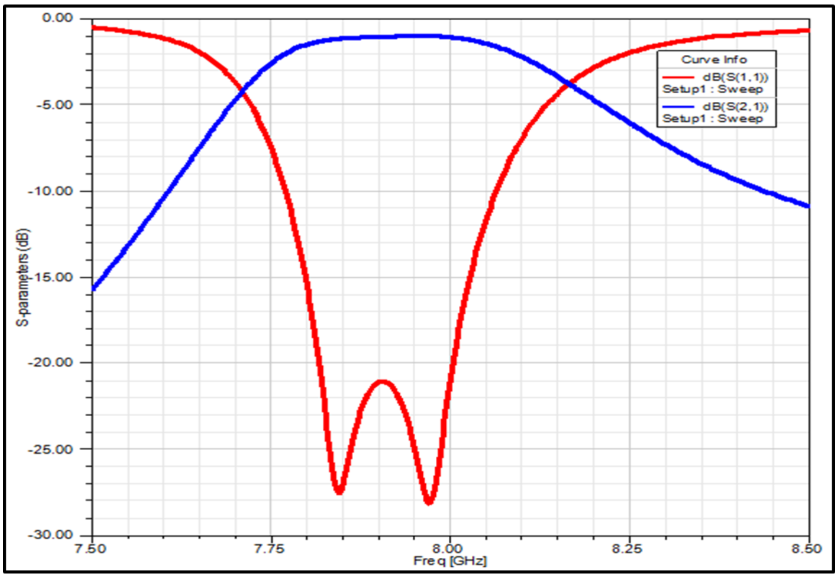

Figure 4.11: S-parameters of the second-order filter against: $Iz = 8.4\ mm,\ g_{12} = 3\ mm,\ l = 13\ mm,\ and\ w = 0.3\ mm,\ s = 0.44$) ([46]).

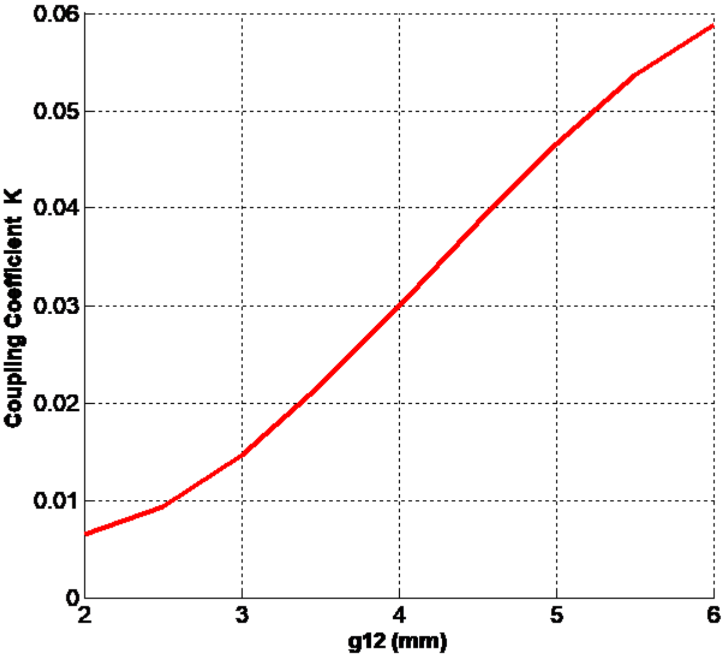

Figure 4.12: .External Coupling coefficient.

The coupling coefficient exhibits a clear relationship with the augmentation in g_{12}, as depicted in Fig.(4.13). The data unequivocally indicates that accurate coupling manipulation is attainable through careful modifications to the dimensions of the aperture lines and the breadth of the iris window.

Concerning Fig.(4.14), it is pertinent to highlight that enlargement in the iris aperture leads to a substantial enhancement of the coupling coefficient k, consequently aligning with the essential requirements for the filter.

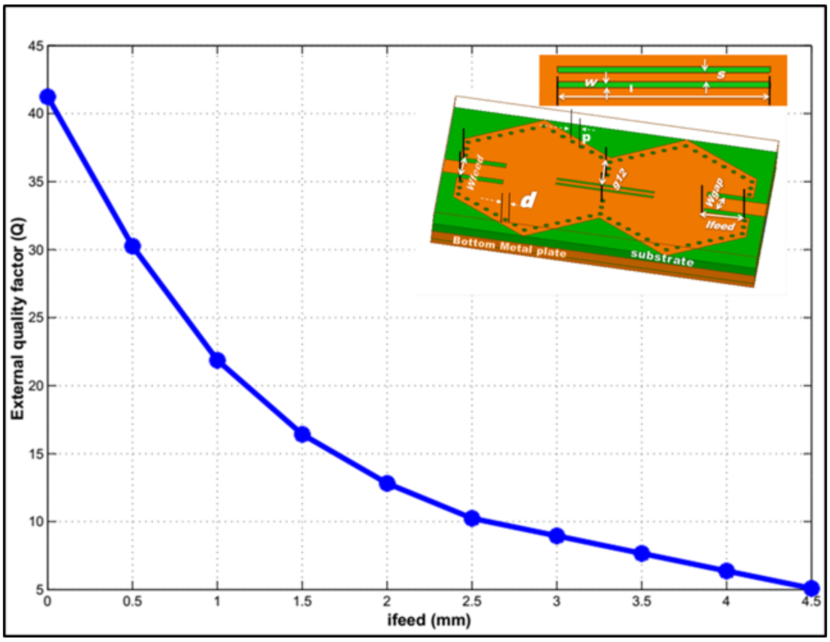

Figure 4.13: External Quality Factor.

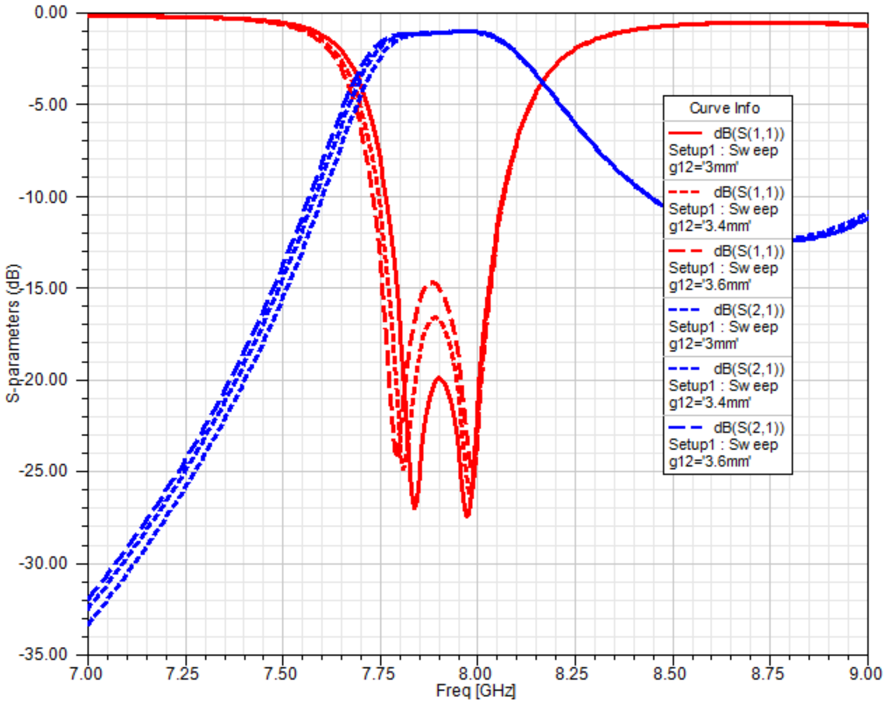

Figure 4.14: Coupling g_{12} coefficients of the coupling structure against.

4.2.7 Third-order cross-coupled filter with mixed-coupling

To assess the efficacy of the proposed combination of electric and magnetic coupling, Tchebychev bandpass filters employing mixed-coupling were constructed and assessed at X-band [11]. The filter, a third-order cross-coupled design centered at 7.95 GHz, exhibits a fractional bandwidth of 8.9% with a 1 dB bandwidth. Initial transmission zeros are located at 8.2 GHz [10]. Fig.(4.15) depicts the layout and interconnection scheme of the third-order cross-coupled generalized Tchebychev bandpass filter. The mixed-coupling approach is applied specifically to the cross-coupling path between resonators 1 and 3, predominantly manifesting as magnetic coupling. Consequently, initial transition zones (TZs) emerge below and above the passband, aligning with the filter's specifications [11].

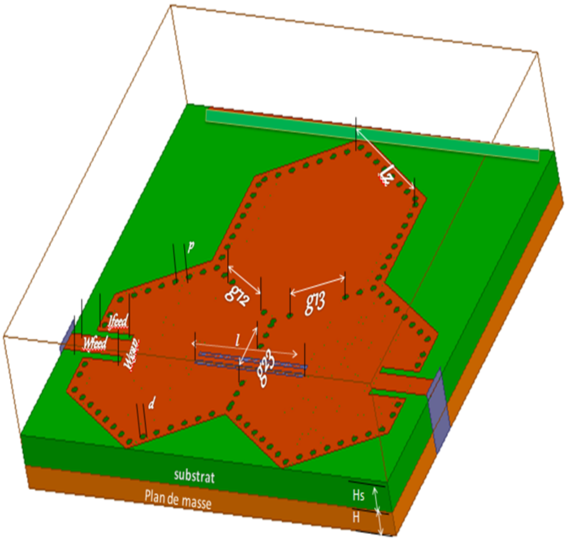

Figure 4.15: The coupling topology of the third-order cross-coupled bandpass filter is being discussed.

Refine. The following design parameters have been obtained for the filter, which has an absolute bandwidth of 450 MHz and a center frequency of $f_0 =$ 7.95 GHz :

$$m_d = \begin{bmatrix} 0.0000 & -0.0346 & 0.0000 & 0.0000 & 0.0000 \\ -0.0346 & 0.0041 & -0.0334 & 0.0166 & 0.0000 \\ 0.0000 & -0.0334 & 0.0159 & -0.0334 & 0.0000 \\ 0.0000 & 0.0166 & 0.0334 & 0.0041 & 0.0381 \\ 0.0000 & 0.0000 & 0.0000 & 0.0381 & 0.0000 \end{bmatrix} \tag{4.2.31}$$

With the optimized filter, $Iz = 8.4\,mm$, $ifeed = 1.5\,mm$, $wfeed = 2.8\,mm$, $wgap = 1.5\ mm$, $d = 0.6\ mm$, $p = 1\ mm$, $w = 0.45\ mm$, $s = 0.5\ mm\ band\ l = 10\ mm$ are its physical dimensions. The analysis outlined in ([2]) is utilized to derive the response of the third-order cross-coupled bandpass filter, as determined by the coupling matrix (4.2.31). Fig.(4.15) illustrates this response. The filter outcomes, as simulated, are contrasted in Fig.(4.16).

Refine. The following design parameters have been obtained for the filter, which has an absolute bandwidth of $450MHz$ and a center frequency of $f_0 = 7.95GHz$:

$$m_d = \begin{bmatrix} 0.0000 & -0.0346 & 0.0000 & 0.0000 & 0.0000 \\ -0.0346 & 0.0041 & -0.0334 & 0.0166 & 0.0000 \\ 0.0000 & -0.0334 & 0.0159 & -0.0334 & 0.0000 \\ 0.0000 & 0.0166 & 0.0334 & 0.0041 & 0.0381 \\ 0.0000 & 0.0000 & 0.0000 & 0.0381 & 0.0000 \end{bmatrix}$$

With the optimized filter, $Iz = 8.4\,mm$, $ifeed = 1.5\,mm$, $wfeed = 2.8\,mm$, $wgap = 1.5\ mm$, $d = 0.6\ mm$, $p = 1\ mm$, $w = 0.45\ mm$, $s = 0.5\ mm$, $and\ l = 10\ mm$

are its physical dimensions. The analysis outlined in ([2]) is utilized to derive the response of the third-order cross-coupled bandpass filter, as determined by the coupling matrix (4.2.31).

Fig.(4.15) illustrates this response. The filter outcomes, as simulated, are contrasted in Fig.(4.16).

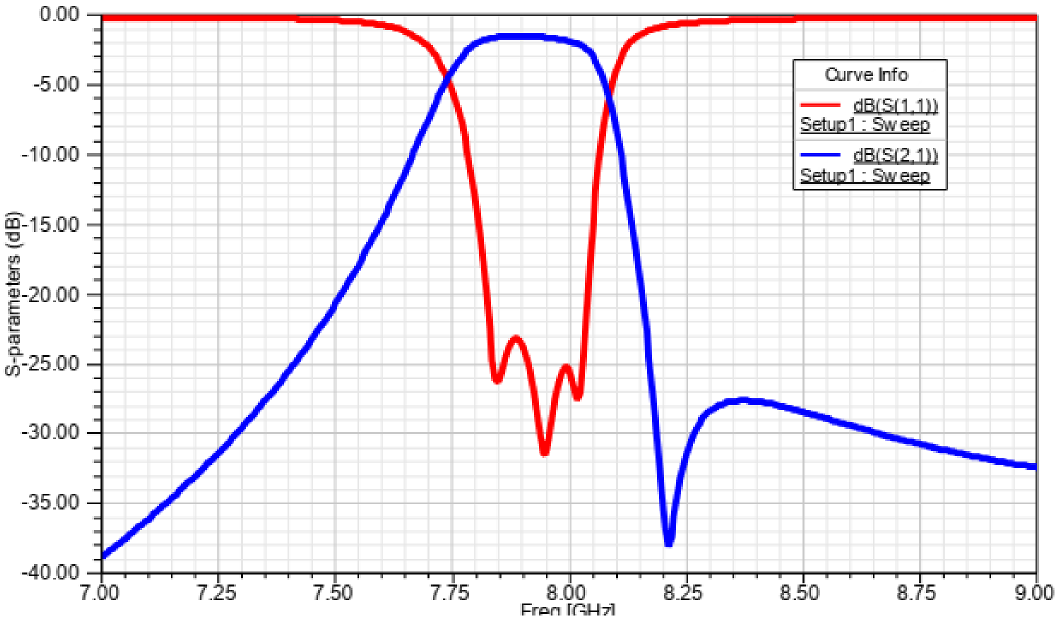

Figure 4.16: The simulated frequency response of the third order cross-coupled band pass filter is analysed.

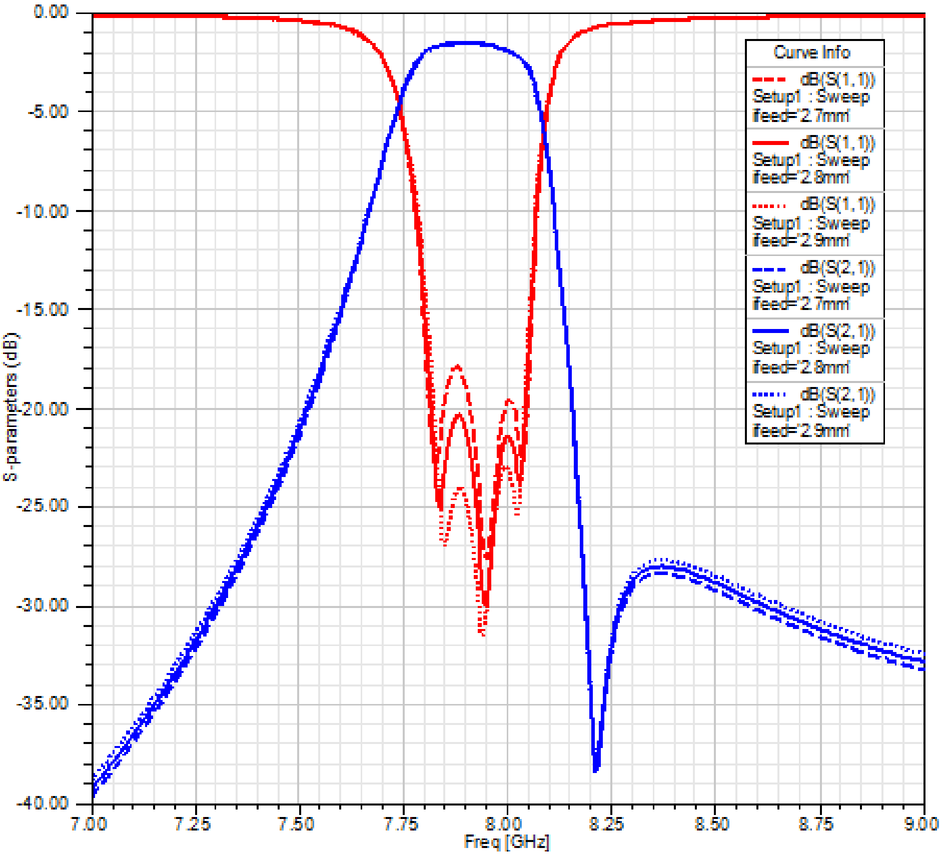

Figure 4.17: The influence of the space ifeed.

Fig.(4.18) displays the results of the $SIW-DGS$ cell simulation with different values from the 'ifeed'. This device uses parameters to monitor the influence of the space 'ifeed' inside the fentes. If the 'ifed' is increased, the upper coupling frequency remains in the mother and the superior coupling frequency will be replaced higher. Consequent, 'ifeed' is the parameter that affects the SIW-DGS proposition: When 'ifeed' is increased, the band passant is increased to the highest point, so that the sign of one passant band is larger.

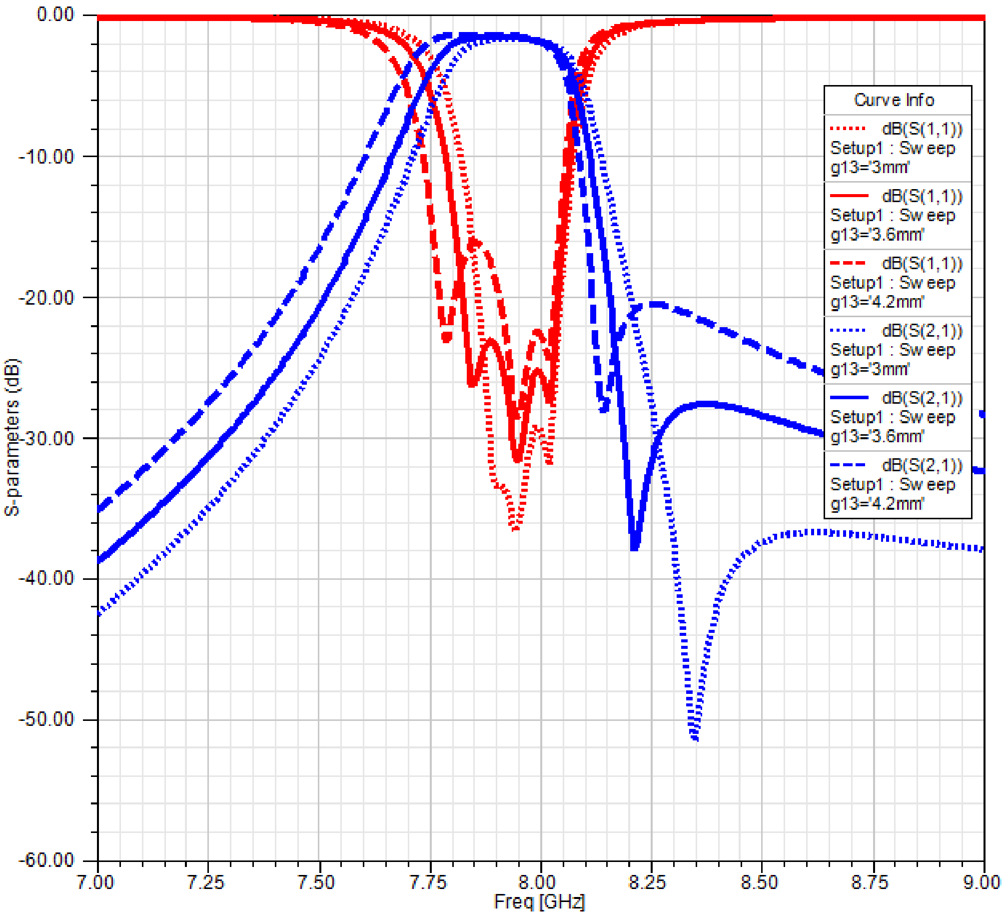

Figure 4.18: The third-order cross-coupled filter's simulated g_{12}.

4.3 Fabrication and Experiment Results

Fig.(4.19) shows the fabricated model of the proposed filter, and Fig.(4.20) shows the total measurement setup. Placed on a pedestal dielectric substrate used is Rogers $RO4003C$ with a height of 0.508 mm, having a relative permittivity (εr) of 3.55 and magnetic loss tangent ($tan\delta$) of 0.0027. are preferred due to their advanced microwave frequency performance and low-cost circuit manufacturing.

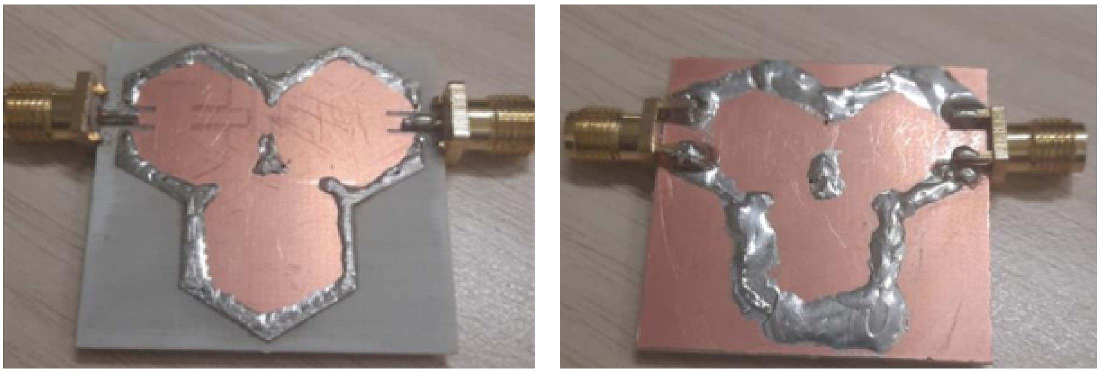

(a) (b)

Figure 4.19: Photographs of fabricated models. (a) top view. (b) Bottom view.

The measured results were plotted against the simulated ones, and they are in good agreement as shown in Fig.(4.19)(a). At $-15\ dB$, in the lower passband and upper passband the measured $S_{11}$is shifted by 0 MHz and 0.1 MHz respectively from the simulated results.

From Fig. (4.20)(b) the simulated and measured transmission coefficients S_{21} show an insertion loss of

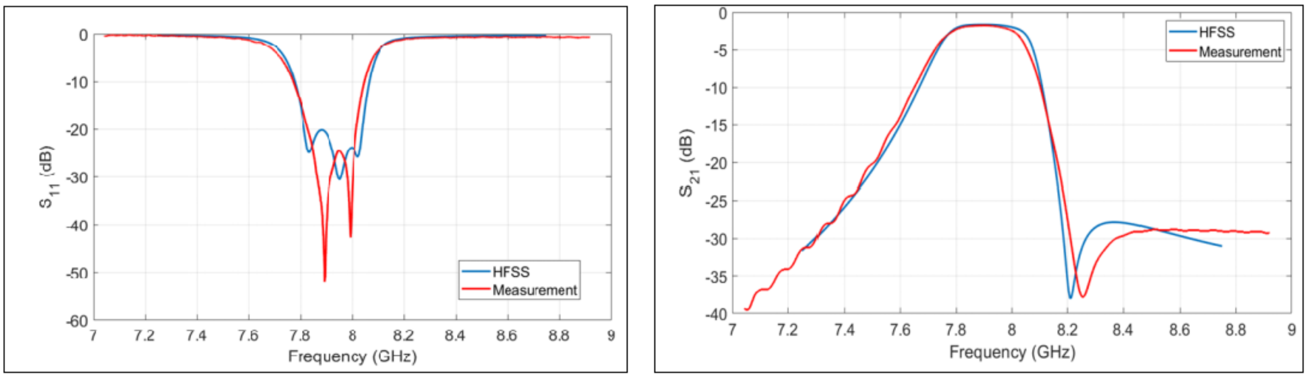

(a) (b)

Figure 4.20: The frequency response of the third-order cross-coupled bandpass filter model.

4.4 Analytical Design and Optimization of Substrate-Integrated Waveguide Cross-Coupled Filters

4.4.1 Trisection Filter Design: Example Two

The filter is constructed by the subsequent requirements that have been established for it:

Center frequency	$f_0 = 8\ GHz$
Bandwidth	$BW = 1.1\ GHz\ (FBW = 10\%)$
Pass band ripple	$LAR = 0.0431\ dB$
Pass band return loss	$RL = 20\ dB$
Stop band rejection level	$> 40\ dB$

Table 4.3: Filter's Target Specifications

A third-order Tchebychev low-pass prototype filter was utilized to test the combined filter designs. This filter had a resonance level of 0.04321 dB. The specification for the low-pass prototype filter specifies $n = 3$ as the preferred filter order. Low-pass filter assembly ([3]) parameters consist of:

g_0	g_1	g_2	g_3	g_4
1	1.0316	1.1474	1.0316	1

The normalized coupling matrix can be leveraged to derive design parameters for dimensional synthesis. The absolute bandwidth and the center frequency, respectively, regulate these parameters. To denormalize the normalized coupling matrix, the subsequent relations ([12]) are utilized:

$$Qes = \frac{g_0 g_1}{FBW}, \quad Q_{es} = \frac{g_n g_{n+1}}{FBW} \tag{4.4.1}$$

$$M_{i,j+1} = \frac{FBW}{\sqrt{g_i g_{i+1}}}, \qquad i = 1, ..., n-1 \tag{4.4.2}$$

$$m_{i,j+j} = \frac{M_{i,j+1}}{FBW}, \quad i = 1, ..., n \tag{4.4.3}$$

The fractional bandwidth is denoted as FBW, whereas the element values of the lowpass prototype filter are represented by g_0, g_1, g_2, g_3, and g_4. The operating frequency of this combined filter is 8 GHz. It is possible to calculate the coupling matrix between the filter and the scaled de-normalized external quality factors utilizing the formulas specified in the reference ([11]).

$$md = \begin{bmatrix} 0 & 0.0410 & 0.0446 \\ 0.0410 & 0 & 0.0410 \\ 0.0446 & 0.0410 & 0 \end{bmatrix} \tag{4.4.4}$$

$$QeS = \frac{g_0 g_1}{FBW} = 23.1995(4.47) \tag{4.4.5}$$

Q_e	M_{12}	M_{23}	M_{13}	Q_s
23.1995	0.0410	0.0410	0.0446	23.1995

Given the circumstances, the symbols 'Q_{es}', 'f_{0i}', and 'M_{ij}' indicate the external quality factor, resonant frequency, and coupling coefficient between adjacent resonators. Furthermore, inductance 'L_0' is determined by the subsequent equations ([19]); capacitance 'C_0' has also been calculated.

$$C_0 = \frac{Q_{eS}}{\omega_0 \times Z} = 157.27\ pF \tag{4.4.6}$$

$$L_0 = \frac{Z}{\omega_0 \times Q_{eS}} = 338.95\ nH \tag{4.4.7}$$

The series impedances Z_{12}, Z_{23}, Z_{34} are:

$$Z_{i,i+1} = \frac{Z}{M_{i,i+1} \times Q_{eS}} \tag{4.4.8}$$

Z_i	L_0, C_0	f_0 (GHz)
$Z = 50\ \Omega$	$L_0 = 338.95\ nH$	8 GHz
$Z_{31} = 48.4684\ \Omega$	$C_0 = 157.27\ pF$	
$Z_{12} = 52.731\ \Omega$		
$Z_{23} = 52.731\ \Omega$		

Table 4.4: Capacitance C_0, Inductance L_0, Impedance Z_i

Fig. (4.21) illustrates the schematic representation of the fourth-order combined filter using mixed-coupling. The parallel capacitance C_0 and the inductance L_0 are the components that define each resonator.

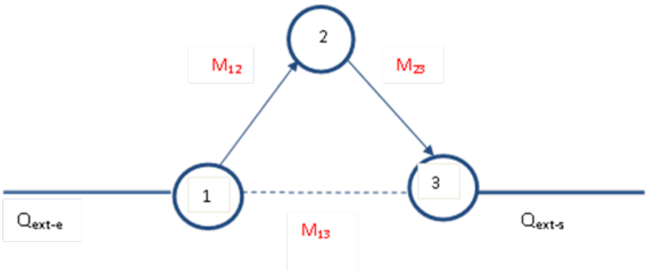

Figure 4.21: third order cross coupled coupling configuration .

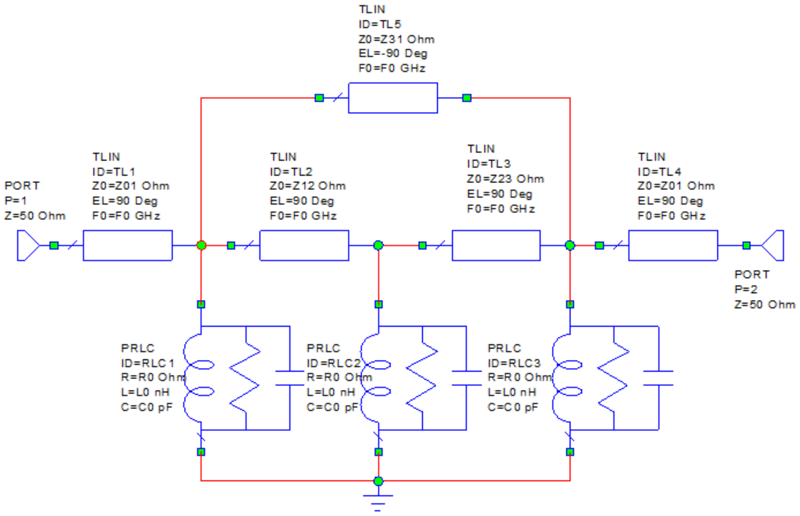

Figure 4.22: Equivalent circuit representation of the I/O resonator with a singular load.

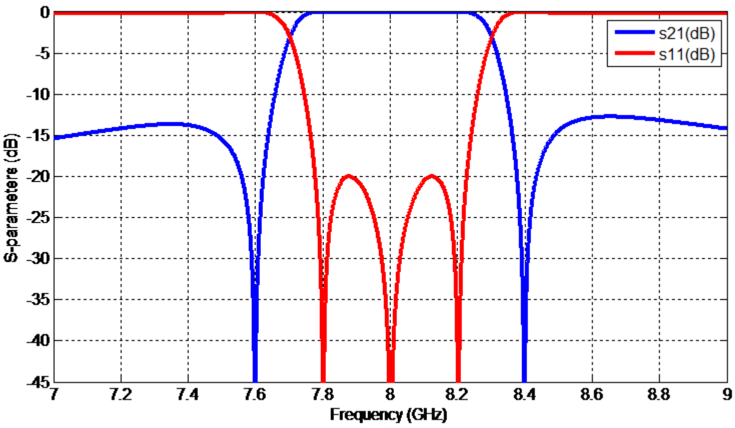

Figure 4.23: The frequency response of third order cross coupled bandpass filter model.

4.4.2 Group Delay Method

Upon coupling to the input feed source, Fig. (4.24) is presented. The conductance represents the input coupling denoted as G. To ascertain the external quality factor, the frequency response of the I/O resonator must be derived from the external quality factor definition specified during the general coupling matrix formulation process. Examining the reflection coefficient, S_{11} occurs at the excitation port of the resonator [[12], [44]].

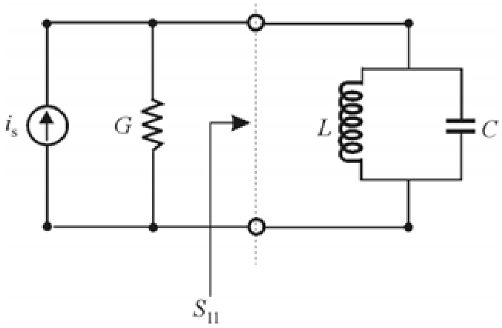

Figure 4.24: Equivalent circuit representation of the I/O resonator with a singular load.

$$S_{11} = \frac{G - Y_{in}}{G + Yin} = \frac{1 - Yin/G}{1 + Yin/G} \tag{4.4.9}$$

The input admittance of the resonator is denoted as Y_{in}.

$$Y_{in} = j\omega C + \frac{1}{j\omega L} = j\omega_0 C(\frac{\omega}{\omega_0} - \frac{\omega_0}{\omega}) \tag{4.4.10}$$

Note that $\omega_0 = 1/\sqrt{LC}$. For frequency near resonance, $\omega = \omega_0 + \Delta\omega$, where $\Delta\omega \ll \omega_0$, Yin is approached by.

$$Y_{in} \approx j\omega_0 C \frac{2\Delta\omega}{\omega_0} \tag{4.4.11}$$

Replacing equation (4.4.9, 4.4.10) in the reflection coefficient S_{11} of the resonator and noticing that $Q_e = \omega C/G$:

$$S_{11} = \frac{1 - jQe(2\Delta\omega/\omega_0)}{1 + jQ_e(2\Delta\omega/\omega_0)}(4.54) \tag{4.4.12}$$

S_{11} demonstrates a phase variation of ± when the frequency offset from resonance is $\Delta\omega = \pm\omega 0/2Q_e$. Deriving the external quality factor from the frequency response of the I/O resonator is essential for constructing the general coupling matrix in accordance with the specified external quality factor. Between the ± marks, the absolute bandwidth is denoted by the S_{11} reflection coefficient at the excitation port of the resonator. From this correlation, one can derive the external quality factor: $Q_e = \omega_0/(\Delta\omega_{(\pm 90)})$

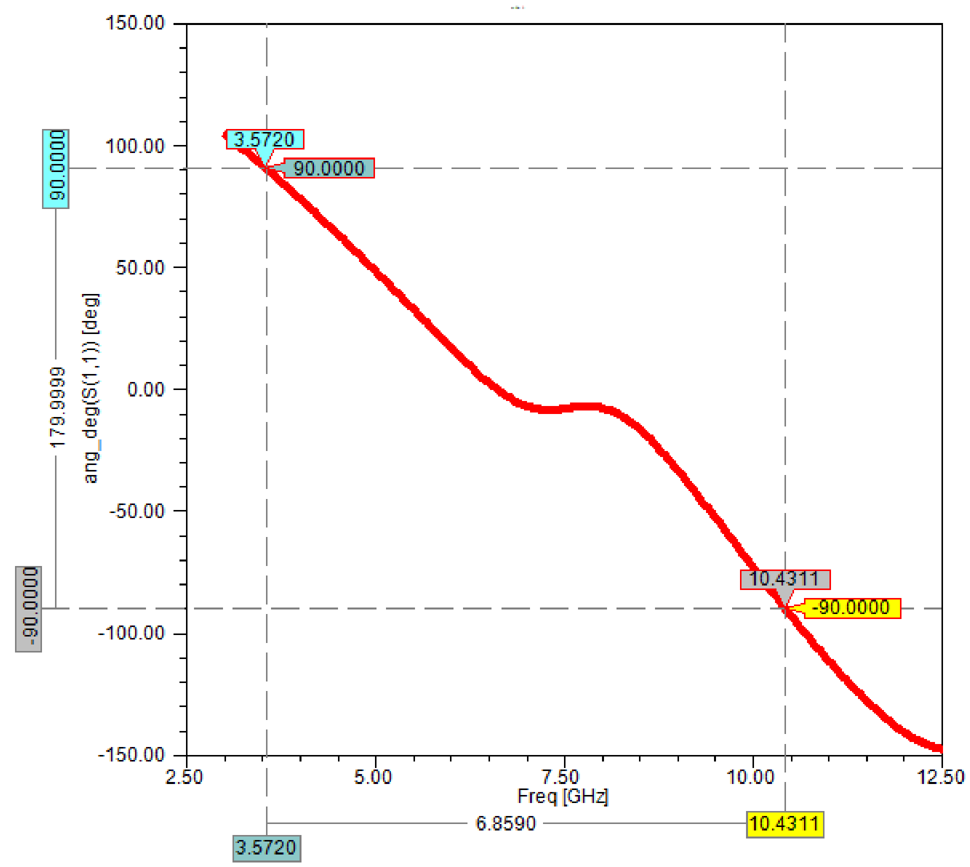

Figure 4.25: The phase response of S_{11} for the circuit is depicted in Fig. (4.25).

$$Q_e = \omega_0/\Delta\omega_{(\pm 90^\circ)} = \frac{8}{0.1898} = 42.14 \tag{4.4.13}$$

A group delay method is utilized to ascertain the input coupling to a solitary resonator through the group delay analysis of the coefficient of reflection S_{11}. This method is predicated on a close examination of the group delay attributes. $\tau = -((\partial\emptyset)/\partial\omega)$ is given by

$$\tau = \frac{4Q_e)/\omega_{01}}{1 + (2Q_e(\omega - \omega_0)/\omega_0)^2} \tag{4.4.14}$$

It is important to observe that the group delay reaches its highest value at resonance when

$$\omega = \omega_0 : \tau_{max} = \tau_{(\omega_0)} = \tau = \frac{4Q_e}{\omega_0} \tag{4.4.15}$$

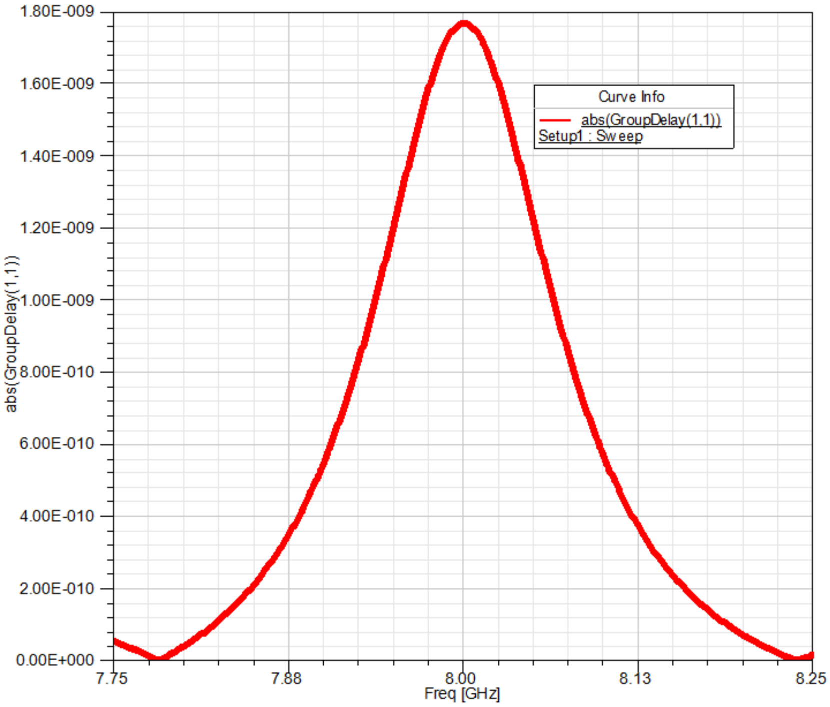

Figure 4.26: Response of the Group Delay compline filter.

$$Q_e = \frac{\omega_0 \tau_{(s_{11})}(\omega_0)}{4} \tag{4.4.16}$$

4.4.3 Parameters Extraction Process

The illustrated structure in Fig. (4.28) integrates electric and magnetic coupling mechanisms. The structure is constructed utilizing a $RO4003C$ substrate, which possesses the subsequent attributes: a substrate thickness (h) of 0.813 mm, a dielectric permittivity (εr) of 3.38, and a loss tangent $(tan\delta)$ of 0.0027 when measured at a frequency of 10 GHz. The center-to-center spacing of the metal via holes is 1 mm.

Each via hole has a diameter of 0.8 mm. The implementation of the mixed-coupling design involves the engraving of three groove lines onto the metal surfaces located at the top and bottom. The width of the iris window determines magnetic coupling as opposed to the manipulation of the slot line's dimensions to modify electric coupling. The phenomenon of mixed-coupling occurs due to the concurrent application of magnetic and electric forces. As illustrated in **Figure 1**, the mixed coupling structure was investigated by simulating a two-coupled cavity model. The Ansys HFSS full-wave simulator was leveraged to conduct the simulations. Using the equations outlined in the reference, one can calculate the initial SIW cavity dimensions, dependent on the TE_{101} mode [44]

$$\begin{cases} \lambda_c = \frac{c}{f\_101\sqrt{\varepsilon r}} = \frac{3\times10^8}{(8\times10^9\sqrt{3.38}} \cong 2mm \\ \frac{d}{\lambda_c} \cong 0.1 \implies d = 0.7mm \\ \frac{d}{P} \cong 0.67mm \implies P = 1.04mm \end{cases} \tag{4.4.17}$$

he leg length and width of W_{eq} measure $5mm$ each in the case of a single SIW square cavity, as determined by calculation in ([11]):

$$f_0 = \frac{c}{2\pi\sqrt{\varepsilon_r}}\sqrt{\frac{1}{a_{eff}^2} + \frac{1}{b_{eff}^2}} \tag{4.4.18}$$

Where

$$a_{eff} = a - \frac{d^2}{0.95p}, b_{eff} = b - \frac{d^2}{0.95p} \tag{4.4.19}$$

The length and width of the TE_{101}-mode-based SIW cavity are denoted as a_{eff} and b_{eff}, respectively, while the velocity of light in a vacuum is represented by c_0

4.4.4 Extraction of External Quality Factor

We utilized HFSS to simulate an SIW cavity resonator with an input signal line to determine the external coupling coefficient in accordance with the group delay method ([30]). The calculated external coupling coefficient utilizing a simulated external coupling structure is illustrated in Fig. (4.27). Compliance with the external coupling regulation by the signal line coupling slot ($feed$) permits the succeeding formula to be used to extract the external quality factor.

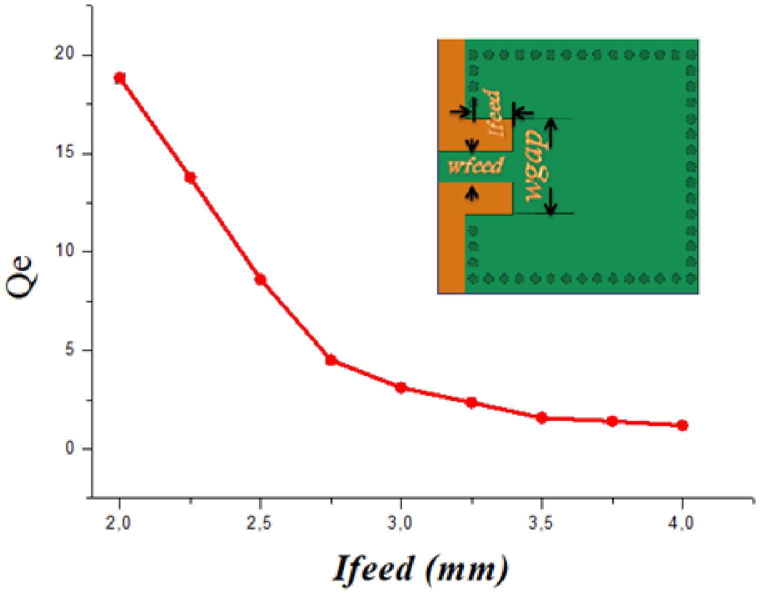

Figure 4.27: The substrate-integrated waveguide (SIW) resonators exhibit an external Q-factor with the following dimensions.

4.4.5 First Order Design Step

Similar to the construction of an air-filled waveguide filter, the design of the filter may be executed through the coupling-matrix method, as elaborated in the preceding sections. The configuration of a SIW filter, represented in Fig. (4.28), is illustrated on a dielectric substrate measuring $0.813mm$ in thickness and having a relative dielectric constant of 3.38. The filter's performance, as simulated by easily accessible electromagnetic modeling tools, is illustrated in Fig. (4.29). The simulation assumes that the substrate has a loss tangent of 0.0027. The formula employs the following variables: (l_{eft}) represents the effective width of the waveguide; $(right)$ denotes the width of SIW; (circumscribed as d), which is equal to $2r$; and (presuming p is sufficiently small) indicates the distance between consecutive vias. d/w ratio in **equation (31)** improves the relationship; otherwise, it becomes nonsensical as the diameter, d.

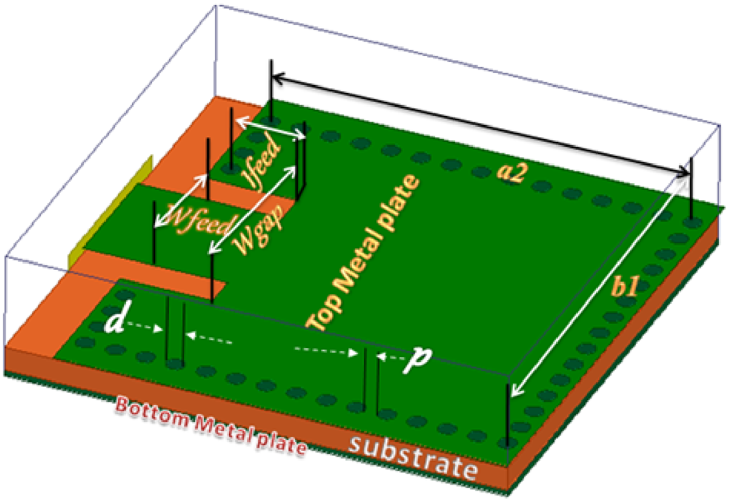

Figure 4.28: First-order combined filter configuration.

The modeled S-parameters of the first-order filter

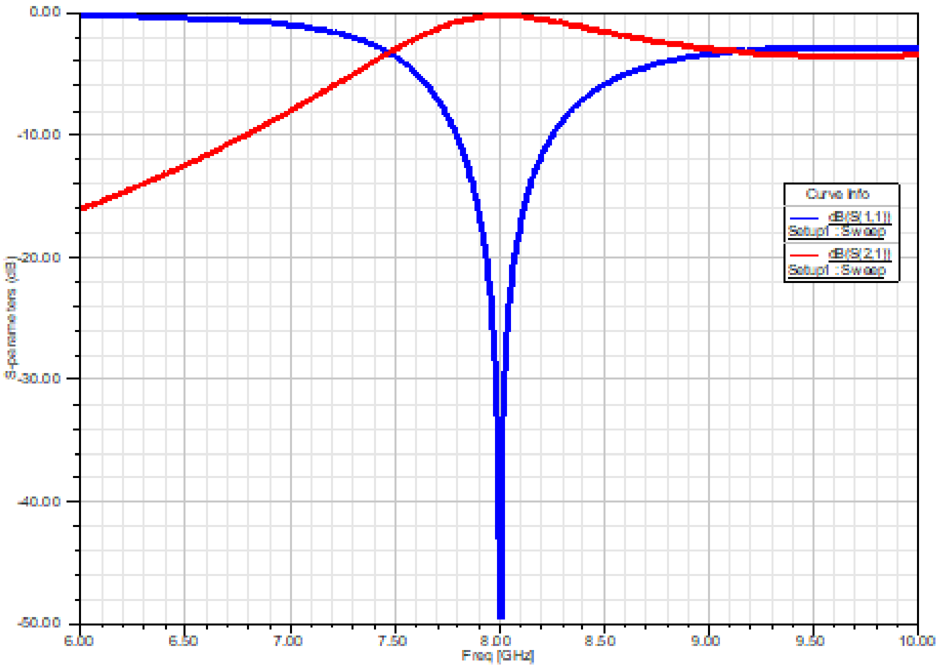

Figure 4.29: Simulated S-parameters of the first-order filter.

4.4.6 Second-Order Design Step

Fig. (4.30) depicts the schematic representation of the second-order filter implemented using the proposed combined electric and magnetic coupling configuration.

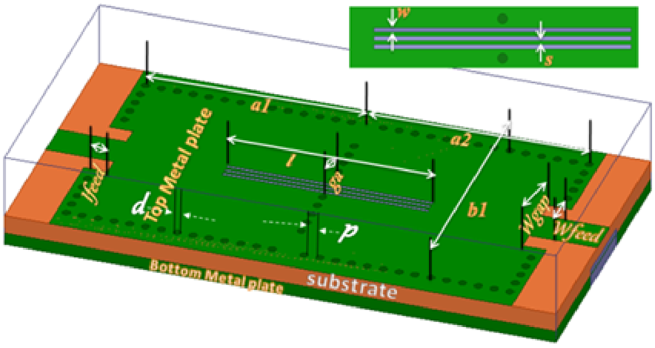

Figure 4.30: In the initial simulation, the configuration of the second-order filter with mixed-coupling.

Fig. (4.31) picture illustrates the outcomes of the S-parameter simulation for the second-order filter, which incorporates both electric and magnetic coupling.

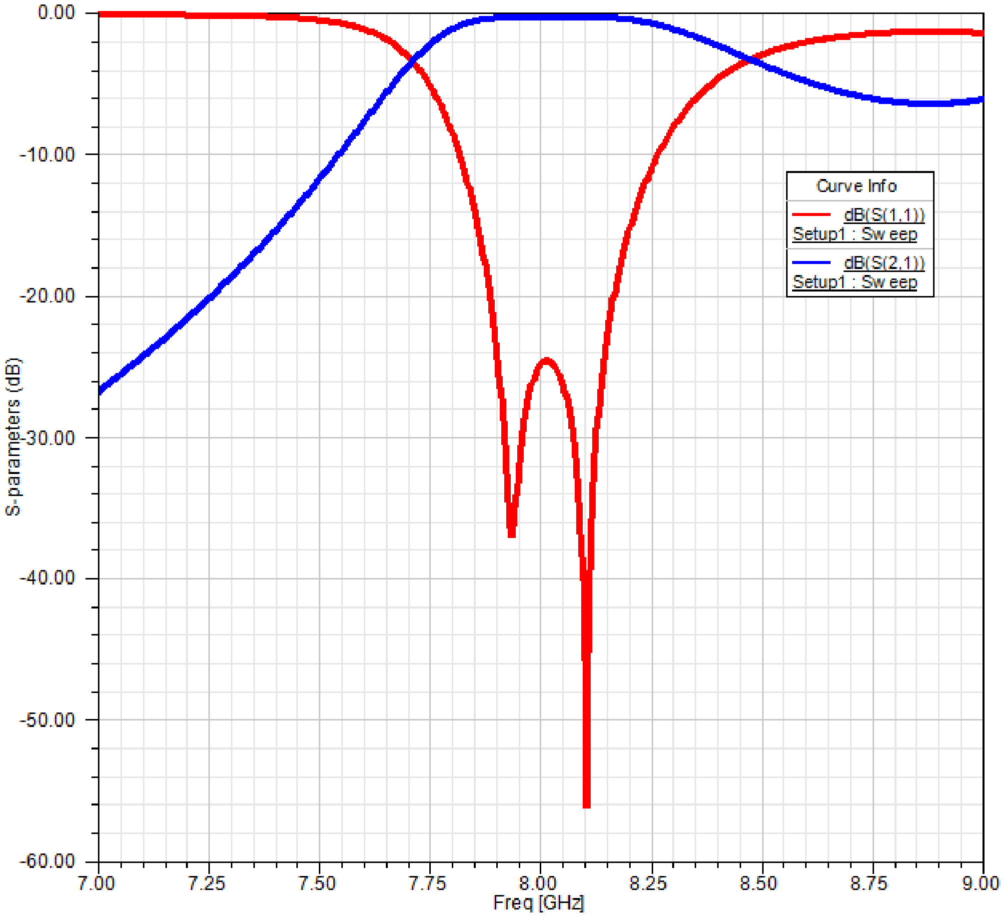

Figure 4.31: Simulated S-parameters of the second-order filter the following dimensions : $a_1 = a_2 = 14.23\ mm,\ b_1 = 14\ mm,\ g_{12} = 5.4\ mm,\ l = 13\ mm,\ and\ w = 0.3\ mm\ ,with\ a\ spacing\ of\ s = 0.44\ mm.$

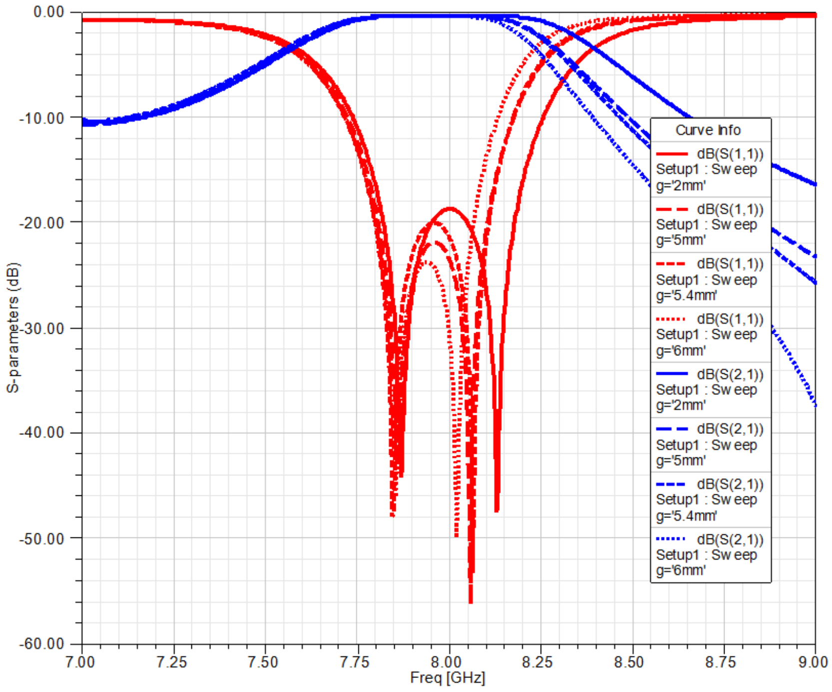

Figure 4.32: Effect coupling the g12 coefficient of the proposed mixed-coupling structure..

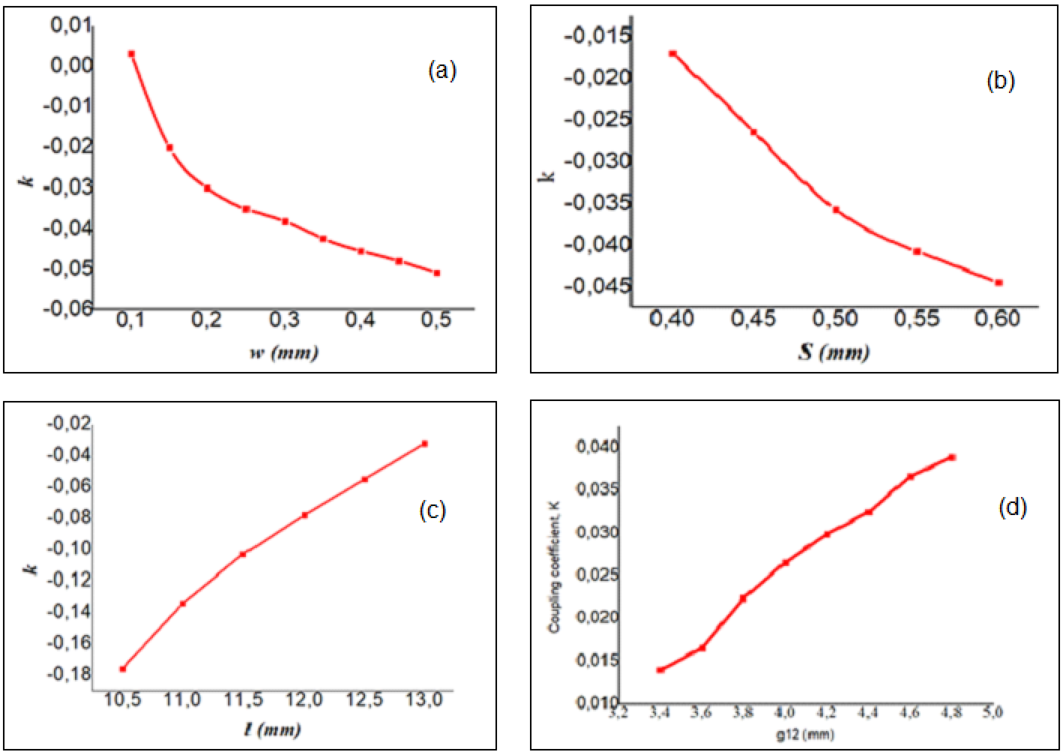

Figure 4.33: Coupling coefficients of the proposed mixed-coupling structure vary with respect to w, s, l, and g_{12}.

As the width (w) and distance (s) of the cavity increase, the external quality factor Q_e, as illustrated in Fig. (4.33) (a) and (b), exhibits a decline. The correlation between the slot lines and the coupling coefficient M_{13} is depicted in Fig. (4.33) (c). A rise in the slot lines corresponds to an enlargement of the iris opening. Based on the information presented in Fig. (4.33) (d), it is apparent that an increase in the coupling strength between the two cavities is proportional to a larger aperture size. A size reduction, conversely, would result in a weakening of the coupling force between the two cavities.

4.4.7 Third-Order Design Step Cross-Coupled Filter With Mixed Coupling

Tchebychev bandpass filters featuring mixed coupling have been carefully designed and evaluated to verify the proposed mixed electric and magnetic coupling structure within the X-band frequency range. At 8 GHz, the third-order cross-coupled filter demonstrates a fractional bandwidth of 8.9%, equivalent to 1 dB. The filter comprises two transmission zeros (Tzs), situated at 7.5 GHz and 8.68 GHz. Fig.(4.34) illustrates the schematic representation and coupling configuration of the third-order cross-coupled generalized Tchebychev bandpass filter. Strategically implemented along the cross-coupling path (between interconnecting resonators 1 and 3), the mixed-coupling architecture is characterized by the predominance of magnetic coupling. As a result, Tzs are established initially both above and below the specified passband in accordance with the filter's parameters.

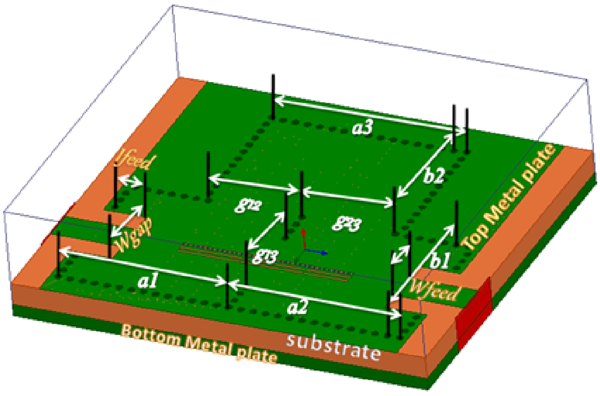

Figure 4.34: Third-order cross-coupled bandpass filter coupling topology.

Table 4.5 presents the design parameters obtained for the filter, which has an absolute bandwidth of $BW = 1.1\ GHz$ and a center frequency of $f_0 = 8\ GHz$.

Geometrical Variable (mm)	Date Range	
	Min (mm)	Max (mm)
$a_1 = a_2$	13.65	14.6
b_1	13.00	13.6
b_2	13.00	14.5
p	00.8	1.4
D	0.35	0.8
ifeed	0.40	3.6
wgap	1.69	2.2
wfeed	05.0	6.0
L	13.00	16.0
W	0.15	0.3
S	0.24	0.5

Table 4.5: Final Dimensions of the Proposed Filter.

$$md = \begin{bmatrix} 0.0397 & -0.0299 & -0.0079 \\ -0.0299 & 0.0422 & -0.0127 \\ -0.0079 & -0.0127 & 0.0087 \end{bmatrix} \tag{4.4.20}$$

The optimized filter is characterized by the subsequent measurements: $a_1 = a_2 = 14.23\ mm,\ b_1 = 14\ mm,\ g12 = 5.4\ mm,\ l = 10\ mm,\ and\ w = 0.3\ mm$, with an s-spacing of 0.44 mm between each element. The synthesized response of the third-order cross-coupled bandpass filter, as indicated in the coupling matrix (4.4.20), is obtained in accordance with the procedure described.

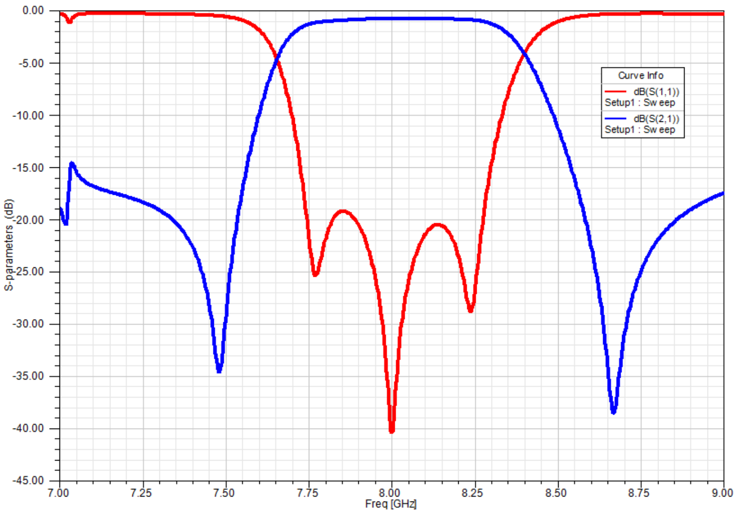

Figure 4.35: Simulation of the frequency response of a third-order cross-coupled bandpass filter.

Fig. (4.36) compares the efficacy of the fourth, third, and second iterations. The effectiveness of the suggested tuning technique is confirmed when the optimized filter response closely resembles the necessary specifications after multiple iterations. The optimal configuration, which has a fractional bandwidth of approximately 1.1 GHz and a center frequency of around 8 GHz, produces an in-band return loss (S_{11}) of less than $-20\ dB$ and a minimum insertion loss (S_{21}) of less than 1.2 dB.

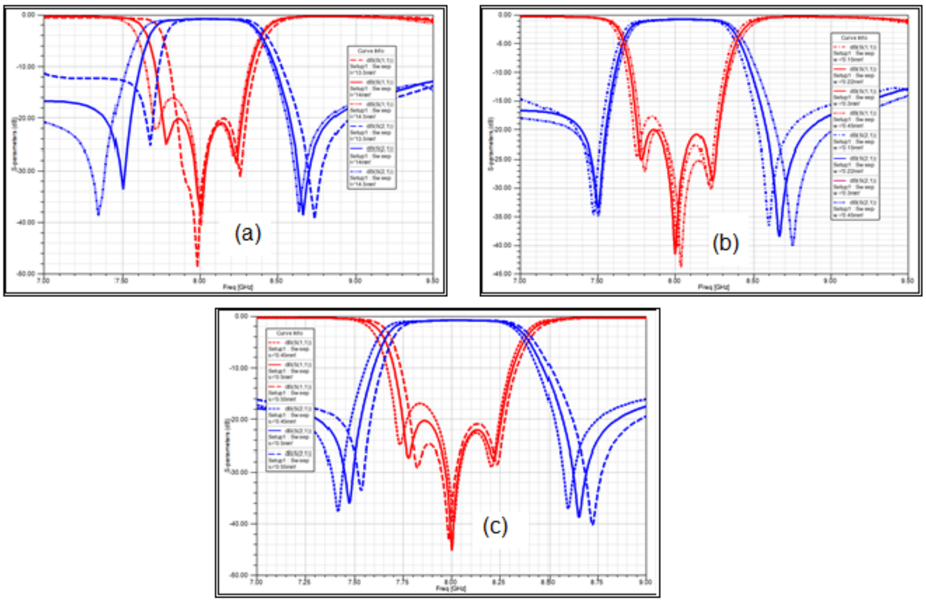

Figure 4.36: The implications of adjusting parameters on the third-order cross-coupled filter.

The specific transition point denoted as fin consistently delineates the boundary of the transition region a cross all scenarios.

The degradation of the electric coupling component of the Meta material Composite (MC) is illustrated in Fig.(4.36) (a) as L increases [44]. With the increase in L, the transmission zeros in the lower stop band shift to lower frequency, leading to a reduction in magnitude. Conversely, the transmission zeros in the upper stop band transition to the passband due to the overall enhancement of the MC [44]. The magnetic coupling feature of the MC becomes more prominent as w increases, as shown in Fig.(4.36) (b). This escalation leads to a decrease [44].

The broader $-3dB$ bandwidth and electric coupling coefficient of 0.08 exhibit superior characteristics compared to current solutions. Furthermore, precise control over the electric and magnetic coupling intensities is achievable by manipulating slot line dimensions and iris window width.

Effective engineering can also produce a TZ that is controllable and located within the upper or lower stop band.

4.5 Cascaded Quadruplet (CQ) Filters (Cross-Coupled filter)

4.5.1 Filter Design

Cascaded Quadruplet (CQ) filters, also known as cross-coupled filters, are a type of advanced filter design used in various high-frequency applications, including microwave and RF systems. These filters improve selectivity and out-of-band rejection by incorporating cross-coupling between non-adjacent resonators. The basic building block of a CQ filter is the quadruplet resonator configuration. This configuration includes four resonators with coupling between adjacent and non-adjacent pairs. This coupling can be designed to create transmission zeros, which enhance filter selectivity by more effectively attenuating unwanted frequency. Fig.(4.37) illustrates the architecture and geometric arrangements of the Substrate Integrated Waveguide (SIW) filter, characterized by direct and indirect couplings.

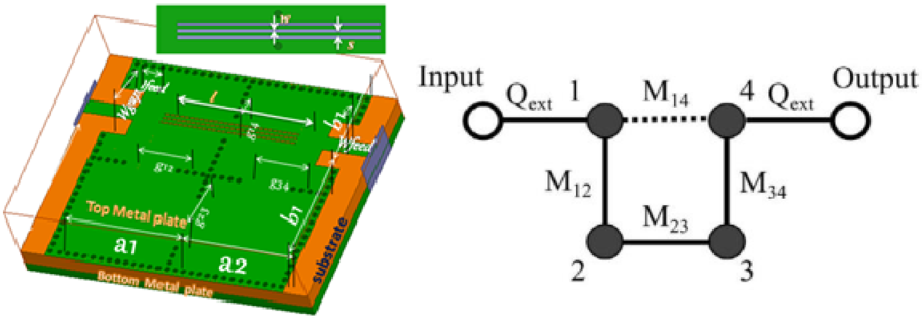

(a) (b)

Figure 4.37: Low-pass prototype and configuration of a SIW four-pole linear phase filter. (a) Configuration of SIW four-pole. (b)Coupling topology of the bandpass filter.

Fig. (4.37) illustrates the structure and geometric configurations of the substrate Integrated Waveguide (SIW) filter, which employs only direct couplings. This filter, depicted in Fig. (4.37) (a), is a four-pole low-pass prototype characterized by the parameters J, J_1, and J_2, representing immittance inverters. These inverters, analogous to a series of coupled microscopic lines, determine the coupling coefficient between resonators through the normalized characteristic impedance. The central immitance inverter, J, is set to the value of '1', leaving g_1 and g_2 (the reactance), and J_1 and J_2 (the inverters) as the adjustable or yet-to-be-determined parameters. Importantly, J_1 is marked as a negative coupling value to differentiate it from J_2 and J, contributing to the creation of finite transmission zeros below and above the desired pass-band. This four-element network aims to establish a connection between the values of its components and the desired filter response.

For the optimized filter outlined in Fig. (4.41), the dimensions are specified as $a_1 = a_2 = 14.23\ mm$, $b_1 = 13.35\ mm$, and $b_2 = 13\ mm$, with inter-element gaps and lengths detailed accordingly. This configuration leads to the presence of four reflection zeros within the band without any transmission zeros outside the band. The filter comprises four adjacent coupling cavities and three coupling post-wall irises, with the input and output ports coupled to the first and last cavities, respectively. Following the normalized Tchebychev low-pass prototype, the reactance and admittance values are determined to calculate the internal coupling coefficients and external quality factors, which in turn allows for the computation of the coupling matrix elements. Dimensional adjustments are then made based on these calculations.

Referencing Cameron's work for synthesizing a generalized Tchebychev filter through a coupling matrix, this adopts a method outlined in another study (referred to as [12]), which specifies component values for a four-element network with an RL of $-20\ dB$ and sets Ω_a at 1.8. This leads to specific g_1, g_2, J_1, and J_2 values. These values facilitate the determination of the coupling coefficient between adjacent elements and the external quality factors in Fig. (4.40), based on the circuit elements of the low-pass prototype filter shown in Fig. (4.38). This method directly correlates the bandpass filter's design parameters and the low-pass prototype's elements.

$$Q_{ei} = Q_{eo} = \frac{g_1}{FBW} \tag{4.5.1}$$

$$M_{2,3} = M_{3,4} = \frac{FBW}{\sqrt{g_2 g_3}} \tag{4.5.2}$$

$$M_{1,2} = \frac{FBW}{\sqrt{g_1 g_2}} \tag{4.5.3}$$

$$M_{1,4} = \frac{FBW \times J_1}{g_1} \tag{4.5.4}$$

The fraction bandwidth (FBW) is a critical parameter in this context. We select a center frequency of 8 GHz, aiming for a return loss of $-20\ dB$.

Additionally, we assume a bandwidth with a 10% ripple. The design and performance characteristics of the filter are further detailed through the generalized coupling matrix, as outlined in reference [3].

$$M_d = \begin{bmatrix} 0.0000 & 0.0497 & 00000 & 00000 & 00000 & 00000 \\ 0.0497 & 0.0003 & 0.0373 & 0000 & 0.0208 & 00000 \\ 00000 & 0.0373 & 0.0027 & -0.0536 & 0.0036 & 00000 \\ 00000 & 00000 & -0.0536 & -0.0042 & -0.0739 & 00000 \\ 00000 & -0.0208 & 0.0036 & -0.0739 & 0.0001 & 0.0812 \\ 00000 & 00000 & 00000 & 00000 & 0.0812 & 00000 \end{bmatrix} \tag{4.5.5}$$

The optimal circuit behavior for this coupling configuration is illustrated in Fig. (4.37)

Q_e	M_{12}	M_{23}	M_{34}	M_{41}	Q_s
9.5974	0.0856	0.0856	0.0856	0.0195	9.5974

The quality factor ($Q_{(e,s)}$) of the input and output ports, along with the resonant frequency (f_{0i}) of each resonator, plays a crucial role in the system's performance. The coupling coefficient ($Mijs$) between two adjacent resonators is also a critical parameter. The capacitance (C_0) and the inductance (L_0) values have been determined using specific equations.

$$C_0 = \frac{Q_{eS}}{\omega_0 \times Z}\, pF \tag{4.5.6}$$

$$L_0 = \frac{Z}{\omega_0 \times Q_{eS}} \quad nH((4.69) \tag{4.5.7}$$

$$RQ = Z\frac{Qu}{Qe} \quad (ohm)(4.70) \tag{4.5.8}$$

The characteristic impedance is a crucial parameter in the performance and design of quarter-wavelength transmission lines, which transfer electrical signals and power without reflection. It ensures effective matching of load to source, minimizes signal loss, and influences line efficiency and signal integrity across various frequency.

$$Z_{12} = Z_{34} = \frac{Z}{M_{12} \times Q_{eS}}\, (ohm) \tag{4.5.9}$$

$$Z_{23} = \frac{Z}{M23 \times QeS}\, (ohm) \tag{4.5.10}$$

$$Z_{41} = \frac{Z}{|M41| \times QeS}\, (ohm) \tag{4.5.11}$$

Z_i	L_0, C_0	$f_0\ (GHz)$
$Z = 50\ \Omega$	$L_0 = 346.08\ nH$	$8\ GHz$
$Z_{01} = 50\ \Omega$	$C_0 = 198.94\ pF$	
$Z_{12} = Z_{34} = 60.8598\ \Omega$		
$Z_{23} = 54.451\ \ \Omega$		
$Z_{14} = 0.0220\ \Omega$		

Table 4.6: Capacitance C_0, Inductance L_0, Impedance Zi

The representation of the fourth-order combined filter featuring mixed-coupling is depicted in Fig. (4.37) (a). This schematic illustrates that a parallel capacitance configuration defines each resonator within the circuit, denoted as C_0, and an inductance labeled L_0.

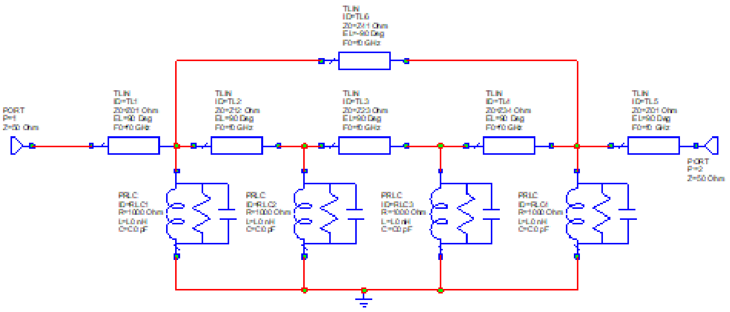

Figure 4.38: Equivalent circuit of lumped element for microwave BPF in AWR.

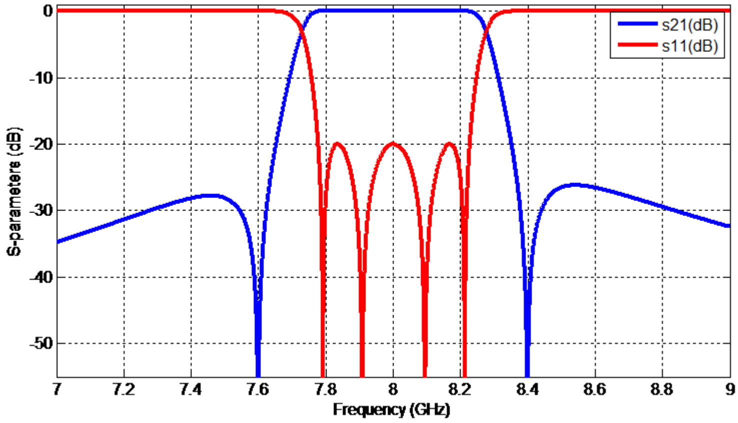

Figure 4.39: S-parameters obtained from the coupling matrix.

The external quality factor of the filter, denoted as Q_{ext}, was determined utilizing equation (4.4.13). This involved exciting a single Substrate Integrated Waveguide (SIW) cavity resonator via a 50 Ω microscopic line connected through a coupling slot. The determination of the external quality factor, Q_e, is primarily influenced by the dimensions of the coupling slot, specifically its width ($wgap$) and length ($lfeed$). The value of Q_e was derived from simulation results, following the application of Equation (4.5.12).

$$Qe = \omega_0 / \Delta\omega_{(\pm 90^0)} \tag{4.5.12}$$

In this section, we describe the characteristics of the cavity resonator, where ω_0 represents the resonant frequency and ($\Delta\omega_{0\pm90}$) denotes the frequency bandwidth achieved through a phase shift of ±90° relative to the absolute phase at ω_0. Fig. (4.25) illustrates the relationship between the external quality factor (Q_e) and the resonator's physical dimensions, specifically the feed length (lfeed) and the gap width ($wgap$). The external quality factor, Q_e, varies with lfeed, and for clarity, we present three distinct curves corresponding to different $wgap$ values. It has been noted that $Q_e$exhibits a gradual decline as lfeed is extended. Conversely, the impact of increasing wgap on Q_e is more subdued, indicating a slower rate of decrease.

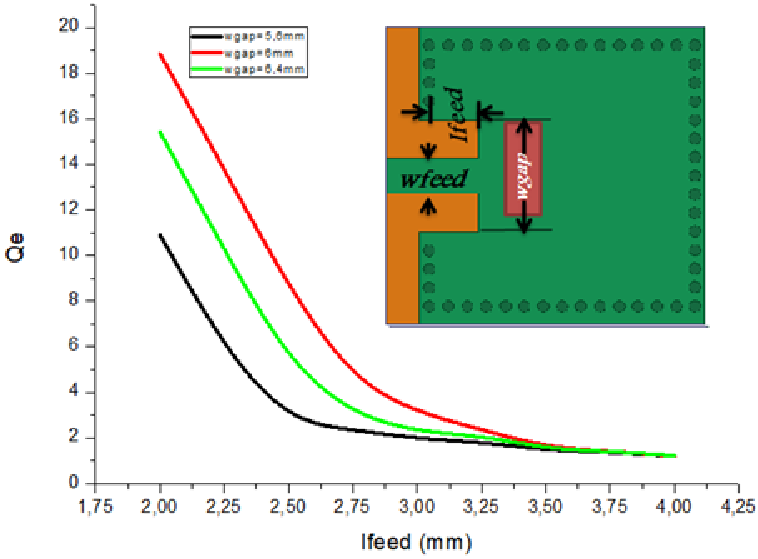

Figure 4.40: External quality factor.

Geometrical	Data range		
Variable (mm)	Min (mm)		Max (mm)
$a_1 = a_2$	cccheight13.65	14.23	14.60
b_1	13	13.15	13.6
b_2	13	13.6	14.5
P	0.8	1	1.4
D	0.35	0.6	0.8
ifeed	0.4	2.3	3.6
wgap	1.69	1.88	2.2
wfeed	5	5.6	6
L	13	14.5	16
W	0.15	0.23	0.3
S	0.3	0.4	0.5

Table 4.7: Dimensions of the Proposed Filters

Fig. (4.41) shows the equivalent circuit's response after transforming the low-pass prototype into a bandpass filter, with 8 GHz as the central frequency, an 800 MHz bandwidth, and a 20 dB return loss level.

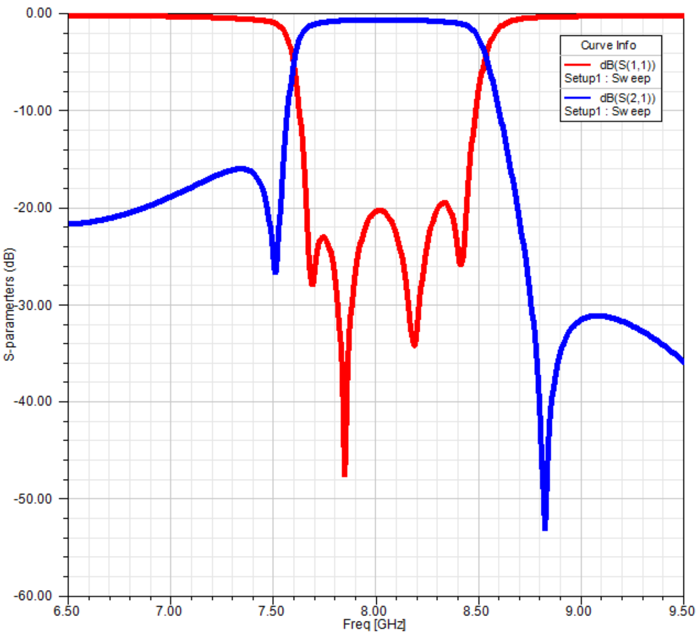

Figure 4.41: EM-simulated responses of the filter with HFSS.

4.5.2 SIW Variation Effects Structure

4.5.2.1 Via hole diameter variation effect

The curves presented in Fig. (4.42) elucidate the impact of varying the diameter of via holes on the observed phenomena, contrasting with the effects illustrated in Fig. (4.37) (a). This analysis reveals that changes in the via hole diameter have an inverse relationship with the outcomes associated with variations in the width of the p. Enlarging the via hole diameter results in a downward shift in the center frequency, while reducing the diameter leads to an upward frequency shift. Consequently, it can be inferred that the resonant frequency is influenced by both the via hole diameter and the width of the p.

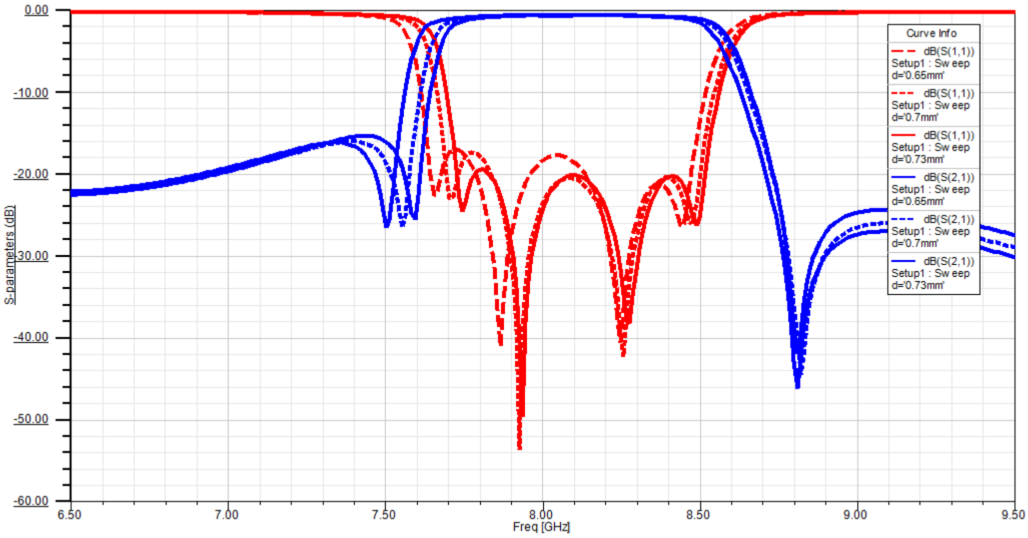

Figure 4.42: Variation of the diameter of via (d) the proposed bandpass filter SIW.

4.5.2.2 SIW Variation Effects Structure DGS

The curves depicted in Figure 4.43 illustrate the changes in the diameter of the Defected Ground Structure (DGS). These changes are a result of variations in the parameters: length (l), width (w), spacing (s), and gap (g), as shown in the same figure. A Transmission Zero (TZ) emerges due to the mixed coupling between two adjacent cavities, positioned above the passband when the Main Coupling (MC) is less than the External Coupling (EC) and below the passband when MC exceeds EC. Furthermore, the position of the TZ shifts towards the right as the ratio of MC to EC decreases, and conversely, it shifts towards the left as this ratio increases.

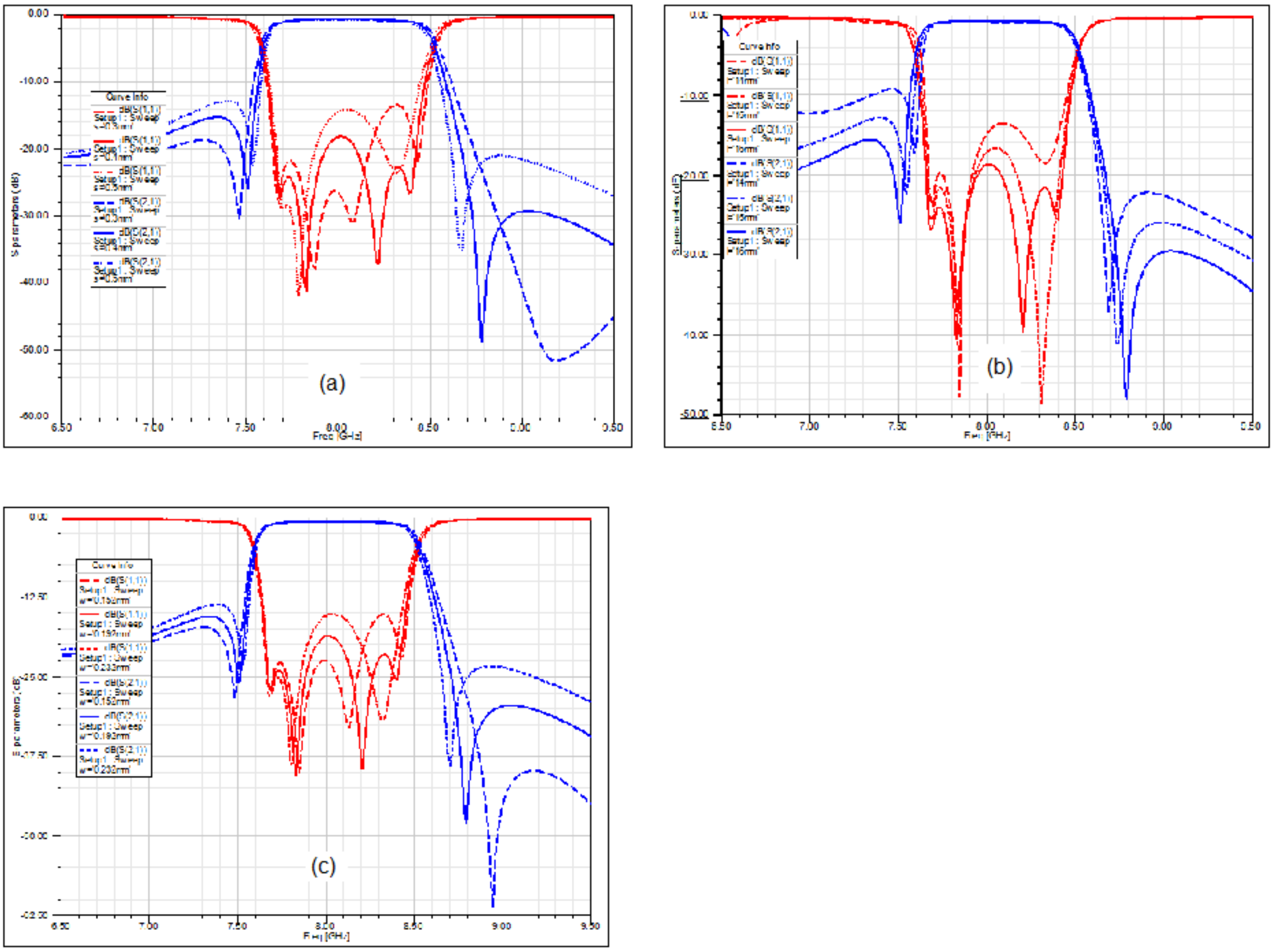

Figure 4.43: Variation of the diameter DGS the variation in the parameters (a) variation in the parameters (W) (b) variation in the parameters (S).(c) variation in the parameters (L).

The Transmission Zeros (TZs) are situated at $8.85GHz$ within the higher frequency band and $7.5GHz$ in the lower frequency band. Leveraging the principles of network synthesis derived from coupling theory, as outlined in reference [11], the resulting normalized coupling matrix is established and detailed in reference [3].

$$m = \begin{bmatrix} 0 & 0.9313 & 0 & 0 & 0 & 0 \\ 0.9313 & 0 & 0.9115 & 0 & 0 & 0 \\ 0 & 0.9115 & 0 & 0.6985 & 0 & 0 \\ 0 & 0 & 0.6985 & 0 & 0.9115 & 0 \\ 0 & 0 & 0 & 0.9115 & 0 & 0.9331 \\ 0 & 0 & 0 & 0 & 0.9331 & 0 \end{bmatrix} \tag{4.5.13}$$

Following simulation and optimization, TABLE 4.8 details the geometric configurations of the filters. However, specific applications necessitate precise attenuation levels in the stop band, necessitating flexible control over the Transmission Zeros (TZs). Their distance from the pass band significantly influences the width of the stop band resulting in a wider stop band when far apart and a narrower one when closer. In a cascaded quadruple filter with a single stage, the determinants of the coupling coefficient include the number of stages, the negative coupling coefficient, and the length of the Coplanar Waveguide (CPW) line. Therefore, by adjusting the CPW line, one can precisely position the TZs. Fig. (4.43) illustrates the correlation between the TZs' positioning and the CPW line's length.

Reference	Order	Electric Coupling Coefficient	3-dB Bandwidth
[7]	3	0.06	1.8%
[8]	4	0.04	4.88%
[40]	3	0.06	5.8%
[13]	4	0.07	6%
[44]	4	0.08	12.1%
This Work	3	3	10%

Table 4.8: Comparisons With Existing Electric Coupling Structures in SIW

4.6 Conclusion

This chapter delves into the domain of Analytical and Synthesis filter Design Substrate Integrated Waveguide (SIW) technology, highlighting its emergence as a compelling alternative to traditional rectangular waveguide. Characterized by its high-quality factor, low loss rates, and straightforward manufacturing process, SIW technology meets the critical demands of advancements in wireless communication systems. It is an efficient approach for crafting high-performance microwave filters, an essential component in designing superior wireless communication infrastructure. Extensive research has been conducted to explore the potential of superconduction front-end planar devices within the Ka frequency band. This exploration aims to unlock additional operating frequency, catering to future wireless communications' escalating needs. Moreover, implementing a planar SIW structure, which incorporates electric and magnetic coupling on a singular layer substrate, represents a significant stride towards innovative wireless communication solutions.

General Conclusion

Mobile communication has become an indispensable facet of modern life, driving a relentless pursuit of enhanced connectivity and reliability. Amidst this demand, mobile communication providers face escalating pressure to elevate the standards of their networks. At the heart of these networks lies the pivotal base station, serving as the linchpin connecting mobile devices to the expansive communication infrastructure.

Within this intricate ecosystem, microwave filters emerge as indispensable guardians, meticulously sieving through signals to ensure clarity amidst the noise. Their role in minimizing interference, enhancing signal quality, and optimizing performance is paramount. Yet, the quest for superior filters becomes imperative as the clamor for swifter, more dependable services intensifies.

Thus, this research project embarks on a voyage to explore and evaluate a myriad of synthesis, dimensioning, and optimization techniques tailored for microwave filters within mobile communication base stations. By scrutinizing recent advancements and breakthroughs, the endeavor aims to pioneer high-performance filters that augment the efficacy of mobile communication systems.

Chapter 1 establishes the foundational knowledge necessary for understanding microwave filters. It covers the basics of filter networks, including polynomial properties, transmission, and reflection coefficients. Exploring frequency responses, characteristic functions, and coupling matrices sets the stage for more complex filter designs. The theoretical groundwork laid in this chapter is crucial for comprehending the advanced topics discussed later.

Chapter 2 delves into the specifics of rectangular bandpass waveguide filters. It

addresses propagation modes, waveguide resonators, and discontinuities within the structure. The chapter highlights the design process of bandpass filters, providing examples of direct coupling and pseudo-elliptic filters. These practical examples underscore the application of theoretical principles in real-world filter designs, emphasizing the importance of accurate synthesis and implementation.
Chapter 3 focuses on the development and optimization techniques for compact microwave filters. The coupling matrix theory is revisited and expanded upon, detailing the physical realization of coupling matrices in bandpass filter designs. The chapter presents detailed design specifications, frequency responses, and equivalent circuits for various filter models, including microscopic filters. The fabrication and experimental results validate the theoretical models, showcasing the effectiveness of the proposed designs.

Chapter 4 addresses the analytical design and optimization of SIW filters. It covers hexagonal cavities, trisection, and cross-coupled filters, employing group delay analysis and quality factor extraction methods. The chapter includes fabrication and experimental results, highlighting the practical viability of the SIW filter designs. Additionally, it discusses the effects of structural variations, such as via hole diameter and defected ground structures (DGS), on filter performance. Overall Contributions and Future Directions This research thoroughly investigates various aspects of microwave filter design, from theoretical principles to practical implementations. The methodologies and examples presented serve as valuable references for future work in this field. Future research could explore further optimization techniques, integrating advanced materials, and developing more compact and efficient filter designs to meet the evolving demands of modern communication systems. By systematically addressing the challenges and innovations in microwave filter design, this work contributes significantly to advancing microwave engineering, paving the way for more efficient and effective filtering solutions in diverse applications.

Bibliography

[1] Atia. A. E. and A. E. Williams, "Narrow-bandpass waveguide filters," IEEE Transactions on Microwave Theory and Techniques, vol. 20, no. 4, pp. 258-265, 1972.

[2] Azad, Amit Ranjan and Jhariya, Dharmendra Kumar and Mohan, Akhilesh, "Substrate-integrated waveguide cross-coupled filters with mixed electric and magnetic coupling structure". International Journal of Microwave and Wireless Technologies, (2018), Volume (10), no. 8, pp. 896-903.

[3] Boria, Vicente. E. and Gimeno, Benito, "Waveguide filters for satellites". IEEE Microwave Magazine, (2007). Volume (8).

[3] Cameron, Richard. J and Kudsia, Chandra M and Mansour, Raafat R, "Microwave filters for communication systems: fundamentals, design, and applications". (2018).

[4] Cameron, Richard. J, "General coupling matrix synthesis methods for Chebyshev filtering functions". IEEE transactions on microwave theory and techniques, (1999). Volume 47.

[5] Challal, Mouloud and Hocine, Kenza and Mermoul, Ali, "A novel design of compact dual-band bandpass filter for wireless communication systems". Wireless Personal Communications, (2019). Volume (109).

[6] Chen, H., Jianqing, Q. and Liu, F. "Modeling Emergence of Network Radar Countermeasure System". Journal of System Simulation, (2021). Volume (27).

[7] Chen. X. P, Hong. W, Cui. T, Hao. Z, and Wu. K., "Substrate integrated waveguide elliptic filter with transmission line inserted inverter," Electron.Lett., vol. 41, no. 15, pp. 851-852, Jul. 2005.

[8] Chen. X.P, and Wu. K, "Substrate integrated waveguide cross-coupled filter with negative coupling structure," IEEE Trans. Microw. Theory Techn., vol. 58, no. 1, pp. 142-149, Jan. 2006.

[9] Damou. M., Chetioui. M. , Boudkhil. A. and Bouhmidi. R. "Analytical Design and Optimization of Multi-Ports Combline Filter using Extraction of Admittance Technique". International Journal of Microwave & Optical Technology, (2022). Volume (17). (**remplacer mehdi par damou1**)

[10] Damou. M., Chetioui. M., Boudkhil. A., Gouni. S., Bouhmidi. R. and Bouras. B. , "Coupled Rectangular Waveguide Resonator Filter Using 3D-HFSS Based Admittance Extraction", (2022).

[11] Damou, M., Chetioui, M., Boudkhil, A., and Berber, R., "Ka Bandpass Filter Based on SIW Technology for Wireless Communications". Journal of Telecommunications and Information Technology, (2021).

[12] Damou, M., Chetioui, M., Boudkhil, A., Gouni. S., Bouhmidi, R., and Bouras, B. "Optimization of Multi-Ports Combline Filter Using Admittance Extraction Technique". in 2022 International Conference of Advanced Technology in Electronic and Electrical Engineering (ICATEEE), (2022), Volume IEEE, pp. 1-5.

[13] El Mostrah. A, Potelon. B, Rius. E, Quendo. C, and Favennec. J. F, "C-band cross-coupled SIW filter using a novel topology of electric coupling," in Eur. Microw. Conf., pp. 183-191, Sep. 2010.

[14] Damou, M., Chetioui, M., Boudkhil, A., Gouni, S., Bouhmidi, R., and Bouras, B. "Coupled Rectangular Waveguide Resonator Filter Using 3D-HFSS Based Admittance Extraction", (2022).

[15] Eslava Sabaté, David, "Characterization and modeling of a coaxial cavity quadruplet based filter for mobile phone LTE-2 band", (2016).

[16] Fiedziuszko, S. J. , "Dual-mode dielectric resonator loaded cavity filters". IEEE Transactions on Microwave Theory and Techniques. (1982). Volume (30), number (9).

[17] Gouni, Slimane, Damou, Mehdi, Chetioui, Mohammed, and Boudkhil, Abdelhakim, "Design of a Bandpass Rectangular Waveguide Filter Based on Direct Coupled Technique". International Journal of Electronics and Telecommunications, (2022).

[18] Guglielmi, M. and Jarry, P., Kerherve, E., Roquebrun, O. and Schmitt, D., "A new family of all-inductive dual-mode filters". IEEE Transactions on Microwave Theory and Techniques, (2001), Volume (49).

[19] Hong, Jia-Shen. G. and Lancaster, Michael. J., "Microstrip filters for RF/microwave applications", (2004).

[20] Hong, Jia-Shen. G and Lancaster, Michael. J., "Design of highly selective microstrip bandpass filters with a single pair of attenuation poles at finite frequency". IEEE Transactions on Microwave Theory and Techniques, 2000; 48(7): 1098-107.

[21] Huang, Liwen, "Novel substrate integrated waveguide filters and circuits", (2013).

[22] Hunter, I., Billonet, L., Jarry, B., and Guillon, P., "Microwave filters-applications and technology". IEEE Transactions on Microwave Theory and Techniques, (2002). Volume (50).

[23] Imai, Kazuo and Nakakita, Hisao, "A 22-GHz-band low-noise down-converter for satellite broadcast receivers". IEEE transactions on microwave theory and techniques, (1991), Volume (39).

[24] Ismail Alyani, Razalli. M. S., Mahdi. M., Adzir. M. and Raja. A., Syamsul. R. A., Kamariah. N. and Rasid. M. F., "X-band trisection substrate-integrated waveguide quasi-elliptic filter", Progress In Electromagnetics Research, (2008). Volume (85).

[25] Jarry, P. and Baher, H., "Special issue on RF and microwave filters, modeling and design". International Journal of RF & Microwave Computer-Aided Engineering, (2007). Volume (17).

[26] Jin, Jian-Ming, "Theory and computation of electromagnetic fields", (2015).

[27] Atkinson. F.V., "Computer-aided circuit analysis Annual report", (1966).

[28] Kuo, Jen-Tsai and Chen, Sin-Ping and Jiang, Meshon, "Parallel-coupled microstrip filters with over-coupled end stages for suppression of spurious responses". IEEE Microwave and Wireless Components Letters, (2003). Volume (13).

[29] Kuo, Jen-Tsai and Jiang, Meshon and Chang, Hsien-Jen, "Design of parallel-coupled microstrip filters with suppression of spurious resonances using substrate suspension". IEEE Transactions on Microwave Theory and Techniques, (2004). Volume (52).

[30] Kurudere, Sinan, "Design of substrate integrated waveguide based bandpass filters and power dividers". Bilkent Universitesi (Turkey), (2013).

[31] Hong. J. S. G. and Lancaster. M. J., "Microstrip filters for RF/microwave applications". John Wiley & Sons,(2004).

[32] Lee, J. S. and Tsai, Chih-Ming, "New cross-coupled filter design using improved hairpin resonators". IEEE Transactions on Microwave Theory and Techniques, (2000). Volume (48).

[33] Lee, J. S., "Microwave resonator filters for advanced wireless systems". University of Michigan (2009).

[34] Liang, Ji-Fuh and Blair, D. William, "High-Q TE01 mode DR filters for PCS wireless base stations". IEEE Transactions on Microwave Theory and Techniques, (1998). Volume (46).

[35] Lopetegi, T., Laso, M., Hernandez, AG., "New microstrip-wiggly-line filters with spurious passband suppression". IEEE Transactions on Microwave Theory and Techniques, (2001). Volume (49).

[36] Makimoto, Mitsuo and Yamashita, Sadahiko, "Microwave resonators and filters for wireless communication: Theory, design and application", (2013). Volume (4).

[37] Matthaei, George. L., "Narrow-band, fixed-tuned, and tunable bandpass filters with zig-zag hairpin-comb resonators". IEEE Transactions on Microwave Theory and Techniques, (2003). Volume (51).

[38] Matthaei, G. and Young, L. and Jones, "EMT Microwave filters, impedance-matching networks, and coupling structures". Artech House Inc., Dedham, Mass. (1980).

[39] Pajonk, Joachim, "New flip chip technology utilizing non-conductive adhesive adapted for high volume chip card module production", (2004).

[40] Potelon. B, Favennec. J. F, Quendo. C, Rius. E, Person. C, and.Bohorquez. J.C, "Design of a substrate integrated waveguide (SIW) filter using a novel topology of coupling," IEEE Microw. Wireless Compon.Lett., vol. 18, no. 9, pp. 596-598, Sep. 2008.

[41] Pozar, David. M, "Microwave engineering". Fourth Editions, University of Massachusetts at Amherst, John Wiley and Sons, Inc (2012).

[42] Rezaei, Abbas and Noori, Leila and Jamaluddin, Mohd Haizal, "Novel microstrip lowpass-bandpass diplexer with low loss and compact size for wireless applications". AEU-International Journal of Electronics and Communications, (2019). Volume (101).

[43] Ruiz-Cruz, A. Jorge and Wang, Chi and Zaki, A. Kawthar, "Advances in microwave filter design techniques". Microwave Journal, (2008). Volume (5).

[43] Seyfert, Fabien and Bila, Stéphane, "General synthesis techniques for coupled resonator networks". IEEE Microwave Magazine, (2007). Volume (8).

[44] Shen. W., Wu. L.S., Sun. X.W., Yin. W.Y., and Mao. J.F. , "Novel substrate integrated waveguide filters with mixed cross coupling (MCC)". IEEE Microwave and Wireless Components Letters, (2009), Volume (19), no. 11, pp. 701-703.

[45] Shirkhar, Mohammad Moein and Roshani, Sobhan, "Design and Implementation of a Bandpass-Bandpass Diplexer Using Coupled Structures". Wireless Personal Communications, (2022). Volume (122).

[46] Gouni. S., Damou. M., Chetioui. M. and Boudkhil. A. "Design of a Bandpass Rectangular Wave guide Filter Based on Direct Coupled Technique". International Journal of Electronics and Telecommunications, (2022).

[47] Gouni. S., Damou. M., Chetioui. M. and Boudkhil. A. "Design of a Cross-Coupled Third Order Bandpass Filter on Substrate Integrated Waveguide Resonator (SIW-R)". International Journal of Microwave and Optical Technology, (2023). Volume 19(11), 8701-703.

[48] Thomas, J. Brian, "Cross-coupling in coaxial cavity filters-a tutorial overview". IEEE Transactions on Microwave Theory and Techniques, (2003). Volume (51).

[49] Uhm, Manseok and Lee, Juseop and Yom, Inbok and Kim, Jeongphill, "General coupling matrix synthesis method for microwave resonator filters of arbitrary topology". ETRI Journal, (2006).

[50] Velazquez. A. , Martel. J . and Medina. F., "Parallel coupled microstrip filters with ground-plane aperture for spurious band suppression and enhanced coupling". IEEE transactions on microwave theory and techniques, (2004). Volume (52).

[51] Wang, Chi and Ruiz-Cruz, Jorge and Zaki, A. Kawthar, "Generalized Chebyshev filter design based on source-load coupling". IEEE Transactions on Microwave Theory and Techniques, (2007). Volume (8).

[52] Wei, Feng and Wu, Kai and Cheng, Jin, "Substrate integrated waveguide filters: Basic design rules and fundamental structures". IEEE Microwave Magazine, (2014).

[53] Wolf, Ian and Irci, Evren, "Cross-coupling and phase cancellation in microwave cavity filters: Theory and experiment". IEEE Transactions on Microwave Theory and Techniques, (2015).

[54] Woode. A. and Petit. J., "Design data for the control of multipactor discharge in spacecraft microwave and RF systems". Microwave Journal, (1992). Volume (35).

[55] Woode. A. and Petit. J., "Investigations into multipactor breakdown in satellite microwave payloads". ESA Journal, (1990). Volume (14).

Publications and seminar participation

Publication

1. **SLIMANE Gouni**, **MEHDI Damou**, **MOHAMMED Chetioui**, and al. Design of a Bandpass Rectangular Waveguide Filter Based on Direct Coupled Technique. International Journal of Electronics and Telecommunications, 2022, p. 483-488-483-488.
2. **SLIMANE Gouni**, **MEHDI Damou**, **MOHAMMED Chetioui**, and al. Design of a Cross-Coupled Third Order Bandpass Filter on Substrate Integrated Waveguide Resonator (SIW-R). International Journal of Microwave Optical Technology, 2023, vol. 18, no 1.

International communications:

1. Damou Mehdi, Chetioui Mohammed, Boudkhil Abdelhakim, and **Gouni Slimane**. Coupled Rectangular Waveguide Resonator Filter Using 3D-HFSS Based Admittance Extraction. In : 2022 7th International Conference on Image and Signal Processing and their Applications (ISPA). IEEE, 2022. p. 1-5.
2. Damou Mehdi, Chetioui Mohammed, **Gouni Slimane**, and al. Optimization of Multi-Ports Compline Filter Using Admittance Extraction Technique. In : 2022 International Conference of Advanced Technology in Electronic and Electrical Engineering (ICATEEE). IEEE, 2022. p. 1-5.
3. **Gouni Slimane**, Damou Mehdi, Chetioui Mohammed, Boudkhil Abdelhakim and Berber Redouane ‘’ Optimization of Analytical Design and

Cascaded Trisection of Substrate-Integrated Waveguide Cross-Coupled Filters", 3rd International Conference on Electronics and Electrical Engineering.

4. Damou Mehdi, **Gouni Slimane**, Chetioui Mohammed, Boudkhil Abdelhakim and Berber Redouane," Design and Simulation of Microscopic patch Antenna Arrays for Wireless Communication Application", 5th International Conference on Embedded Systems in Telecommunications and Instrumentation.

5. Mehdi Damou, **Gouni Slimane**, Bouras Maroua, Chetioui Mohammed, Boudkhail Abdelhakim and Nouri Keltouma. "Design of a Filter Based on Direct Coupled Resonators Using The Coupling Matrix Technique". ICAECCT'23: The 1st International Conference on Advances in Electronics, Control and Computer Technologies

6. Senasli Lamia, Mehdi Damou, Senasli Houda, Chetioui Mohammed, **Gouni Slimane** and Boudkhil Abdelhakim."Electromagnetic Optimization of Bandpass Cross-Coupled Filter for mobile Communication". ICAECCT'23: The 1st International Conference on Advances in Electronics, Control and Computer Technologies.

National Conference:

1. **Gouni Slimane**, Damou Mehdi, Chetioui Mohammed, Boudkhil Abdelhakim and Berber Redouane. 'Analysis of Substrate Integrated Waveguide Hexagonal Resonator of Cross-Coupled Filters'.CNTA'22: National Conference on Telecommunications and its Applications.

2. **Gouni Slimane** 'Microwave Cavity Filters Using Local Linear Embedding Technique for Double Deep Q-Learning Approach'.SAIDA ARTIFICIAL INTELLIGENCE DAY.

3. **Gouni Slimane**, Damou Mehdi, Chetioui Mohammed, Boudkhil Abdelhakim 'Analytical Design of Cascaded Trisection Substrate Integrated Waveguide (SIW) filter with hexagonal Resonator of Cross-Coupled Filters'. https://sites.google.com / view/national-conference-ncetee23/home